Cortical circuits for cross-modal generalization

Maëlle Guyoton[1]*, Giulio Matteucci[1]*, Charlie G. Foucher[1], Matthew P. Getz[2], Julijana Gjorgjieva[2] & Sami El-Boustani[1]

[1] Department of Basic Neurosciences, Faculty of Medicine, University of Geneva, 1 Rue Michel-Servet, 1206 Geneva, Switzerland.

[2] School of Life Sciences, Technical University of Munich, Maximus-von-Imhof-Forum 3, 85354 Freising, Germany.

* These authors contributed equally to this work.

Summary

Adapting goal-directed behaviors to changing sensory conditions is a fundamental aspect of intelligence. The brain uses abstract representations of the environment to generalize learned associations across sensory modalities. The circuit organization that mediates such cross-modal generalizations remains, however, unknown. Here, we demonstrate that mice can bidirectionally generalize sensorimotor task rules between touch and vision by using abstract representations of peri-personal space within the cortex. Using large-scale mapping in the dorsal cortex at single-cell resolution, we discovered multimodal neurons with congruent spatial representations within multiple associative areas of the dorsal and ventral streams. Optogenetic sensory substitution and systematic silencing of these associative areas revealed that a single area in the dorsal stream is necessary and sufficient for cross-modal generalization. Our results identify and comprehensively describe a cortical circuit organization that underlies an essential cognitive function, providing a structural and functional basis for abstract reasoning in the mammalian brain.

Introduction

Objects possess unique physical properties that are detected by different sensory organs. The brain seamlessly integrates these sensory inputs to create unified percepts and abstract representations of the environment, which are essential for generalizing behaviors to unfamiliar situations[1]. This phenomenon is especially pronounced in the peri-personal space, where visual and tactile inputs converge[2]. Indeed, an object's position and identity, initially discerned through touch in darkness, can immediately be recognized by sight in light. Cross-modal generalization —also called cross-modal transfer learning— describes the process by which recognition in one sensory modality enables the generalization of learned associations to others, a capability observed across diverse species[2–5], suggesting a common foundational circuit organization. Across the hierarchy of sensory systems, neural representations become increasingly invariant to low-level features, including the specific sensory modality of a stimulus, ultimately abstracted to form representations that encode perception in a modality-independent manner. While neuronal correlates of such abstract representations have been identified — from supramodal stimulus feature encoding in the rat posterior parietal cortex to “concept cells” in the human temporal lobe[6–9] — the cortical architecture enabling their use for generalized learning across sensory modalities remains to be elucidated . Mice have proven to be a valuable model for dissecting circuits responsible for multisensory integration and their role in goal-directed behavior[10–13]. Mice rely on visuo-tactile inputs for behaviors such as gap crossing[14], navigation[15], and object recognition[6]. Because whiskers occupy a substantial portion of the visual field, both somatosensory and visual systems frequently receive correlated inputs (Fig. 1a). In the superior colliculus, multimodal representations of whisker and visual information possess topographically co-aligned

functional maps[16,17], potentially enhancing reflexive behaviors like gaze and head orientation by increasing the salience of spatially congruent multisensory events[18]. Cortical circuits, critical for perception and goal-directed behaviors, also display multimodal visuo-tactile responses. In particular, associative areas within the posterior parietal cortex receive inputs from both the primary visual cortex (V1) and the primary somatosensory cortex (S1)[19]. However, the precise nature of the functional and anatomical organization of cortical areas dedicated to visuo-tactile processing, as well as their potential role in cross-modal generalization of learned sensorimotor associations, remains unknown. Here we investigate these circuits in mice performing goal-directed behaviors.

Results

Cross-modal generalization in mice

We designed a behavioral paradigm to test the ability of mice to generalize sensorimotor associations learned through whisker sensations to the visual modality. Given that both sensory modalities share a common spatial organization within the peri-personal space (Fig. 1a), the task includes visual and tactile stimuli that originate from locations that are spatially congruent (Fig. 1b). In the dark, head-fixed and water-restricted mice were first trained on a Go/No go tactile discrimination task, where they had to discriminate between stimulations of two whiskers vertically arranged in the same column of the whisker pad. Mice were rewarded with a drop of water if they licked a spout upon stimulation of the top whisker (B2) whereas they were punished with a 10-second-long timeout if they licked for the bottom whisker (C2). Once mice became expert at the task and performed stably with a high percentage of correct trials

over at least 3 consecutive sessions, we switched the task to a Go/No go visual task. In this condition, we replaced the top and bottom whisker stimulations with top and bottom visual stimuli. These stimuli consisted of black squares on a gray background drifting along the same rostro-caudal direction than the whisker deflections. The screen was oriented to be centered and parallel to the right retina on the same side as the previously stimulated whiskers. The location of the moving squares along the vertical axis was chosen to roughly match the location of the whiskers within the visual field of the animals (see Methods).

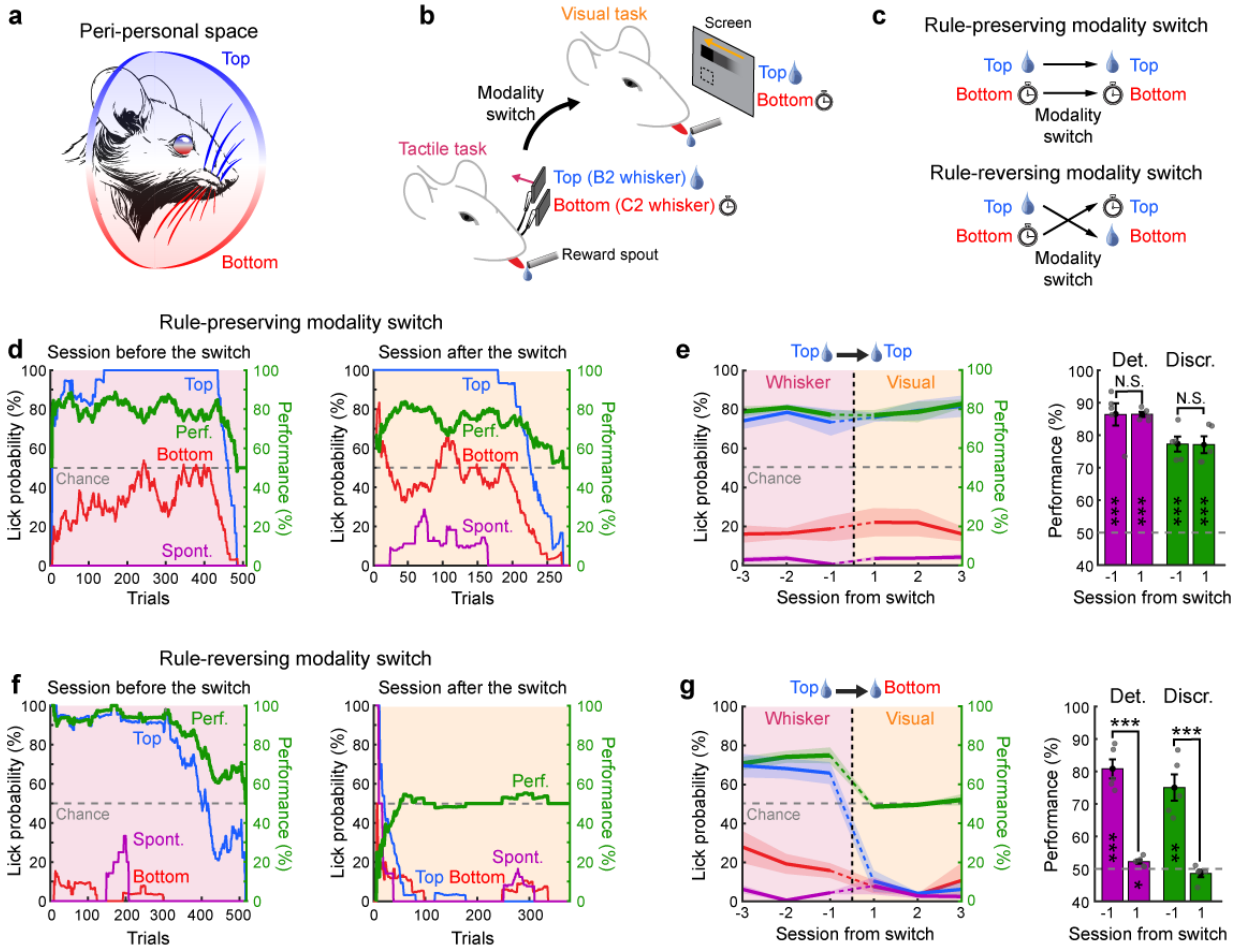

Fig. 1. Cross-modal generalization in mice.

a, Illustration of the common organization of the peri-personal space for visual and whisker tactile inputs in mice. **b,** Schematic of the behavioral Go/No go paradigm for studying cross-modal generalization of spatial information in mice. **c,** Two types of tactile-to-visual modality switches: "rule-preserving", wherein the spatial location of rewarded stimuli is preserved, and "rule-reversing", wherein the location of rewarded stimuli is reversed. **d,** Left: example of a session with the tactile task the day before modality switch. Conditional lick probabilities over trials are shown for the top whisker (blue), the bottom whisker (red) and in absence of stimuli (purple). Task performance (green) is computed as the percentage of correct discrimination

trials (see Methods). Chance level is shown as a gray dashed line. Traces were computed on a sliding window of 60 trials. Right: same as left for the first visual session following a rule-preserving modality switch. **e,** Left: task performance and conditional lick probabilities averaged across mice (N=5 mice) over three consecutive sessions before and after a rule-preserving switch (vertical dashed line). Shaded area: S.E.M. Color code as in panel d. Right: detection (purple) and discrimination (green) performance distribution for the session before and after the switch (two-sided paired t-test comparing days, *p<0.05, **p<0.01, ***p<0.001, N.S. Not significant). Performances are also tested against chance level (two-sided t-test, *p<0.05, **p<0.01, ***p<0.001, Blank: Not significant). **f-g,** Same as in panels d-e but for a rule-reversing modality switch.

To test whether mice can use previous associations learned during the tactile task to infer the reward contingency (i.e. the rule that determines when a reward will be delivered following a sensorimotor response) in a new visual task, we considered two scenarios: a “rule-preserving” and a “rule-reversing” modality switch. The cohort of mice undergoing the rule-preserving modality switch could obtain a reward by licking for stimuli presented at the same spatial location after the switch. For mice undergoing the rule-reversing switch, the reward contingency was spatially reversed following the switch to the new modality (Fig. 1c). Following rule-preserving modality switches, we observed rapid generalization of the learned association to the new modality. Mice seamlessly performed the task with a comparable level of high performance as observed in the session preceding the switch (Fig. 1d,e), already within the first few tens of trials. In contrast, task performance was strongly affected following a rule-reversing modality switch, consistently falling at chance level or below. Mice typically attempted to lick in response to both stimuli during the early part of the session before rapidly disengaging and ceasing any licking behavior (Fig. 1f). In many cases, mice attempted to lick first for visual stimuli spatially congruent with the previously rewarded whisker, causing performance to briefly drop below chance level during the early phase of the session. Following rule-reversing switches, mice displayed a strong resistance to engaging with the task for several consecutive sessions (Fig. 1g). We

verified that this result was not caused by a preference for the top whisker or for the top visual stimulus by repeating the same experiments with cohorts of mice trained to lick for bottom whisker stimulations. Mice maintained high task performance after switches that preserved the spatial rule, regardless of whether they were initially trained on one whisker or another, but performance briefly dropped below chance when the rule was reversed (N=10 mice, two-sided t-test with respect to chance level in the first 100 trials, p=0.02), before eventually disengaging (Extended Data Fig. 1a-c). Such disengagement after a rule-reversing modality switch persisted despite strong thirst-driven motivation, as indicated by prolonged licking bouts observed when water drops were manually delivered to maintain task engagement[20]. To ensure comparable thirst levels across sessions, we carefully regulated water intake and monitored weight loss for each mouse. Furthermore, all cohorts were equally trained and exhibited comparable performance and engagement before the modality switch (Extended Data Fig. 2a-d). This implies that the mouse's failure to perform after a rule-reversing modality switch stems from conflicting prior knowledge of the task rule, rather than from a lack of experience or motivational drive.

Despite the limited visibility of the capillary glass tubes used for whisker stimulations in the dark, we tested whether mice could rely on the movement of tubes as visual cues to perform the tactile task, thereby generalizing within the visual domain instead of across sensory modalities. We carried out control experiments where mice proficient in the tactile task underwent sessions with whiskers temporarily removed from the tubes, and subsequently reintroduced. We observed that both detection and discrimination performance dropped to chance level immediately after the whiskers were removed from the capillary tubes, but recovered to expert levels once the whiskers were reinserted into the piezo stimulators (Extended Data Fig. 3). This

demonstrates that mice were not using visual cues to perform the whisker discrimination task in the dark.

Besides generalizing task rule through common spatial organization, mice could also potentially generalize the abstract Go/No go structure common to the two tasks (i.e. “acting upon one stimulation, the Go stimulus, leads to reward while acting upon the other, the No go stimulus, leads to a timeout”) to rapidly increase performance after the switch. To investigate this possibility, we trained mice on an auditory Go/No go discrimination task, which produced similar levels of motivation and performance without prior knowledge of spatial rules related to reward contingency. Mice were then switched to the spatial visual task (Fig. 2a). The stimuli used for the auditory task were two pure tones played from the same speaker, bearing no clear spatial relationship to the visual stimuli introduced after the modality switch. In absence of spatial prior, performance dropped to chance level after the switch but steadily recovered to expert level over the next few sessions (Fig. 2b and Extended Data Fig. 1d-e). We concluded that mice could learn the task after modality switch significantly faster in absence of the conflicting spatial prior observed for mice experiencing rule-reversing modality switches (Fig. 2c).

We further confirmed that mice could also generalize the task rule from the visual to the tactile modality, demonstrating bidirectional cross-modal generalization of learned associations (Fig. 2d-f and Extended Data Fig. 1f-h). Notably we observed a consistent drop in performance during switches from visual to tactile modalities under rule-preserving conditions, an effect that was absent during tactile-to-visual switches. This asymmetry likely reflects differences in task difficulty specific to each modality, leading to distinct performance ceilings for the visual and tactile tasks, regardless of whether they were performed before or after the modality switch (Fig. 2g). The difference in

task difficulty may stem from lower discriminability capabilities between nearby whiskers compared to small visual stimuli, despite their matching spatial locations. Consequently, task performance is expected to remain stable or improve slightly when switching from a tactile to a visual task. In contrast, a performance decline is anticipated when switching from a visual to a tactile task, consistent with our observations. None of the observed behavioral effects could be attributed to differences in learning trajectory, expertise level, or motivational state, as the different cohorts of mice were exposed to a comparable number of trials, performed similarly, and exhibited the same weight loss (Extended Data Fig. 2).

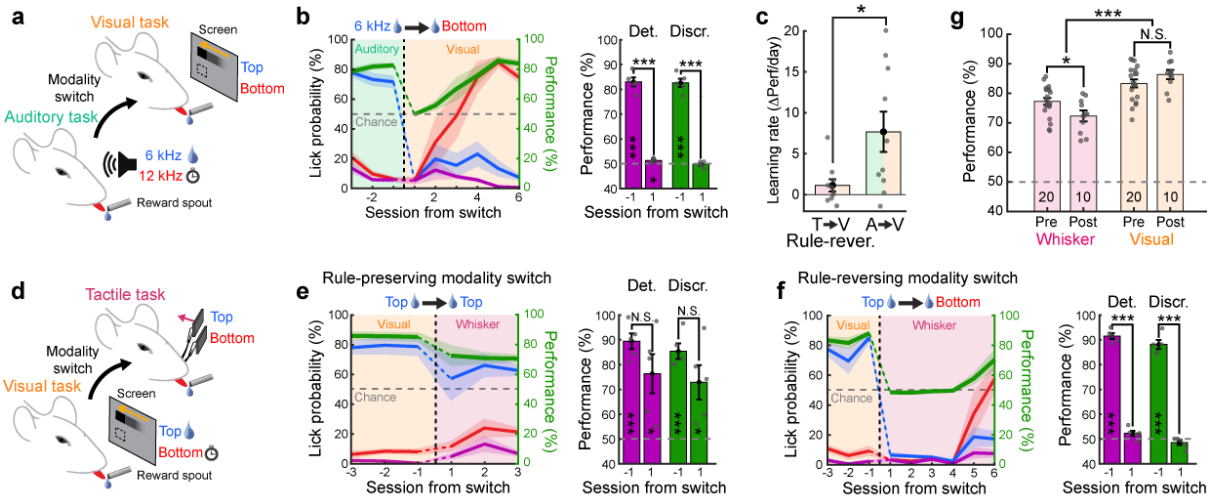

Fig. 2. Bidirectional cross-modal generalization of spatial information.

a, Schematic of the behavioral paradigm where switches occur between an auditory discrimination task with two pure tones (6 kHz and 12 kHz) and a visual task. The 6 kHz tone only is associated with a water reward. **b,** Left: Average task performance and conditional lick probabilities across sessions for mice (N=5 mice) undergoing a modality switch (dashed vertical line). Shaded areas and color code as in Fig. 1e. Right: detection (purple) and discrimination (green) performance distribution for the session before and after the switch (two-sided paired t-test comparing days, *p<0.05, **p<0.01, ***p<0.001, N.S. Not significant). Performances are also tested against chance level (two-sided t-test, *p<0.05, **p<0.01, ***p<0.001, Blank: Not significant). **c,** Comparison of relearning rates between mice that underwent a rule-reversing tacto-visual modality switch and mice that underwent switch from a non-spatial auditory task to the same visual task (N=10 mice for tactile group and N=10 mice for auditory group, unpaired two-sided t-test, *p=0.02). **d,** Schematic of the behavioral paradigm, where switches occur between a visual task and a tactile task with the top visual stimulus being the rewarded one. **e,** Same as panel b for mice undergoing a rule-preserving switch (N=5 mice). **f,** Same as panel b but for a rule-reversing modality switch. **g,** Comparison of average task performance in the tactile and visual tasks before (pre) or after (post) modality

switches across mice (sample size indicated in the bar plot). Only mice that underwent rule-preserving switches were included after the switch (two-sided unpaired Wilcoxon test, *p<0.05, ***p<0.001, N.S. Not significant).

Finally, we compared our results for rule-reversing modality switches with conditions in which reward contingencies were switched within the tactile modality, as previously studied[21,22]. After mice reached expert level in the tactile task, we reversed the reward contingencies between the two whiskers. This led to a stark drop in discrimination performance below chance level, indicating that mice rigidly persisted in performing the task following the original rule (Extended Data Fig. 4). Following the switch, performance increased but remained below or at chance level for at least three consecutive sessions. Thus, mice behave differently when reward contingencies are switched within the same sensory modality as they continue to inflexibly produce the same sensorimotor transformation, likely reflecting ingrained habitual behaviors.

Co-aligned visuo-tactile spatial maps in the dorsal cortex

Our behavioral results suggest that mice can generalize previously learned sensorimotor associations across sensory modalities (Extended Data Fig. 5), based on a common representation of the peri-personal space. Cortical circuits are necessary for perception and are believed to mediate flexible goal-directed behaviors such as cross-modal generalization[2,23]. To pinpoint the cortical regions responsible for visuo-tactile generalization, we mapped the topographic representation of vertical space for both modalities in the dorsal cortex of transgenic mice expressing the calcium indicator GCaMP6f in cortical layers 2/3 (Fig. 3a, see Methods). We first used established retinotopic and somatotopic mapping protocols[20,24] to identify whisker-responding and retinotopically organized cortical areas through a 5 mm diameter cranial window over the posterior part of the left dorsal cortex (Extended Data Fig. 6a).

Whisker response patterns and retinotopic sign maps enabled us to precisely fit a projection of the Allen Mouse Brain Atlas to the cranial window of each mouse (see Methods). We used this atlas to register all functional maps into a common reference frame (Extended Data Fig. 6b-f).

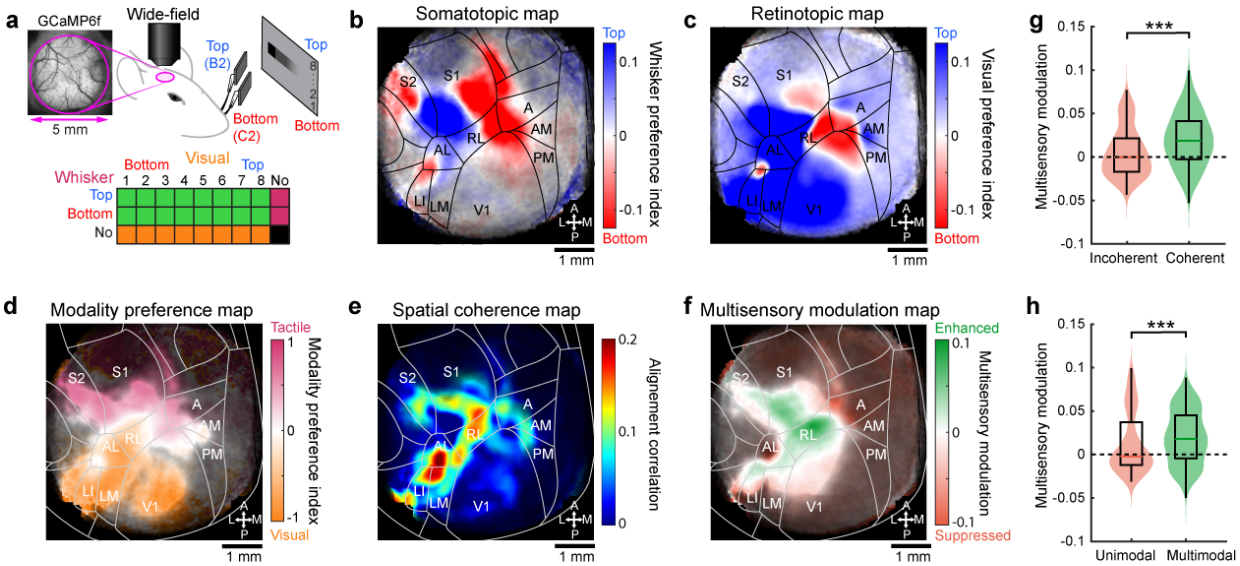

Fig. 3. Co-aligned visual and tactile functional maps in the dorsal cortex.

a, Top: schematic of the visuo-tactile sparse noise protocol used during wide-field imaging of GCaMP6f-expressing mice through a cranial window. Bottom: matrix of all combinations of visual and whisker stimuli (green: multisensory, orange: visual, magenta: tactile). **b,** Somatotopic map of vertical space computed from whisker stimuli averaged across mice (N=29 mice for all panels of the figure), with transparency defined by response significance in each pixel (see Methods). A projection of the Allen Mouse Brain Atlas is overlaid on top with areas names and orientation. **c,** Average retinotopic map of vertical space. **d,** Average modality preference map between visual and tactile responses. **e,** Average spatial coherence map between visual and tactile representations (see Methods). **f,** Average multisensory modulation map comparing visuo-tactile responses and combination of unisensory responses (see Methods). **g,** Multisensory modulation index for pixels belonging in regions of high spatial coherence compared to regions without spatial coherence (n=26,286 pixels versus n=28,394 pixels, unpaired two-sided Wilcoxon test, ***$p<10^{-300}$). **h,** Multisensory modulation index for pixels belonging to unimodal or multimodal regions (n=10,264 pixels versus n=15,921 pixels, unpaired two-sided t-test, ***$p<10^{-116}$).

To characterize the cortical representation of the vertical space for both unisensory and multisensory stimulations, we designed a visuo-tactile sparse noise protocol (Fig. 3a). Tactile stimuli consisted of single whisker deflections applied to either the top or bottom whisker, while visual stimuli were black squares drifting in the

rostro-caudal direction, displayed at eight different vertical locations. Visual and tactile stimuli were presented either individually or simultaneously in all possible combinations (see Methods). This protocol was used in task-naïve mice to obtain retinotopic and somatotopic maps for vertical space by computing the preferred spatial position for each pixel. In response to whisker stimuli, we identified the well-established somatotopic arrangement of the primary and secondary whisker somatosensory cortices, S1 and S2, which exhibited a topographic inversion at their boundary (Fig. 3b). Importantly, we observed that whisker stimulations also evoked organized somatotopic maps in several visually responsive areas including the anterior (A), rostro-lateral (RL), antero-lateral (AL) and latero-intermediate (LI) areas. This suggested that whisker representations might be present in a more extended cortical network than previously reported[25]. Strikingly, the maps we obtained with visual stimuli displayed a very similar organization to the tactile ones in these associative areas as well as in S1 and S2 (Fig. 3c). The extended spatial representations evoked by visual or tactile stimuli were found consistently across mice (Extended Data Fig. 6g). This suggests that spatially localized stimuli, regardless of their visual or tactile nature, might share a common topographic representation that facilitates mapping between sensory modalities, as previously observed in the superior colliculus[16,17]. Spatial representations evoked by these two modalities displayed an angular offset that we estimated around 30 degrees by comparing the angle difference between gradient vectors obtained from these maps (see Methods). This might reflect the mouse's internal model of how whisker sensations align with their corresponding locations in the visual field[13].

We further investigated the functional properties of these representations by first computing a modality preference index to assess what sensory modality

285 dominates each area (Fig. 3d). As expected, S1 and S2 were dominated by tactile
286 inputs whereas V1 was dominated by visual inputs. RL and the region at the border
287 between AL and LI displayed a more balanced preference for both modalities. In
288 addition, we measured the spatial coherence between maps of vertical retinotopy and
289 somatotopy indicating local co-alignment (Fig. 3e, see Methods). This confirmed a
290 widespread spatial co-alignment across most associative areas in the belt between
291 V1 and S1. We further computed a multisensory modulation index, comparing
292 multisensory responses triggered by visuo-tactile stimuli to the maximal unisensory
293 response on a pixel-by-pixel basis (see Methods). The resulting map revealed a strong
294 multisensory enhancement in visuo-tactile associative areas and in S1 (Fig. 3f).
295 Multisensory responses were comparable under visuo-tactile conditions where
296 whisker stimuli were synchronous or delayed by 0.15 seconds to ensure simultaneity
297 of evoked responses in the cortex (Extended Data Fig. 7), with a tendency to show
298 stronger enhancement in the latter case, as previously documented[19]. Moreover, we
299 found that multisensory enhancement was more pronounced in regions with higher
300 coherence between spatial maps and with strong bimodal representations (Fig. 3g,h).

301

302 **Anatomical origin of spatial maps in the dorsal cortex**

303 Functional maps measured with wide-field calcium imaging could result from
304 direct inputs from visual and tactile primary cortical areas, from evoked top-down
305 inputs[26], or even be the result of highly stereotypical uninstructed movements evoked
306 by sensory stimuli[27]. To investigate the synaptic origin of these maps, we performed
307 anatomical experiments to map both feedforward and feedback projections between
308 primary sensory areas and associative areas displaying visuo-tactile representations
309 (Fig. 4a). We obtained visual and tactile functional maps for representation of vertical

space in wild-type mice using intrinsic optical signal imaging under low isoflurane anesthesia (Extended Data Fig. 8a,b,d,e, see Methods). These maps were then used to identify two cortical locations representing distinct iso-horizontal vertical positions in V1 or to target B2 and C2 barrels in whisker S1. We then opened the cranial window and injected two adeno-associated viral vectors to induce expression of tracer proteins GFP and tdTomato in the respective locations (Extended Data Fig. 8c,f). After 10-15 days, transcardial perfusions were performed and brains were extracted, flattened, and sliced (see Methods). Enriched M2 subtype muscarinic acetylcholine receptors (M2 AChR) in V1 and S1 barrel field were used as landmarks to fit the Allen Mouse Brain Atlas on the reconstructed stack, confirming the location of injection sites along the vertical representation of V1 and S1 (Fig. 4b,c). Axonal projections from primary sensory areas were found in associative cortical regions where visuo-tactile responses were measured with the same spatial organization. Variability in injection sites allowed us to create an anatomical map that described axonal preferences for top and bottom location (Fig. 4b,c), aligning closely with wide-field imaging results (Fig. 3b,c). This confirmed that the functional maps are inherited, at least in part, from direct feedforward projections from primary cortical areas.

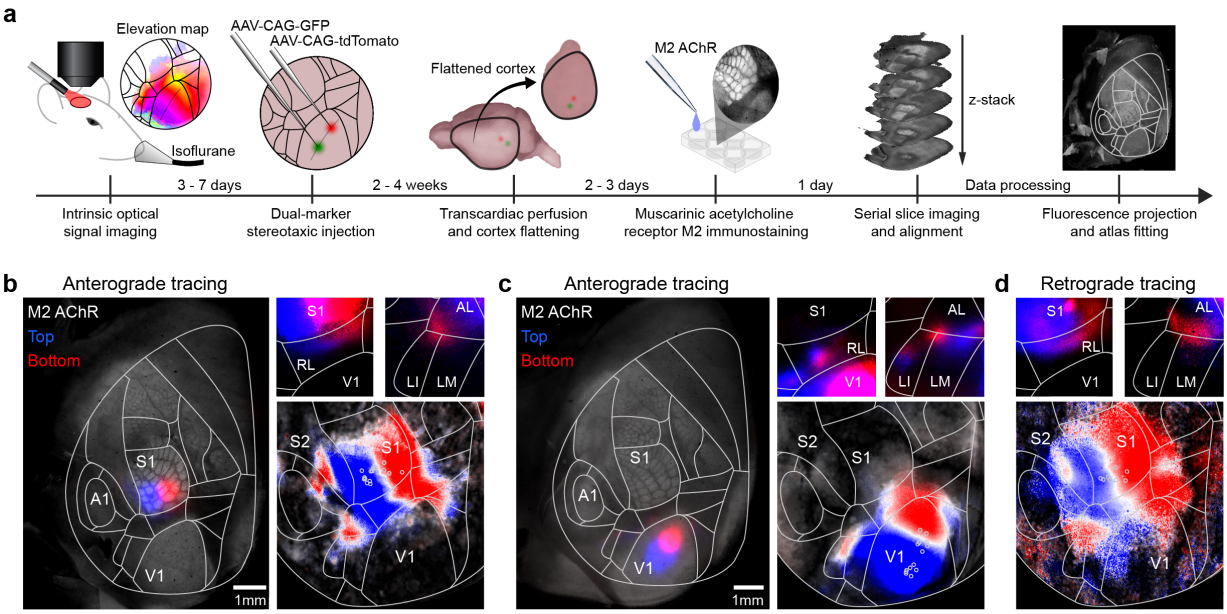

Fig. 4. Co-aligned visual and tactile anatomical projection maps in the dorsal cortex.

a, Schematic of the data collection and analysis pipeline for topographic anatomical tracing. **b,** Anterograde labeling of S1 projections using injections of viral vectors AAV-CAG-GFP and AAV-CAG-tdTomato. Left: injection sites in B2 and C2 barrels in whisker S1. Right: conserved somatotopic organization of projections in associative areas for the cortex shown on the left (top). Bottom: Reconstructed whisker preference averaged across mice using all injection sites depicted by circles (see Methods, N=9 mice and n=18 injections, Pearson coefficient of correlation between anatomical and wide-field map: 0.8311, $p<10^{-300}$). **c,** Same as panel b but for anterograde labeling of V1 projections with two injection sites along the iso-horizontal axis (N=7 mice and n=14 injections, Pearson coefficient of correlation: 0.5121, $p<10^{-300}$). **d**, Retrograde labeling of S1-projecting neurons using CTB-Alexa 555 and CTB-Alexa 647 injections. Top: Examples of CTB-labeled neurons spatially organized in associative areas. Bottom: Reconstructed map of preferred whisker in projecting neurons over the dorsal cortex combining all injection sites (N=5 mice and n=8 injections, Pearson coefficient of correlation: 0.663, $p<10^{-300}$).

While visual stimuli could evoke organized responses in S1 (Fig. 3c), no direct projections were found between V1 and S1[28] suggesting the existence of spatially organized feedback projections from associative areas to S1. Previous work has shown that feedback projections from higher visual areas (including A, RL, AL and LI) to V1 are spatially organized along the vertical dimension[29] but it is not clear if this holds true for feedback projections to S1. Feedback projections from associative areas to S1 were characterized using the same strategy, but with injections of Cholera Toxin Subunit B (CTB) conjugated either with Alexa 555 or Alexa 647 (Fig. 4d). S1-projecting neurons for top and bottom locations aligned with wide-field imaging (Fig. 3b) and anterograde tracing (Fig. 4b). We additionally confirmed that the same was true for V1 (Extended Data Fig. 8g) as previously reported[29]. Thus, we observed a shared spatial organization of feedforward and feedback projections between primary and associative areas. Using retrograde labeling with CTB injections in RL, we also compared the cell density of RL-projecting neurons in V1 and S1, revealing that V1 contains a denser population of neurons projecting to RL (Extended Data Fig. 8h-k). This asymmetry, together with feedback connections from associative areas to

primary cortices, could explain why visual stimuli evoked stronger responses in S1 than the other way around (Fig. 3b-c).

Single-neuron visuo-tactile functional properties

Spatially organized feedforward and feedback projections could facilitate generalized sensorimotor learning through transfer of spatial information across sensory modalities. However, functional maps obtained with wide-field imaging do not reveal precise computations performed at single-cell level and could still be prone to artifacts produced by neuronal processes originating from other brain structures. To overcome this limitation and assess if neurons in associative areas can mediate cross-modal generalization, we performed two-photon calcium imaging in a subset of mice (Fig. 5a). Single neuron somatic GCaMP6f signal was extracted during the visuo-tactile sparse noise protocol in fields-of-view covering different cortical areas identified with the atlas (Extended Data Fig. 9a-f). Given the observed fluorescence response patterns to various unimodal and multimodal stimuli (Fig. 5b), we could map specific functional properties of single neurons onto the reference atlas, pooling data across mice, for comparison with corresponding wide-field regions. Many recordings were performed across a large portion of the dorsal cortex to extensively cover responsive visuo-tactile areas (Extended Data Fig. 9g-h). We reconstructed the somatotopic map of vertical space across the cranial window (Fig. 5c), which closely aligned with the wide-field map (Fig. 3b). Neurons with whisker tactile responses were found across the belt of associative areas following the somatotopic organization. This further confirmed the existence of an extended network of whisker responsive and visuo-tactile cortical regions[25]. The same was true for neurons responding to visual stimuli, which were found across most visual and tactile areas, including S1 (Fig. 5d),

consistent with the responses observed using wide-field imaging (Fig. 3c). Reconstructed population maps based on single-neuron properties consistently matched with functional maps measured with wide-field calcium imaging (Extended Data Fig. 10).

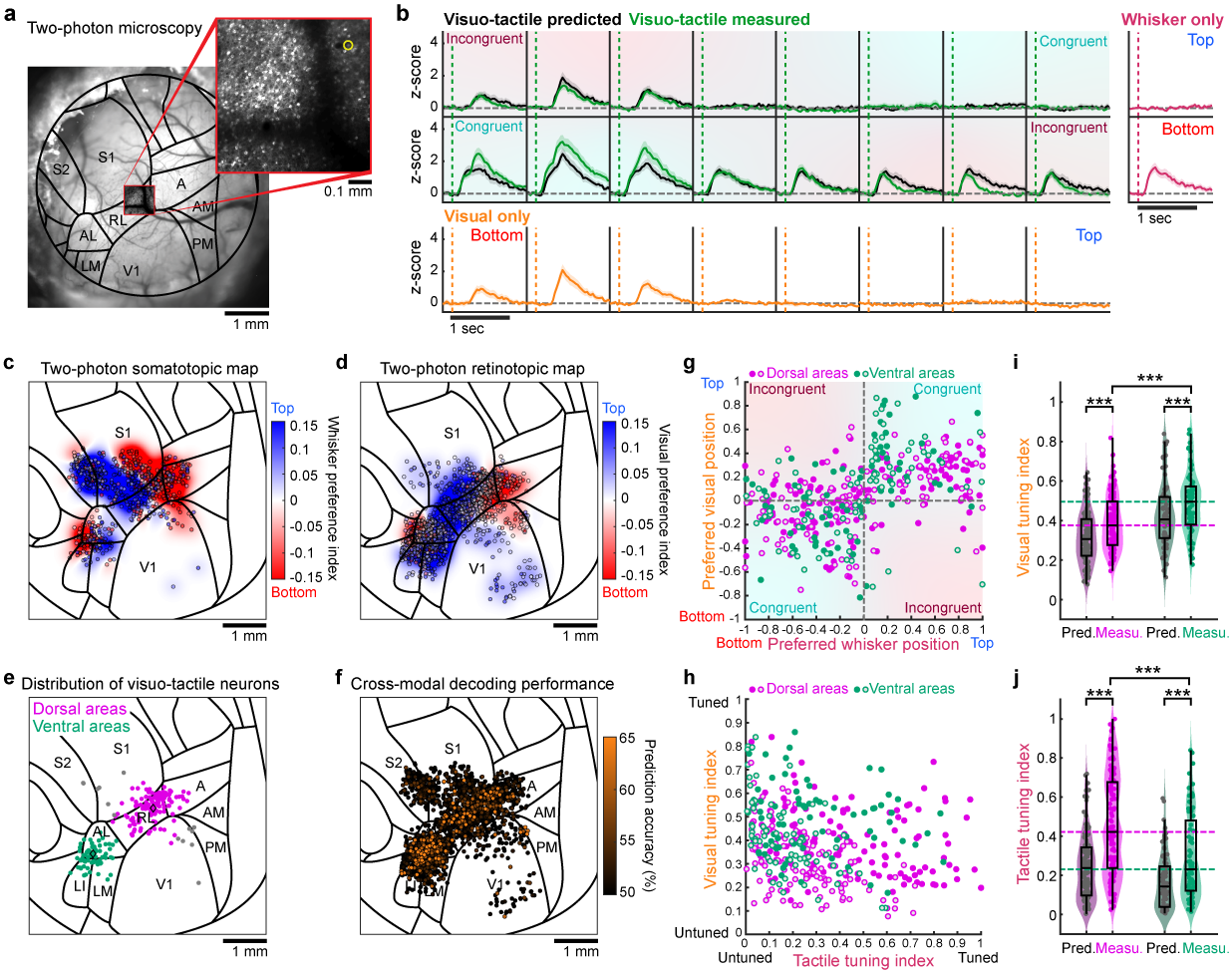

Fig. 5. Visuo-tactile representation of peri-personal space in single neurons.

a, Example cranial window and two-photon field-of-view overlapping with the medial part of area RL. **b,** Response pattern of GCaMP6f fluorescence for the example neuron highlighted with yellow circle in panel a. Unisensory responses (z-scored) are shown on the side for visual (orange) or whisker (magenta) stimuli. Predicted multisensory responses are shown for visuo-tactile stimuli (black) together with measured responses (green). Error bars: S.E.M. **c,** Population of single neurons imaged with two-photon microscopy to measure significant responses to whisker stimuli (n=567 neurons, N=25 mice). Each spot represents a single neuron, and the color code indicates preference for top (blue) or bottom (red) stimuli. The reconstructed wide-field map is displayed in the background (see Methods, Pearson coefficient of correlation: 0.8472, $p<10^{-300}$). **d,** Same as panel c for neurons significantly responding to visual stimuli (n=1,593 neurons, Pearson coefficient of correlation: 0.6505 $p<10^{-300}$). **e,** Distribution of all visuo-tactile bimodal neurons identified. Neurons are classified as being part of the ventral (green) or dorsal (pink) pathway depending on their location (see Methods). Neurons that are not part of these pathways are shown in gray. **f,** Distribution of

responsive neurons color-coded by their visual decoding accuracy, following training with whisker-stimulation responses (see Methods, N=2,563 neurons, N=25 mice). **g,** Comparison of preferred visual position and preferred whisker along the vertical axis in visuo-tactile stimulations condition for predicted (open circles) and measured (full circles) responses of ventral neurons (n=75 significantly responsive multimodal neurons, Pearson coefficient of correlation: 0.36 for predicted with $p=1.6x10^{-3}$ and 0.48 for measured with $p=1.5x10^{-5}$; 77% of neurons in congruent quadrants) and dorsal neurons (n=124 significantly responsive multimodal neurons, Pearson coefficient of correlation: 0.55 for predicted with $p=3.7x10^{-11}$ and 0.47 for measured with $p=4.3x10^{-8}$; 71% of neurons in congruent quadrants). **h,** Comparison between tactile and visual tuning indices computed from the predicted (open circles) or measured (full circles) visuo-tactile responses of neurons in panel e. **i,** Comparison of the visual tuning indices from panel h between predicted and measured responses for ventral and dorsal stream neurons (two-sided paired Wilcoxon test between measured and predicted for ventral: n=75 neurons, ***$p=1.7x10^{-5}$; for dorsal: n=124 neurons, ***$p=3.1x10^{-11}$; two-sided unpaired t-test comparing dorsal and ventral measured responses: ***$p=3.2x10^{-5}$). **j,** Same as panel i for the tactile tuning indices (two-sided paired Wilcoxon test between measured and predicted for ventral: n=75 neurons, ***$p=7.7x10^{-10}$; for dorsal: n=124 neurons, ***$p=1.6x10^{-19}$; two-sided unpaired t-test comparing dorsal and ventral measured responses: ***$p=1.1x10^{-5}$).

Among all neurons imaged, we identified four functional cell-types. Unisensory visual or tactile neurons only responded to their respective modality, gated neurons responded only when both visual and tactile stimuli were presented together, and bimodal visuo-tactile neurons responded to both unisensory visual and whisker stimuli (Extended Data Fig. 11a-b). Importantly, bimodal visuo-tactile neurons localized into two distinct clusters (Fig. 5e), corresponding to the multimodal domains identified by wide-field imaging (Fig. 3d), and consistent with anatomical projection patterns (Fig. 4b,c). As these clusters coincided with areas associated with the dorsal (A, RL) and ventral (AL, LI) streams, we used these designations moving forward. Due to their distinct functional properties, visuo-tactile neurons may facilitate cross-modal generalization. A Bayesian decoder trained to discriminate whisker stimuli based on individual neuronal responses was evaluated for generalization to visual stimuli (see Methods). Visuo-tactile neurons in associative areas uniquely enabled effective generalization across sensory modalities (see Fig. 5f). Other neuron types demonstrated significantly lower decoding accuracy when we tested their ability to

438 generalize the tactile discrimination to the visual modality, particularly with larger
439 populations (see Extended Data Fig. 11c-e). Therefore, visuo-tactile neuronal
440 population, displaying a prominent preference for spatially congruent combinations in
441 task-naïve mice, possesses the necessary properties to mediate goal-directed cross-
442 modal generalization if decoded by a downstream decision-related brain area[30]. This
443 suggests that cross-modal generalization might occur without the need for task-
444 induced synaptic plasticity in sensory circuits.

445 We further characterized the response properties of single neurons for visuo-
446 tactile stimuli in comparison with their responses predicted from unisensory responses
447 (Fig. 5b, see Methods). We found that bimodal neurons were typically tuned to
448 spatially congruent stimuli across both modalities. The example neuron in Figure 5b
449 responded preferentially to the bottom part of the visual field and to the bottom whisker.
450 Using unisensory responses, we predicted the response pattern to visuo-tactile stimuli
451 as the maximum response between the two modalities for each combination. When
452 comparing the predicted response with the measured one, we observed suppression
453 in incongruent combinations and enhancement in congruent ones. This nonlinear
454 modulation profile enables neurons to maintain their spatial selectivity independently
455 of the stimulated modality (visual, tactile, or visuo-tactile). This response property is
456 reminiscent of the supramodal encoding of object orientation reported in visuo-tactile
457 neurons of the rat posterior parietal cortex[6]. Population analysis confirmed that spatial
458 congruence in multisensory selectivity is prevalent among populations of multimodal
459 neurons in both the ventral and dorsal stream (Fig. 5g). Additionally, the two neuronal
460 populations exhibited sharper tuning for whisker and visual positions than that
461 predicted by their unisensory responses alone (Fig. 5h). Visuo-tactile neurons were
462 found in most mice in which imaging was performed in associative areas (18 mice out

463 of 22 for dorsal areas, 14 mice out of 17 for ventral areas). Strong multisensory
464 modulations, with a norm of the difference between observed and predicted selectivity
465 larger than 0.3 (Fig. 5h), were observed in a subset of these neurons (32 neurons out
466 of 124 found in 8 mice out of 18 for dorsal areas, 12 neurons out of 75 found in 6 mice
467 out of 14 for ventral areas). These modulations were significantly stronger in neurons
468 from dorsal areas compared to those from ventral areas (n=75 neurons for ventral
469 versus n=124 neurons for dorsal, unpaired two-sided t-test, ***$p=7.6x10^{-4}$ with average
470 norm difference = 0.203 ± 0.015 for ventral and average norm difference = 0.122 ±
471 0.018 for dorsal). In particular, neurons from the ventral domain displayed sharper
472 tuning for particular visual locations, whereas neurons in the dorsal domain exhibited
473 greater tuning to individual whiskers (Fig. 5i,j), consistent with modality preferences
474 observed in wide-field imaging data (Fig. 3d). These results showed that bimodal
475 neurons in visuo-tactile associative areas are indeed specifically responding to
476 spatially congruent visuo-tactile stimuli and therefore could mediate cross-modal
477 generalization during goal-directed tasks.

478

479 **Cross-modal generalization loss-of-function**

480 Cross-modal decodability of stimulus location observed at single-cell level (Fig. 5f),
481 alongside the anatomical connectivity between visual and whisker somatosensory
482 cortices (Fig. 4), suggest that associative visuo-tactile cortical areas could mediate
483 cross-modal generalization of goal-directed behaviors. We performed loss-of-function
484 experiments to assess the necessity of these areas for visuo-tactile generalization.
485 Given that task-naïve mice (those not yet exposed to any behavioral tasks) exhibited
486 co-aligned and anatomically connected spatial maps, we reasoned that the
487 reverberation of evoked responses across this extensive visuo-tactile network could

488 potentially drive learning processes beyond the initially stimulated modality. This could
489 facilitate cross-modal generalization before any direct exposure to the second task
490 with the other modality. Indeed, the existence of supramodal representations of space
491 in associative areas could shape sensorimotor circuits across sensory modalities that
492 share the same spatial properties during the learning of the first task. To prevent this
493 possibility, we decided to chronically silence associative cortical areas prior to any
494 sensorimotor learning. We virally expressed the tetanus toxin light chain (TeNT-P2A-
495 GFP) in ventral or dorsal areas, thereby preventing neurotransmitter vesicle release
496 in transfected neurons (Fig. 6a, see Methods). Neurons expressing TeNT also co-
497 expressed GFP, allowing comparison of the expression pattern with the fitted atlas
498 (Fig. 6b). After subtracting blood vessel patterns and comparing with the cranial
499 window before injection (see Methods), we characterized the extent of GFP
500 expression and overlap with different visuo-tactile areas (Extended Data Fig. 12a-d).
501 To ensure strong expression of TeNT to effectively suppress vesicle release in the
502 transfected neurons before the beginning of the behavioral training, we waited at least
503 four weeks after viral injections[31]. Mice learned the whisker discrimination task at the
504 same rate as control mice and reached expert performances comparable to those
505 observed in mice trained without TeNT expression (Fig. 6c, Extended Data Fig. 12a-
506 d). Additionally, mice expressing TeNT performed a comparable number of trials to
507 control mice (N=20 mice for control group, N=25 mice for TeNT group, unpaired two-
508 sided t-test, p=0.89). However, when switching to the visual task in the rule-preserving
509 condition, performance typically dropped to chance level (Fig. 6d,k).

510 To identify which visuo-tactile areas are necessary for cross-modal
511 generalization, we expressed TeNT-P2A-GFP in different cortical locations across
512 mice (see Methods). We were able to cover all visuo-tactile areas with varying degrees

513 of overlap with the expression of TeNT (Extended Data Fig. 12e). Injections performed
514 in ventral or dorsal associative areas resulted in comparable expression patterns at
515 the surface of the cortex after correcting for any obstruction caused at the edge of the
516 cranial window (Extended Data Fig. 12f). The extent of TeNT-P2A-GFP expression
517 varied across mice and could overlap with multiple areas, requiring correlative
518 analyses that accounted for these varying degrees of overlap or were independent of
519 specific areas. Taking advantage of this variability, we first calculated for each cortical
520 area the extent to which the overlap of its surface with TeNT expression correlated
521 with any decline in performance following a rule-preserving switch (Extended Data Fig.
522 12g). This analysis revealed that generalization impairment was significantly
523 correlated with TeNT expression in area RL only (Fig. 6e). Despite the proximity of RL
524 to S1 and V1 and the risk of inactivating these primary sensory cortices with TeNT,
525 we did not observe any significant correlation in these areas. To confirm this result,
526 we also performed an area-independent reverse correlation analysis mapping the
527 average TeNT coverage that evoked a complete impairment of cross-modal
528 generalization (see Methods). Here again, RL silencing was found to consistently
529 prevent cross-modal generalization, revealing that this associative area is necessary
530 for the transfer to occur (Fig. 6f). Grouping mice depending on whether TeNT
531 expression pattern was located in the dorsal or ventral stream (Fig. 6g,i), we confirmed
532 that dorsal stream silencing severely affected generalization performance (Fig. 6h),
533 leading to slower re-learning after rule-preserving switches. Although mice expressing
534 TeNT in RL initially failed to detect or discriminate visual stimuli after the task switch,
535 they regained performance in the visual task after several training sessions. This
536 indicates that despite a comparable capacity to perform the visual or tactile task, these
537 mice were not able to generalize learning across sensory modalities.

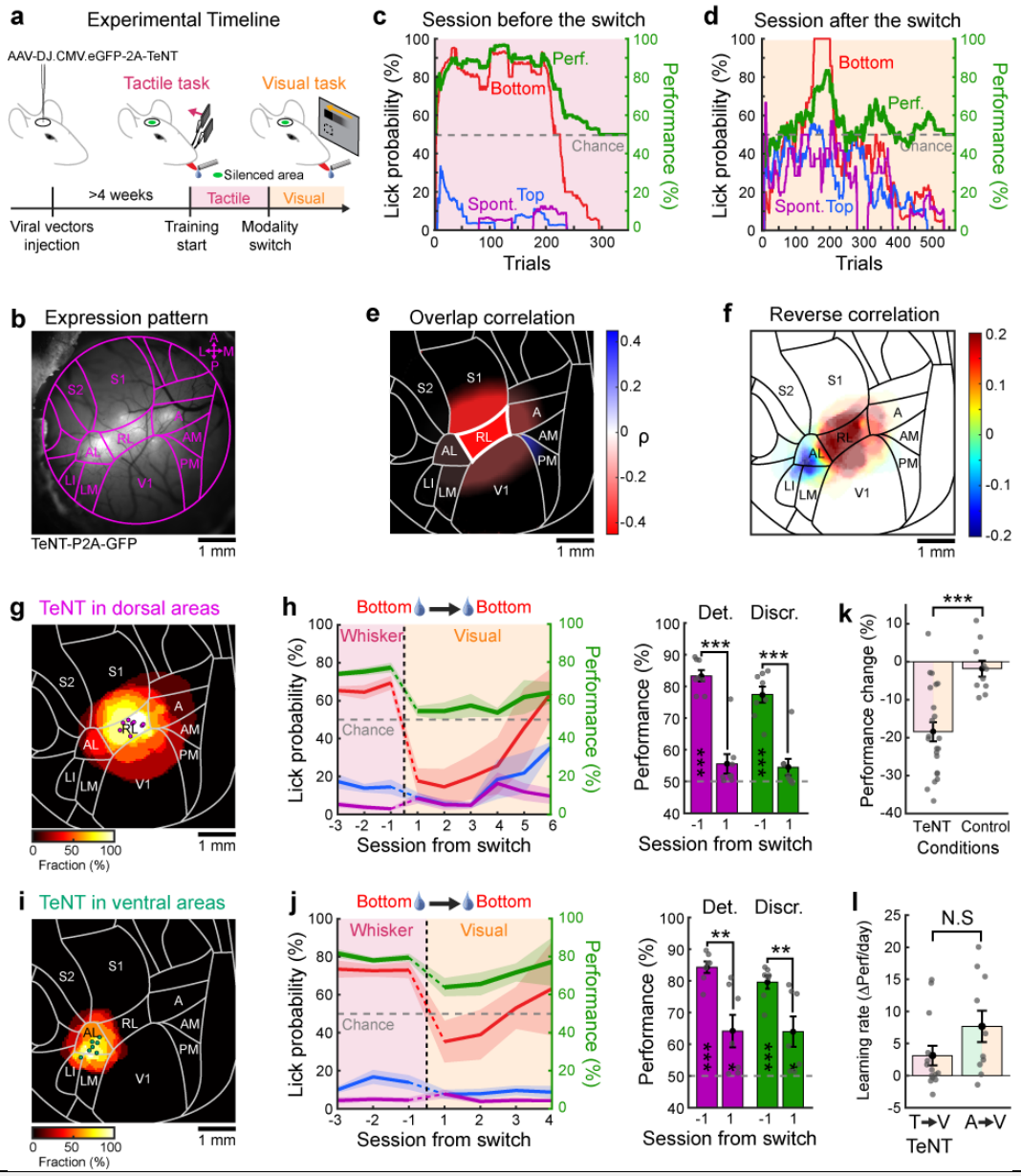

Fig. 6. Area RL is necessary for cross-modal generalization.

a, Schematic of the experimental timeline for loss-of-function experiments. **b,** Cranial window with expression of TeNT-P2A-GFP where viral vectors were injected. Atlas overlaid for reference. **c,** Example session before a rule-preserving modality switch from a tactile to a visual task. Color code as in Fig. 1d. **d,** Session following the modality switch. **e,** Area-based correlation between TeNT-P2A-GFP expression overlap and performance drop following modality switch. Color map indicates Pearson coefficients of correlation ρ. Areas with $p<0.05$ are indicated with a thick border (RL with $p=0.047$). **f,** Average TeNT-P2A-GFP coverage for mice with impaired cross-modal generalization (see Methods). The map is displayed after subtraction of the average coverage across all injected mice. **g,** Average TeNT-P2A-GFP coverage of all mice where only dorsal neurons were silenced (N=8 mice). Dots indicate center-of-mass location for each mouse. **h,** Left: Average task performance and conditional lick probabilities across sessions for mice in panel g with rule-preserving modality switch (vertical dashed line). Shaded area: S.E.M. Color code as in panel c. Right: Detection (purple) and discrimination (green) performance distribution the day before and after the switch (paired two-sided t-test comparing days, *$p<0.05$, **$p<0.01$, ***$p<0.001$, N.S. Not significant).

Performances are also tested against chance level (two-sided t-test, *p<0.05, **p<0.01, ***p<0.001, Blank: Not significant). **i,** Same as panel g but for TeNT-P2A-GFP expression in the ventral stream (N=7 mice). **j,** Same as panel h for ventral areas (paired two-sided t-test comparing days, *p<0.05, **p<0.01, ***p<0.001, N.S. Not significant). Performances are also tested against chance level (two-sided t-test, *p<0.05, **p<0.01, ***p<0.001, Blank: Not significant). **k,** Comparison of performance change following rule-preserving switch between all mice expressing TeNT-P2A-GFP and control mice described in Fig. 1e and Extended Data Fig. 1b (N=22 mice for TeNT and N=10 mice for control, two-sided unpaired t-test, ***$p=2.6x10^{-4}$). **l,** Learning rate estimated over the first three sessions following modality switch for mice expressing TeNT-P2A-GFP with impaired cross-modal generalization and control mice trained to the auditory task first described in Extended Data Fig. 1e-f (N=14 mice for TeNT and N=10 mice for control, two-sided unpaired t-test, N.S. p=0.11).

In contrast, inactivation of ventral areas slightly impaired performance immediately after a rule-preserving, although mice were performing on average well above chance level (Fig. 6j). One possible cause is the imprecision in estimating the expression pattern from the surface. The spread of expression within deeper layers, undetectable from the surface, could occasionally occur and affect nearby areas such as RL without being identified through wide-field imaging. These results suggests a very selective effect of RL silencing in impairing cross-modal generalization abilities but not unisensory skills.

We further assessed how silencing area RL with TeNT affects task performance following rule-reversing modality switch (Extended Data Fig. 13a-b). Following the switch, their performance fell to chance level but recovered faster than what we observed for control mice (Extended Data Fig. 13c). To fully characterize the learning rate following modality switches in TeNT-expressing mice, we focused on all mice that exhibited complete generalization impairment (i.e. displaying performance near chance level on the first session following the switch regardless of whether the condition was rule-reversing or rule-preserving). For these mice, we quantified the re-learning rate over several sessions following the modality switch and observed that the distribution was comparable to that seen during non-spatial auditory-to-visual

585 switches (Fig. 6l). This implies that silencing area RL prevents mice from applying prior
586 knowledge about the spatial task rule, whether it is conflicting or congruent with the
587 new task rule, resulting in the mice learning the visual task without prior spatial
588 knowledge.

589

590 **Optogenetic sensory substitution for cross-modal generalization**

591 To determine whether cortical area RL is not only necessary, but also sufficient
592 for visuo-tactile generalization, we conducted gain-of-function experiments by
593 substituting visual stimuli after modality switch with direct optogenetic stimulations of
594 RL top- and bottom- encoding subregions (Fig. 7a). Projections from primary sensory
595 areas to the ventral and dorsal visuo-tactile stream being largely distinct (Extended
596 Data Fig. 8h-j), we assumed that optogenetic activations of RL would remain restricted
597 mostly to the dorsal stream. Functional mapping was first performed to identify
598 domains of RL encoding top and bottom visual stimuli in Ai32 transgenic mice
599 expressing Cre-dependent ChR2-eYFP. Viral vectors AAV1.CaMKIIa.Cre were then
600 injected in this area to broadly express ChR2-eYFP in RL (Fig. 7b). We employed a
601 projector-based microscope to precisely shape blue light patterns, selectively exciting
602 subregions of RL that encode top and bottom stimuli. This approach allowed us to
603 substitute visual stimuli in the upper or lower visual field with precise spatio-temporal
604 optostimulations following the modality switch (see Methods). Based on the properties
605 and location of single neurons measured through two-photon imaging (Fig. 5f), we
606 estimated that approximately 65% of RL visuo-tactile neurons with generalizing

607 properties were activated by these blue light patterns, with roughly 40% located in the

608 bottom region and 25% in the top region.

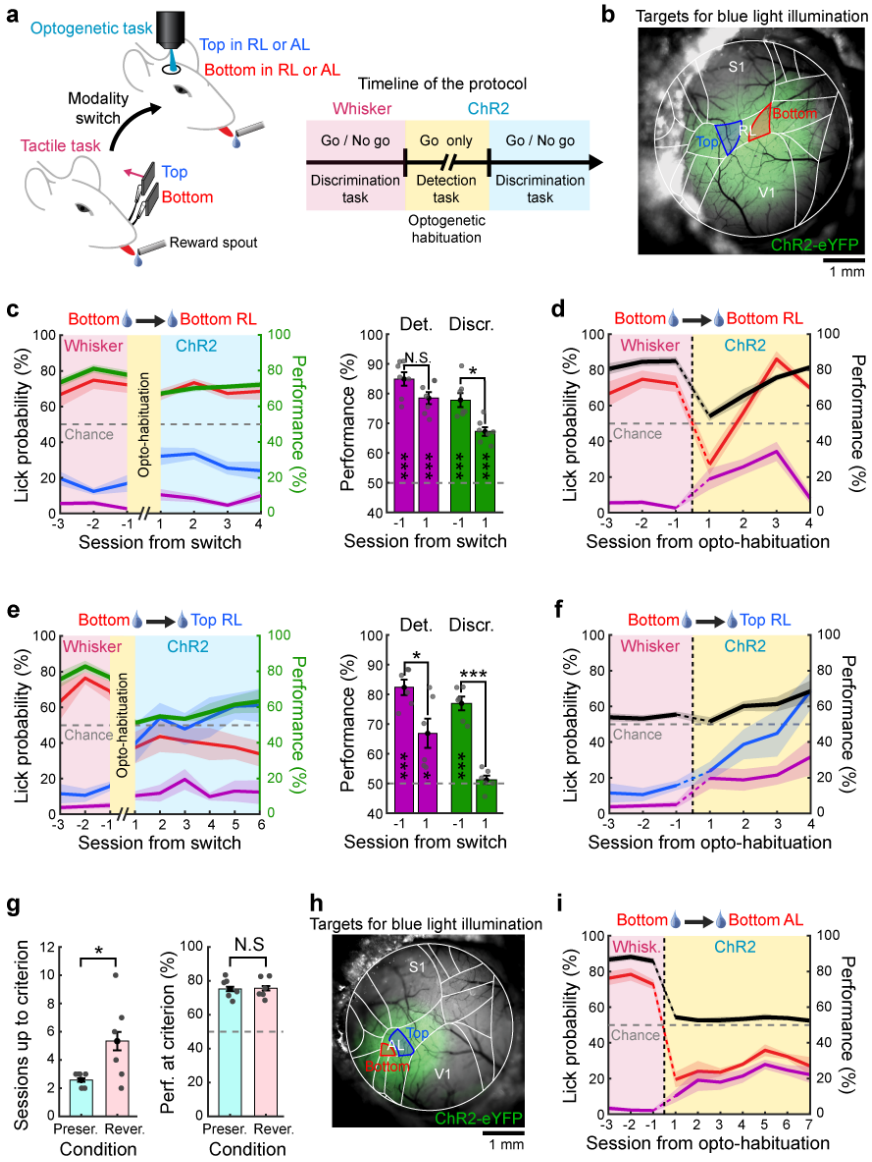

609 **Fig. 7. Area RL is sufficient for cross-modal generalization.**

610 **a,** Schematic of the behavioral experiment with direct ChR2-mediated optostimulations of RL
611 subregions following modality switch. **b,** Example cranial window of an Ai32 mouse expressing
612 ChR2-eYFP after injection of AAV1.CaMKIIa.Cre viral vectors in area RL. Atlas overlaid for
613 reference. Subregions of RL encoding top or bottom stimuli are indicated in blue or red,
614 respectively. Blue light patterns are shaped to match these subregions (see Methods). **c,** Left:
615 Average task performance and conditional lick probabilities across sessions for mice
616 experiencing a rule-preserving modality switch from the whisker task to the optogenetic task
617 (N=7 mice). Right: detection (purple) and discrimination (green) performance distribution the
618 session before and after the switch (paired two-sided t-test comparing days, *p<0.05,
619 **p<0.01, ***p<0.001, N.S. Not significant). Performances are also tested against chance level
620 (two-sided t-test, *p<0.05, **p<0.01, ***p<0.001, Blank: Not significant). **d,** Average detection
621 performance (black) and conditional lick probability for the bottom stimulus (red) or in the

absence of stimuli (purple) across sessions for mice switching from the whisker task to the habituation phase to respond to optogenetic stimulations in the bottom-encoding part of RL. **e,** Same as panel c but for mice undergoing a rule-reversing switch (N=6 mice, paired two-sided t-test comparing days, *p<0.05, **p<0.01, ***p<0.001, N.S. Not significant). **f,** Same as panel d but for mice undergoing habituation to respond to optogenetic stimulations in the top-encoding part of RL. **g,** Left: Comparison of the number of sessions required to reach the detection criterion between mice undergoing a rule-preserving switch and those undergoing a rule-reversing switch (unpaired two-sided t-test, *p<0.05). Right: Comparison of detection performance at the end of the optogenetic habituation phase (unpaired two-sided t-test, p=0.88). **h,** Same as panel b but for optogenetic stimulations of area AL. **i,** Same as panel d but for optogenetic stimulations of AL. The detection criterion was never reached during this habituation phase.

Before switching to the full optogenetic substitution task, mice that had achieved stable expert performance in the tactile task first underwent optogenetic habituation sessions (Fig. 7a). During these sessions, they were exposed exclusively to the Go light pattern, with a distribution of 80% Go trials and 20% Catch trials with blue light stimulations outside the cranial window. Once mice exhibited a consistent licking response to optogenetic stimulations, they were transitioned to the full task, which included No go trials. This step was necessary, as stimulations of higher-order sensory areas may induce unfamiliar modulations of perceptual experience rather than generating new percepts[32–34], making them more difficult to be detected. We assessed the ability of mice to generalize previously learned sensorimotor associations from the whisker task to the optogenetic task, both when the spatial rule was preserved or reversed. Following rule-preserving modality switch, mice maintained a comparable level of discrimination performance once No go trials were introduced (Fig. 7c). During the opto-habituation phase, these mice quickly learned to respond to optogenetic stimulations (Fig. 7d). In contrast, mice undergoing the rule-reversing modality switch performed at chance level after the No go stimuli were introduced and gradually relearned the task in the following sessions (Fig. 7e). Additionally, they were significantly slower to respond to optogenetic stimulation

653 during the habituation phase (Fig. 7f), taking roughly twice as long to reach the same
654 level of responsiveness (Fig. 7g). This is most likely due to the spatial prior inherited
655 from the tactile task, which associated the top stimuli with a time-out punishment. This
656 suggests that activity in RL alone is sufficient to induce cross-modal generalization,
657 once mice habituated to optogenetic stimulations. To further confirm that this function
658 was specific to RL, we performed the same experiment targeting area AL of the ventral
659 stream (Fig. 7h), which also contains visuo-tactile neurons (Fig. 5e). Optogenetic
660 activation of AL failed to evoke behavioral responses for at least 7 consecutive days,
661 even when stronger blue light intensities were used or when larger light patterns
662 matching the size of those used over RL were applied (Fig. 7i).

663

664 **Network model for generalized sensorimotor learning**

665 Based on our experimental findings on the functional and anatomical
666 organization of visuo-tactile cortical circuits, as well as the effect of RL silencing on
667 cross-modal generalization, we developed a network model to recapitulate the
668 behavior we observed in mice. Our model included areas V1, S1, RL and AL, each
669 comprising two recurrent networks of excitatory and inhibitory neurons encoding "top"
670 or "bottom" spatial location, respectively (Fig. 8a). Although areas RL and AL exhibit
671 comparable functional properties, their cortical connectivity differs markedly.
672 Estimations of cortico-cortical connectivity reported by Wang and colleagues[35] indicate
673 that RL shows stronger feedback projections to S1/V1 and robustly connects to the
674 premotor cortex (M2), which is critical for sensorimotor transformation[20]. In contrast,
675 AL has limited feedback projections to primary sensory areas and very weak
676 connectivity to M2. Based on these observations, in the model only areas S1, V1 and
677 RL projected to reward-modulated decision variables representing a downstream

motor area such as M2. Additionally, feedback projections from AL to V1 and S1 were modeled as much weaker than those from RL. Training the model on the whisker discrimination task involved external inputs to S1 (representing thalamic inputs) and reward-modulated learning via Hebbian plasticity of the sensorimotor connections (see Methods). In line with our experimental observations, we modeled the sensory cortices such that populations encoding top or bottom stimuli could communicate bidirectionally with populations in associative areas encoding the same spatial locations. This model architecture produces visuo-tactile neuronal populations in RL and AL that were tuned exclusively to spatially congruent visuo-tactile stimuli. Synaptic connections between sensory cortices were not subjected to plasticity, as only the synaptic plasticity of sensorimotor connections was necessary to learn the association between the Go stimuli and the corresponding action following a reward. Model simulations showed that after switching inputs from S1 to V1, mimicking a rule-preserving switch from the tactile to the visual modality, performance remained stable (Fig. 8b). However, if the spatial rule of the task was reversed upon modality switch, performance dropped below chance level and then slowly recovered (Fig. 8c). This delay in performance recovery was due to the model weights needing to override the previously learned structure before learning the new association. Mimicking the loss-of-function experiments, we silenced the area RL in the model during training, causing the neural network to learn the visual task from scratch after the rule-preserving switch without any spatial prior in the weight structure (Fig. 8d). The absence of strong connections between the primary sensory areas prevented ongoing learning in the non-stimulated area. The model suggests that the activity reverberation mediated by bidirectional connections with area RL induces a consistent weight structure across connected areas. These weights, however, needed to be reorganized following a rule-

reversing modality switch, leading to delayed relearning time (Extended Data Fig. 14a-d).

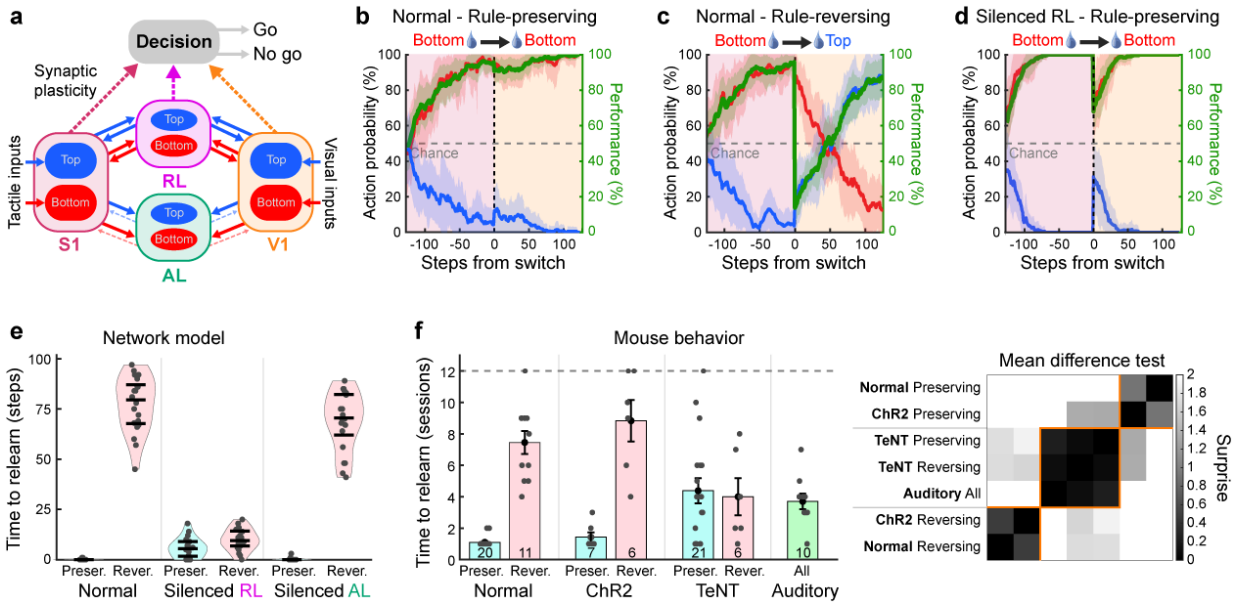

Fig.8. Neural network architecture for cross-modal generalization.

a, Schematic of the neural network model for cross-modal generalization. Synapses projecting to the decision-computing area are the ones undergoing synaptic plasticity during sensorimotor learning. Feedback projections from area AL (dashed lines) are one tenth of the strength of feedback projections from RL (see Methods). **b,** Action probability conditional on inputs to S1 before, and inputs to V1 after, a rule-preserving modality switch (vertical dashed line). Red: rewarded bottom stimulations, blue: non-rewarded top stimulations. Green: Discrimination performance. Shaded areas: standard deviation with n=20 simulations. **c,** Same as panel b after a rule-reversing modality switch. **d,** Same as panel b with silenced RL. **e,** Number of steps necessary to cross a performance threshold of 75% in the full network model (left) or in the model with silenced RL (middle) or silenced AL (right) after rule-preserving or rule-reversing modality switches (n=20 simulations). Error bars indicate median, first and third quartiles. **f,** Left: Number of sessions needed to cross a performance threshold of 65% following the modality switch. Training was stopped after 12 sessions (dashed line) and mice that did not reach the criteria before this session are plotted on the dashed line. Mice numbers are indicated for each group at the bottom of the bar. Error bars: S.E.M. Right: Surprise matrix computed from pairwise unpaired two-sided t-test between conditions. A hierarchical clustering based on cosine similarity was used to group conditions based on surprise values.

To quantify the effect of different task conditions in the learning trajectory following modality switch in the model, we computed the time needed in simulation steps to recover expert level. Following a rule-preserving modality switch, the time to relearn was near-instantaneous whereas it was much longer following rule-reversing

729 switches (Fig. 8e). Interestingly, when RL was silenced, the time to relearn was in-
730 between these two distributions reflecting that the model learned the task from scratch
731 (Fig. 8e). Silencing area AL, however, had no impact on task generalization. This result
732 remained consistent as long as AL feedback strength was very weak compared to RL
733 (Extended Data Fig. 14e). Therefore, this network model recapitulates cross-modal
734 generalization and offers mechanistic insights into the circuit organization and synaptic
735 plasticity required for sensorimotor learning, providing testable hypotheses for further
736 experimental validation. Finally, we compared these results to the time needed to
737 relearn the task after modality switch in all conditions used with our mice (Fig. 8f). In
738 line with the model, mice rapidly recovered high-performance levels after a rule-
739 preserving modality switch. In contrast, time to relearn the task was dramatically
740 prolonged following rule-reversing switches. This was true for both visual stimuli and
741 optostimulations following the switch. In TeNT-expressing mice, however, the time to
742 relearn the task was moderate and similar for both rule-preserving and rule-reversing
743 modality switches. Importantly, the time to relearn in these mice was comparable to
744 the time needed to reach expert level in the auditory task in absence of any spatial
745 prior, reminiscent of the "RL silenced" case in the model. The distribution of peak
746 performance observed for our mice was mostly determined by the nature of the
747 sensory inputs after the switch rather than the switch type (Extended Data Fig. 15).

748

749 **Discussion**

750 Our results elucidate the cortical architecture underlying the abstract
751 representation of peri-personal space in mice. We identified the specific cortical circuit
752 that enables rapid generalization of sensorimotor associations learned from one

753 modality to another, forming the neural substrate for a key component of flexible
754 behavior.

755 Cross-modal generalization has been reported across numerous species
756 including apes[3], rodents[2] and, more recently, bumblebees[4]. Early research into the
757 mammalian brain circuits involved in cross-modal generalization underscores the
758 necessity of different brain structures to process different types of information such as
759 spatial, temporal, and object-related features[23,36,37]. The posterior parietal cortex
760 (PPC) plays an important role in processing spatial information[38,39]. Our results point
761 out that area RL, a subregion of PPC, is crucial for cross-modal generalization based
762 on abstract representations of peri-personal space. Area RL displays visuo-tactile
763 neuronal responses[19] and is implicated in whisking movements control[40]. It is
764 strategically positioned between the primary visual cortex and the primary whisker
765 somatosensory cortex, facilitating bidirectional information transfer between these
766 sensory systems. Area RL possesses a retinotopic map biased towards the lower part
767 of the visual field[24] where most whiskers are visible, and its neurons are tuned to high
768 binocular disparity, aligning with objects in close proximity, potentially within whiskers'
769 reach[41]. It was also implicated in optic flow processing[42] while its contribution to high-
770 order motion computations remains debated[43,44]. Our findings unveil a fundamental
771 functional specialization of area RL, confirming its unique role in facilitating visuo-
772 tactile coordination and sensory abstraction in the peri-personal space. Future
773 research could elucidate how this area may contribute to sensorimotor integration
774 during active multimodal exploration of nearby objects, similar to multimodal limb
775 posture encoding observed in the primate PPC[45].

776 Other forms of cross-modal generalization, such as object recognition, may
777 engage different cortical regions. Indeed, areas of the dorsal stream are classically

associated with spatial, attentional, and motion processing or motor guidance, while areas of the ventral stream are involved in object recognition. Previous studies have reported visuo-tactile multimodal responses in both the ventral and dorsal pathway in primates[46–48], including areas initially thought to be exclusive to visual processing like V4[49] and MT/V5[50]. Our study uncovered visuo-tactile areas belonging to the ventral or dorsal stream in mice[35,51]. Specifically, RL and A are typically associated to the dorsal stream while LI, with its significant projection to the postrhinal (POR) cortex, is associated with the ventral stream[35]. Lesions in the perirhinal cortex in rats, downstream to POR, obstruct cross-modal object recognition during spontaneous exploration[36]. Moreover, areas LI and AL have been functionally characterized as specialized for shape processing and object recognition[52,53], suggesting that they could represent a rodent homologue of the visuo-haptic subregion of the lateral occipital complex (LOtv) reported in human fMRI studies[46]. These reports suggest that the ventral pathway might contribute specifically to cross-modal object recognition. Future research focusing on objects discrimination could provide further insight into the specific role of visuo-tactile areas in the ventral stream.

Cross-modal generalization involving other sensory modalities has been observed using amodal properties such as stimulus duration or intensity[2]. Notably, rodents can generalize behaviors based on shared features between audition and vision[54,55], although the precise circuit identity and organization required for this process remain unclear. Importantly, lesions in the posterior parietal cortex, which includes area RL, have been shown to impair behaviors relying on spatial information but not those involving non-spatial information[23]. While several other brain regions such as the prefrontal cortex or temporal associate areas may contribute to non-spatial

802 cross-modal generalization, the exact circuit organization of these regions remains to
803 be explored[2].

804 Our wide-field imaging and anatomical mapping experiments revealed a more
805 extensive and organized network of visuo-tactile associative cortical areas than
806 previously identified[19,35,56], where many associative areas exhibited a shared
807 representation of vertical space between visual and whisker tactile inputs. These
808 spatial maps extended even to primary sensory cortices through associative areas,
809 with strong responses observed in S1 following visual stimulations despite no direct
810 projections between V1 and S1[28]. Our data suggest that the asymmetrical propagation
811 of activity between the visual and whisker somatosensory cortices could originate from
812 denser populations of neurons in V1 projecting to the associative area RL compared
813 to those in S1. However, our model suggests that this asymmetry in feedforward
814 projections does not prevent bidirectional cross-modal generalization (Extended Data
815 Fig. 14f). Although recent findings advise caution in interpreting cross-modal signals
816 between primary cortical areas due to potential confusion with signals evoked by
817 uninstructed movements[27], our results suggest that certain fundamental features, such
818 as spatial location, indeed have a shared representations across various cortical areas.
819 These representations possibly support object or event-oriented abstract encoding[57]
820 for cross-modal generalized learning. Organized feedback projections from
821 associative areas to primary sensory cortices appear to play an unsuspected role for
822 learning, in addition to their known role in shaping functional properties with contextual
823 information[58]. This raises the question of whether the same or different feedback
824 projections subserve these functions.

825 Consistent with the literature on multisensory integration[59], we observed multisensory
826 modulations that enhanced responses to spatially congruent visuo-tactile stimuli and

827 suppressed responses to incongruent stimuli. This response pattern could potentially
828 result from surround suppression for incongruent inputs, mediated by local
829 parvalbumin-positive interneurons as observed for conflicting visuo-auditory stimuli[12] ,
830 while a distinct mechanism could specifically enhance responses to spatially
831 congruent inputs. By comparing congruent to incongruent combinations, we
832 uncovered multisensory modulation rules that shape a supramodal representation of
833 peri-personal space. Supramodal encoding of gratings orientation was reported in
834 neurons of the rat PPC in response to visuo-tactile stimuli[6] despite a lack of organized
835 functional maps for orientation selectivity in rodents. The development of congruent
836 supramodal tuning in single neurons and overlapping spatial maps, as observed in
837 naive animals, likely arises from an interplay of genetically encoded connectivity
838 biases and activity-dependent mechanisms. Biased connectivity, combined with
839 correlated spontaneous activity in sensory areas like V1 and S1, appears to refine
840 map alignment in regions such as mouse RL, potentially through Hebbian plasticity[60].
841 Similarly, in the superior colliculus, early cross-modal experiences refine coarse,
842 overlapping modality-specific maps through Hebbian plasticity acting on sensory-
843 evoked activity, with critical input from multisensory cortical regions[18,61]. These
844 findings suggest that both spontaneous activity and sensory experience contribute to
845 the maturation of multisensory integration. For example, after cataract removal,
846 individuals initially struggle to integrate visual and haptic cues but rapidly develop
847 optimal multisensory strategies with experience, demonstrating remarkable plasticity
848 of these circuits even in the adult brain[62]. This adaptability raises intriguing questions
849 about how multisensory representations in mouse RL might adjust to altered visuo-
850 tactile contingencies, which could be experimentally tested through controlled
851 manipulations of sensory co-occurrence statistics[63]. New experiments could provide

deeper insights into the role of experience in shaping multisensory processing across developmental and adult stages.

Information generalization across modalities is crucial not only for biological brains but also for artificial systems. With the advent of multimodal large language models such as GPT-4o and Gemini, it is widely recognized that multimodality is fundamental for general artificial intelligence[64,65] and can lead to the emergence of abstract conceptual representations in machine learning systems[66]. We believe that the supramodal encoding of peri-personal space by multisensory neurons we reported could represent an early instance of the same computational mechanism leading to the emergence of conceptual representations[9,30] that form the building blocks of flexible mental representations known as cognitive maps[1]. In this light, our work represents a major step toward understanding the circuit architecture of one of the most fundamental cognitive computations: sensory abstraction.

References

1. Behrens, T. E. J. *et al.* What Is a Cognitive Map? Organizing Knowledge for Flexible Behavior. *Neuron* **100**, 490–509 (2018).

2. Cloke, J. M., Jacklin, D. L. & Winters, B. D. The neural bases of crossmodal object recognition in non-human primates and rodents: A review. *Behavioural Brain Research* **285**, 118–130 (2015).

3. Davenport, R. K. & Rogers, C. M. Intermodal Equivalence of Stimuli in Apes. *Science* **168**, 279–280 (1970).

4. Solvi, C., Gutierrez Al-Khudhairy, S. & Chittka, L. Bumble bees display cross-modal object recognition between visual and tactile senses. *Science* **367**, 910–912 (2020).

5. Bruck, J. N. & Pack, A. A. Understanding across the senses: cross-modal studies of cognition in cetaceans. *Anim Cogn* **25**, 1059–1075 (2022).

6. Nikbakht, N., Tafreshiha, A., Zoccolan, D. & Diamond, M. E. Supralinear and Supramodal Integration of Visual and Tactile Signals in Rats: Psychophysics and Neuronal Mechanisms. *Neuron* **97**, 626-639.e8 (2018).

7. Samborska, V., Butler, J. L., Walton, M. E., Behrens, T. E. J. & Akam, T. Complementary task representations in hippocampus and prefrontal cortex for generalizing the structure of problems. *Nat Neurosci* **25**, 1314–1326 (2022).

8. Miller, E. K., Nieder, A., Freedman, D. J. & Wallis, J. D. Neural correlates of categories and concepts. *Curr Opin Neurobiol* **13**, 198–203 (2003).

9. Quiroga, R. Q., Reddy, L., Kreiman, G., Koch, C. & Fried, I. Invariant visual representation by single neurons in the human brain. *Nature* **435**, 1102–1107 (2005).

10. Garner, A. R. & Keller, G. B. A cortical circuit for audio-visual predictions. *Nat Neurosci* **25**, 98–105 (2022).

11. Godenzini, L. *et al.* Auditory input enhances somatosensory encoding and tactile goal-directed behavior. *Nat Commun* **12**, (2021).

12. Song, Y. H. *et al.* A Neural Circuit for Auditory Dominance over Visual Perception. *Neuron* **93**, 940-954.e6 (2017).

13. Weiler, S. *et al.* A primary sensory cortical interareal feedforward inhibitory circuit for tacto-visual integration. *Nat Commun* **15**, 3081 (2024).

14. Jenkinson, E. W. & Glickstein, M. Whiskers, barrels, and cortical efferent pathways in gap crossing by rats. *J Neurophysiol* **84**, 1781–1789 (2000).

15. Sofroniew, N. J., Cohen, J. D., Lee, A. K. & Svoboda, K. Natural whisker-guided behavior by head-fixed mice in tactile virtual reality. *Journal of Neuroscience* **34**, 9537–9550 (2014).

16. Drager, U. C. & Hubel, D. H. Physiology of visual cells in mouse superior colliculus and correlation with somatosensory and auditory input. *Nature* **253**, 203–204 (1975).

17. Drager, U. C. & Hubel, D. H. Topography of visual and somatosensory projections to mouse superior colliculus. *J Neurophysiol* **39**, 91–101 (1976).

910 18. Stein, B. E., Stanford, T. R. & Rowland, B. A. Development of multisensory
911 integration from the perspective of the individual neuron. *Nat Rev Neurosci* **15**,
912 520–535 (2014).

913 19. Olcese, U., Iurilli, G. & Medini, P. Cellular and synaptic architecture of
914 multisensory integration in the mouse neocortex. *Neuron* **79**, 579–593 (2013).

915 20. Matteucci, G. *et al.* Cortical sensory processing across motivational states during
916 goal-directed behavior. *Neuron* **110**, 4176-4193.e10 (2022).

917 21. Chéreau, R. *et al.* Dynamic perceptual feature selectivity in primary
918 somatosensory cortex upon reversal learning. *Nat Commun* **11**, 3245 (2020).

919 22. Banerjee, A. *et al.* Value-guided remapping of sensory cortex by lateral
920 orbitofrontal cortex. *Nature* **585**, 245–250 (2020).

921 23. Tees, R. The effects of posterior parietal and posterior temporal cortical lesions
922 on multimodal spatial and nonspatial competencies in rats. *Behavioural Brain*
923 *Research* **106**, 55–73 (1999).

924 24. Zhuang, J. *et al.* An extended retinotopic map of mouse cortex. *Elife* **6**, 1–29
925 (2017).

926 25. Yamashita, T. *et al.* Diverse Long-Range Axonal Projections of Excitatory Layer
927 2/3 Neurons in Mouse Barrel Cortex. *Front Neuroanat* **12**, (2018).

928 26. Choi, I., Lee, J.-Y. & Lee, S.-H. Bottom-up and top-down modulation of
929 multisensory integration. *Curr Opin Neurobiol* **52**, 115–122 (2018).

930 27. Bimbard, C. *et al.* Behavioral origin of sound-evoked activity in mouse visual
931 cortex. *Nat Neurosci* **26**, 251–258 (2023).

932 28. Wang, Q. & Burkhalter, A. Area map of mouse visual cortex. *Journal of*
933 *Comparative Neurology* **502**, 339–357 (2007).

934 29. Morimoto, M. M., Uchishiba, E. & Saleem, A. B. Organization of feedback
935 projections to mouse primary visual cortex. *iScience* **24**, (2021).

936 30. Bernardi, S. *et al.* The Geometry of Abstraction in the Hippocampus and Prefrontal
937 Cortex. *Cell* **183**, 954-967.e21 (2020).

938 31. Zingg, B., Peng, B., Huang, J., Tao, H. W. & Zhang, L. I. Synaptic Specificity and
939 Application of Anterograde Transsynaptic AAV for Probing Neural Circuitry. *The*
940 *Journal of Neuroscience* **40**, 3250–3267 (2020).

941 32. Azadi, R. *et al.* Image-dependence of the detectability of optogenetic stimulation
942 in macaque inferotemporal cortex. *Current Biology* **33**, 581-588.e4 (2023).

943 33. Parvizi, J. *et al.* Electrical Stimulation of Human Fusiform Face-Selective Regions
944 Distorts Face Perception. *The Journal of Neuroscience* **32**, 14915–14920 (2012).

945 34. Murphey, D. K., Maunsell, J. H. R., Beauchamp, M. S. & Yoshor, D. Perceiving
946 electrical stimulation of identified human visual areas. *Proceedings of the National*
947 *Academy of Sciences* **106**, 5389–5393 (2009).

948 35. Wang, Q., Sporns, O. & Burkhalter, A. Network analysis of corticocortical
949 connections reveals ventral and dorsal processing streams in mouse visual
950 cortex. *Journal of Neuroscience* **32**, 4386–4399 (2012).

951 36. Winters, B. D. & Reid, J. M. A Distributed Cortical Representation Underlies
952 Crossmodal Object Recognition in Rats. *The Journal of Neuroscience* **30**, 6253–
953 6261 (2010).

954 37. Yeterian, E. H. The effects of visual or auditory cortical lesions on specific cross-
955 modal transfer in the rat. *Neuropsychologia* **15**, 517–527 (1977).

956 38. Whitlock, J. R. Posterior parietal cortex. *Current Biology* **27**, R691–R695 (2017).

957 39. Pasalar, S., Ro, T. & Beauchamp, M. S. TMS of posterior parietal cortex disrupts
958 visual tactile multisensory integration. *European Journal of Neuroscience* **31**,
959 1783–1790 (2010).

960 40. Mohan, H. *et al.* Functional Architecture and Encoding of Tactile Sensorimotor
961 Behavior in Rat Posterior Parietal Cortex. *The Journal of Neuroscience* **39**, 7332–
962 7343 (2019).

963 41. La Chioma, A., Bonhoeffer, T. & Hübener, M. Area-Specific Mapping of Binocular
964 Disparity across Mouse Visual Cortex. *Current Biology* **29**, 2954-2960.e5 (2019).

965 42. Rasmussen, R. N., Matsumoto, A., Arvin, S. & Yonehara, K. Binocular integration of
966 retinal motion information underlies optic flow processing by the cortex. *Current*
967 *Biology* **31**, 1165-1174.e6 (2021).

968 43. Matteucci, G., Bellacosa Marotti, R., Zattera, B. & Zoccolan, D. Truly pattern:
969 Nonlinear integration of motion signals is required to account for the responses
970 of pattern cells in rat visual cortex. *Sci Adv* **9**, (2023).

971 44. Sit, K. K. & Goard, M. J. Distributed and retinotopically asymmetric processing of
972 coherent motion in mouse visual cortex. *Nat Commun* **11**, 3565 (2020).

973 45. Graziano, M. S. A., Cooke, D. F. & Taylor, C. S. R. Coding the Location of the Arm by
974 Sight. *Science* **290**, 1782–1786 (2000).

975 46. Amedi, A., Malach, R., Hendler, T., Peled, S. & Zohary, E. Visuo-haptic object-
976 related activation in the ventral visual pathway. *Nat Neurosci* **4**, 324–330 (2001).

977 47. James, T. W. & Kim, S. Dorsal and Ventral Cortical Pathways for Visuo-haptic
978 Shape Integration Revealed Using fMRI. in *Multisensory Object Perception in the*
979 *Primate Brain* 231–250 (Springer New York, New York, NY, 2010).

980 48. Lacey, S. & Sathian, K. Visuo-haptic multisensory object recognition,
981 categorization, and representation. *Front Psychol* **5**, (2014).

982 49. Maunsell, J. H. R., Sclar, G., Nealey, T. A. & DePriest, D. D. Extraretinal
983 representations in area V4 in the macaque monkey. *Vis Neurosci* **7**, 561–573
984 (1991).

985 50. Hagen, M. C. *et al.* Tactile motion activates the human middle temporal/V5
986 (MT/V5) complex. *European Journal of Neuroscience* **16**, 957–964 (2002).

987 51. Marshel, J. H., Garrett, M. E., Nauhaus, I. & Callaway, E. M. Functional specialization
988 of seven mouse visual cortical areas. *Neuron* **72**, 1040–1054 (2011).

989 52. Tafazoli, S. *et al.* Emergence of transformation-tolerant representations of visual
990 objects in rat lateral extrastriate cortex. *Elife* **6**, (2017).

991 53. Froudarakis, E. *et al.* Object manifold geometry across the mouse cortical visual
992 hierarchy. *BioRxiv* Preprint at https://doi.org/10.1101/2020.08.20.258798
993 (2020).

994 54. Over, R. & Mackintosh, N. J. Cross-modal Transfer of Intensity Discrimination by
995 Rats. *Nature* **224**, 918–919 (1969).

55. Delay, E. R. Effects of cross-modal transfer on direct and reversal learning in the rat. *Anim Learn Behav* **14**, 427–434 (1986).

56. Caron-Guyon, J. *et al.* Neuronal encoding of multisensory motion features in the rat associative parietal cortex. *Cerebral Cortex* **30**, 5372–5386 (2020).

57. Ghazanfar, A. A. & Schroeder, C. E. Is neocortex essentially multisensory? *Trends Cogn Sci* **10**, 278–285 (2006).

58. Keller, A. J., Roth, M. M. & Scanziani, M. Feedback generates a second receptive field in neurons of the visual cortex. *Nature* **582**, 545–549 (2020).

59. Stein, B. E. & Stanford, T. R. Multisensory integration: Current issues from the perspective of the single neuron. *Nat Rev Neurosci* **9**, 255–266 (2008).

60. Dwulet, J. M. *et al.* Correlated spontaneous activity sets up multi-sensory integration in the developing higher-order cortex. *Elife* (2024) doi:10.7554/eLife.101713.1.

61. Cang, J. & Feldheim, D. A. Developmental Mechanisms of Topographic Map Formation and Alignment. *Annu Rev Neurosci* **36**, 51–77 (2013).

62. Senna, I. *et al.* Development of multisensory integration following prolonged early-onset visual deprivation. *Current Biology* **31**, 4879-4885.e6 (2021).

63. Matteucci, G., Piasini, E. & Zoccolan, D. Unsupervised learning of mid-level visual representations. *Curr Opin Neurobiol* **84**, 102834 (2024).

64. Fu, L. *et al.* A Touch, Vision, and Language Dataset for Multimodal Alignment. *ArXiv* (2024) doi:10.48550/arXiv.2402.13232

1017 65. Wu, J., Gan, W., Chen, Z., Wan, S. & Yu, P. S. Multimodal Large Language Models: A
1018 Survey. *ArXiv* (2023) doi:10.48550/arXiv.2311.13165

1019 66. Goh, G. *et al.* Multimodal Neurons in Artificial Neural Networks. *Distill* **6**, (2021).

1020 67. Lein, E. S. *et al.* Genome-wide atlas of gene expression in the adult mouse brain.
1021 *Nature* **445**, 168–176 (2007).

1022 68. Pachitariu, M. *et al.* Suite2p: beyond 10,000 neurons with standard two-photon
1023 microscopy. *bioRxiv* 061507 (2016) doi:10.1101/061507.

1024 69. Wallace, M. T., Meredith, M. A. & Stein, B. E. Multisensory Integration in the
1025 Superior Colliculus of the Alert Cat. *J Neurophysiol* **80**, 1006–1010 (1998).

1026 70. Jazayeri, M. & Movshon, J. A. Optimal representation of sensory information by
1027 neural populations. *Nat Neurosci* **9**, 690–696 (2006).

1028 71. Ma, W. J., Beck, J. M., Latham, P. E. & Pouget, A. Bayesian inference with
1029 probabilistic population codes. *Nat Neurosci* **9**, 1432–1438 (2006).

1030 72. Boyden, E. S., Zhang, F., Bamberg, E., Nagel, G. & Deisseroth, K. Millisecond-
1031 timescale, genetically targeted optical control of neural activity. *Nat Neurosci* **8**,
1032 1263–1268 (2005).

1033 73. Efron, B. & Tibshirani, R. J. *An Introduction to the Bootstrap*. (Chapman and
1034 Hall/CRC, 1994). doi:10.1201/9780429246593.

1035

1036

1037 # Methods

1038 Animals

1039 All experiments were carried out in accordance with the Institutional Animal Care and
1040 Use Committee of the University of Geneva and with permission of the Geneva
1041 cantonal authorities (GE258B). C57BL/6J wild-type mice and transgenic mouse lines
1042 were housed 2–6 mice per cage under a 12/12-h non-inverted light/dark cycle with ad
1043 libitum access to food and water. Transgenic mice used for calcium imaging were
1044 obtained as a crossing between Ai148-D mice (Jackson Laboratories, stock number
1045 030328) and Rasgrf2-2A-dCre mice (Jackson Laboratories, stock number 022864).
1046 Ai148-D mouse line is a Cre-dependent reporter line containing a gene encoding the
1047 calcium indicator GCaMP6f at the Igs7 locus. Exposure to Cre recombinase through
1048 viral vector injections or crossing with Cre-expressing mice resulted in expression of
1049 GCaMP6f. Rasgrf2-2A-dCre mouse line expressed a trimethoprim-inducible Cre
1050 recombinase directed by endogenous Rasgrf2 promoter/enhancer elements. When
1051 induced, Cre recombinase activity is observed in cortical layers 2/3 and other scattered
1052 cells of the cortex, hypothalamus, thalamus, and midbrain. Trimethoprim (TMP) i.p.
1053 injections were performed for 5 consecutive days at least two weeks before any
1054 surgical intervention (0.25 mg/g of body weight diluted in DMSO and 0.9% NaCl). As
1055 a result, TMP injected crossed Ai148D x Rasgrf2-2A-dCre mice expressed GCaMP6f
1056 in cortical layer 2/3. For optogenetic experiments, we used Ai32 transgenic mice that
1057 express Channelrhodopsin-2 (ChR2) fused to enhanced Yellow Fluorescent Protein
1058 (eYFP) in a Cre-dependent manner, enabling fast neuronal activation in vivo through
1059 blue light illumination (Jackson Laboratories, stock number 012569). Males and
1060 females aged 2–5 months and weighing approximately 20–25 g were used for all
1061 experiments with no clear sex differences observed.

1062 Viral vectors and markers

1063 For anterograde labeling, AAV2.CAG.GFP (Addgene, #37825-AAV2, titer: 7×10^{12}
1064 vg/mL) and AAV2.CAG.tdTomato (Addgene, #59462-AAV2, titer: 4×10^{12} vg/mL) were
1065 used. The volume of viral vectors injected was around 50-75nL in each site at a depth
1066 of approximately 400-500 μm from the surface of the cortex. Brains were collected 3
1067 weeks after the injections. For retrograde labeling, Cholera Toxin subunit B conjugated
1068 to Alexa Fluor 555 (Invitrogen, reference number C22843) or Alexa Fluor 647
1069 (Invitrogen, reference number C34778) diluted in PBS were injected (~50nL in each
1070 site, 400-500 μm below the surface). Brains were collected 10 days after the injections.
1071 For silencing experiments, AAV-DJ.CMV.eGFP-2A-TeNT viral vectors were injected
1072 in the region of interest (Wu Tsai Neurosciences Institute, reference number GVVC-
1073 AAV-70) at 3 different depths along the cortical column (800 μm, 500 μm and 200 μm
1074 respectively). Behavioral protocols started at least one month after the injections were
1075 done. For optogenetic experiments, Ai32 mice expressing Cre-dependent ChR2-eYFP
1076 were injected with AAV1.CamKII0.4.Cre.SV40 (Addgene, #105558-AAV1,
1077 titer: 3.5×10^{12} vg/mL) in three different locations along RL and two different depths
1078 (250 μm and 500 μm) to express ChR2-eYFP in most of this area.

1079

1080 Stereotaxic surgeries

1081 Pain management was first performed by administrating the opioid Buprenorphine
1082 subcutaneously (0.1 mg/kg) before starting the surgery. Mice were anesthetized inside
1083 an induction chamber with 3% isoflurane mixed with oxygen and then fixed on the
1084 stereotaxic apparatus (Model 940, Kopf). A custom-made nose-clamp has been
1085 adapted to the apparatus to maintain the position of the animal, allowing head rotation.

1086 Body temperature was constantly monitored through a thermic probe and adjusted to
1087 ~37°C via a heating pad placed below the mouse (DC Temperature Controller, FHC).
1088 Breathing rate was regularly monitored by visual inspection. Ophthalmic gel (Vitamin
1089 A, Bausch Lomb) was applied on both eyes to ensure protection from light and prevent
1090 them from drying out. A local anesthetic was injected under the skin of the head before
1091 the surgical incision (mix Lidocaine/Bupivacaine, 6mg/kg and 2.5 mg/kg respectively).
1092 During the surgery, mice were anesthetized with a constant isoflurane level lowered
1093 around 2%. At the end of the surgery, an anti-inflammatory was also administered
1094 subcutaneously (Carprofen, 7.5mg/kg) and animals were warmed with a heating lamp
1095 for at least 15 minutes until recovery from anesthesia. A second anti-inflammatory
1096 (Ibuprofen, Algifor) was added to drinking water for 3-days post-op and the weight was
1097 checked daily to ensure that weight was kept above 15% of the original weight prior to
1098 the surgery. All animals were implanted with a cranial implant. After removing the skin
1099 and tissues on top of the head, the skull was cleaned, dried and thinned. The mouse
1100 head was tilted approximately at a 30° angle, ensuring better access to the left
1101 hemisphere. A custom-made metallic implant was placed on the top of the skull using
1102 a custom-made holder. It was then fixed with a layer of glue (Loctite 401, Henkel) and
1103 additional layers of dental acrylic (Pala, Kulzer) to ensure the implant is securely
1104 attached. Dental acrylic was covered with black nail polish to prevent light
1105 contamination from visual stimuli during imaging experiments. After at least 3 days of
1106 recovery, mice could undergo additional procedures. Animals that underwent imaging
1107 sessions were implanted with a glass window composed of a top round cover slip of 7
1108 mm diameter and two superimposed 5 mm diameter cover slips (CS-7R and CS-5R,
1109 Multi Channel Systems). The three concentric cover slips were glued together with UV
1110 glue (Optical Adhesive n°68, Norland). The craniotomy was the size of the smaller
1111 window and was drilled above the posterior part of the dorsal cortex. Before removing

1112 skullcap, we used a custom-made perfusion chamber with saline solution (NaCl 0.9%)
1113 to rinse the craniotomy continuously and reduce bleeding stains. A custom-made
1114 holder with air-suction was used to hold and position the window. The cranial window
1115 was gently brought down until it was in contact with the brain. The window was then
1116 fixed with UV glue, super glue and dental acrylic. For stereotaxic injections, glass
1117 pipettes (5-000-2005, Drummond) were pulled (Model P-97, Sutter Instrument Co) and
1118 broken to obtain a tip of ~10-15µm inner diameter. Pipettes were further beveled to
1119 create a sharp tip to avoid cortical damage during insertion. Injection sites were
1120 determined using functional mapping. Injections were done using a single-axis oil
1121 hydraulic micromanipulator (R.MO-10, Narishige). The pipette was slowly inserted
1122 inside the cortex until reaching the desired depth. Viral vectors or other reagents were
1123 injected at a speed of ~2nL/s. When the whole volume was injected, we waited 5
1124 minutes with the pipette in the same position before gently removing it.

1125

1126 Behavioral training

1127 A Matlab custom-made graphical user interface (GUI) was developed from the Matlab
1128 App Designer to control the behavioral tasks and monitor performance. The GUI
1129 allowed real time visualization of the animal's performance and online modification of
1130 the parameters (e.g. stimuli parameters, punishment duration, stimuli proportion).
1131 Animals underwent water restriction 2 to 4 days before the training started and were
1132 handled every day by the experimenter for at least 10 minutes. During the pre-training
1133 phase, mice were habituated to head-fixation and placed on the setup. In the first
1134 session, only Go stimuli (i.e., stimuli for which licking responses are rewarded) were
1135 presented and rewards were delivered automatically regardless of mouse actions. Go
1136 trials proportion was progressively reduced as No go trials (i.e., trials featuring the

1137 stimulus for which licking responses were punished) were added in the following
1138 sessions and mice were required to lick to obtain rewards during Go trials. Mice were
1139 trained once a day, every day at the same hour. Eight different behavioral tasks (two
1140 tactile tasks, two visual tasks, two auditory tasks and two optogenetic tasks) were used
1141 for our experiments (Fig. 1, Fig. 2, Extended Data Fig. 1, Fig. 7 and Fig. 7), all following
1142 a Go/No go discrimination paradigm. In the tactile tasks, two whiskers ("top" whisker
1143 B2 and "bottom" whisker C2) were inserted inside glass capillaries each attached to a
1144 piezo actuator that could create a small deflection of about 1 mm along the rostro-
1145 caudal axis. These deflections were sinusoidal pulses and lasted 0.2 s. In one version
1146 of the task, B2 whisker stimulations were associated to a reward (Go trials). In the
1147 other version, C2 whisker stimulations were the Go trials. In the visual tasks, two
1148 drifting squares (a "top" square and a "bottom" square, relative to the midline in the
1149 mouse visual field) were presented on the screen. In one version of the task, top
1150 square stimulations were the Go trials while in the other version of the task, bottom
1151 squares stimulations were the Go trials. The auditory task followed the same structure
1152 as the other tasks but using two short pure tones of 6 kHz and 12 kHz as Go and No
1153 go stimuli, respectively. These tones were delivered from a speaker located next to
1154 the mouse on the same side as the visual and tactile stimuli. The optogenetic tasks
1155 were performed by directly stimulating subregions of RL or AL corresponding to top or
1156 bottom multimodal representation found with calcium imaging, using shaped blue light
1157 patterns. In one version of the task, stimulating the top region was associated with a
1158 reward, while in the other version, it was the bottom region. The total trial duration of
1159 a single trial was 4 s: after a 2 s quiet window (during which licking resulted in trial
1160 abortion) the stimulus was presented, and the mouse was allowed to lick during a 2 s
1161 response window. During Go trials, the mouse could obtain a water reward upon
1162 licking the spout following the stimulus (Hit trials). Failure to lick would result in a Miss

1163 trial. During No go trials, the mouse had to refrain from licking (Correct rejection trials,
1164 CR) or it was punished with a time-out of 10 s (False Alarm trials, FA). Some trials
1165 were presented without any stimulus (catch trials). If the mouse licked during catch
1166 trials, no time-out was applied. If mice were too compulsive (i.e. licking during the quiet
1167 window was too frequent), a 10 s time-out early lick punishment could also be applied.
1168 The proportion of each trial type was the following: Go trials = 30%, No go trials = 50%,
1169 Catch trials = 20%. All tactile stimuli were generated through Matlab data acquisition
1170 toolbox controlling a piezo actuator (Bimorph bendor piezo actuator PB4NB2S,
1171 Thorlabs) through a National Instrument card. All visual stimuli were generated using
1172 Matlab and PsychToolBox. Stimuli were presented on a gray background through a
1173 LCD monitor (20x15cm, pixels, 60Hz refresh rate, Pi-shop) positioned 10 cm from the
1174 eye, with a 30° angle to the right of the midline. The screen was also tilted with a 30°
1175 angle along the horizontal plane to match the mouse head angle with the intent of
1176 roughly aligning the bottom and top parts of the screen to the resting position of the
1177 C2 and B2 whiskers in the mouse visual field. Stimulations during behavior consisted
1178 of black squares moving through the screen in the rostro-caudal direction (bar width
1179 was 12.5°, stimulus duration was 175ms, speed was 500°/sec), on a gray background.

1180

1181 Wide-field microscopy

1182 We used a custom-made wide-field epifluorescence microscope setup[44] including a
1183 sCMOS camera (ORCA-Flash4.0 V3, Hamamatsu). Magnification was achieved
1184 through a 0.63X C-mount camera adapter for Olympus Microscopes. The field-of-view
1185 size was 5.6 mm x 5.6 mm. The camera and adapters were mounted on a base
1186 allowing vertical movement with manual focus. LED white illumination (740mW,
1187 1225mA, Thorlabs) could be controlled via a T-Cube LED driver (LEDD1B, Thorlabs).

1188 Filter cubes could be changed for different types of imaging. For imaging GCaMP6f,
1189 GFP excitation, emission and dichroic filters were used. For intrinsic optical signals
1190 imaging, Cy3/5 excitation, emission and dichroic filters were used. An objective (MVX
1191 Plan Apochromat with 2x, Olympus) was attached to the microscope base. The
1192 somatotopic mapping protocol consisted of repetitive rostro-caudal pulsatile
1193 deflections (~1 mm amplitude) of either B2 or C2 whiskers for 50-80 trials each
1194 followed by a quiet window. The retinotopic mapping protocol consisted of drifting bars.
1195 A contrast reversing checkerboard was presented within the bar to better drive neural
1196 activity (0.04 cycles/° of spatial frequency and 2 Hz of temporal frequency). In each
1197 trial the bar was swept in the four cardinal directions: left to right, right to left, bottom
1198 to top, and top to bottom. Single trials were repeated 20 to 40 times. For anatomical
1199 experiments, only C57BL/6J mice were used. To image the intrinsic optical signal, we
1200 used longer tactile stimulations and slower visual stimulations. Mice were fixed on the
1201 platform and anesthetized during the procedure with isoflurane level lowered than 1%.
1202 Body temperature was monitored with a probe and adjusted to 37°C using a heating
1203 pad (DC Temperature Controller, FHC). For all the other experiments, we used Ai148-
1204 D x Rasgrf2-2A-dCre mice and calcium imaging. The visuo-tactile sparse noise
1205 protocol consisted in combinations of visuo-tactile stimuli: three whisker conditions (C2
1206 whisker stimulation, B2 whisker stimulation and no whisker stimulation) and nine
1207 vertical positions of a moving square similar to the one used for the visual task. The
1208 ninth position corresponded to a no visual stimulus condition (i.e. blank screen).
1209 Together, all visual stimuli spanned approximately 8x12.5°=100° in the vertical space.
1210 Visual and tactile stimuli were either presented alone (unisensory conditions) or
1211 together (multisensory conditions). When presented together, onsets were either
1212 synchronous or delayed (0.15 s delay, visual leading tactile stimulus). In total,
1213 3x9x2=54 different combinations were presented in pseudo-random order with a 1 s

1214 inter-stimulus interval. The full sequence was repeated 60 times. Total sparse noise
1215 protocol duration was approximately 1 hour. At the beginning of each recording, we
1216 took a picture of the cranial window with blood vessels pattern on focus as reference
1217 image. The focus was then set at ~300µm below the surface to maximize signal
1218 collection. Light was adjusted to prevent saturation. Before each imaging session, the
1219 window was cleaned with 70% ethanol and eyes hydrated with mineral oil.

1220

1221 Two-photon microscopy

1222 The two-photon microscope was custom-made (INSS Company). It consisted of a
1223 femtosecond laser with wavelength range 690-1040nm (Tunable Ti:Sapphire with
1224 dispersion compensation MaiTai DeepSee, Spectra Physics) whose beam was
1225 directed with Resonant/Galvo scan mirrors and the emitted signals were detected by
1226 2 GaAsP amplified PMTs (PMT2101/M, Thorlabs). Imaging was performed through a
1227 16x Nikon 0.80 NA objective and using ScanImage (Vidrio Technologies). Images
1228 were acquired at approximately 30 frames per second. Two-photon calcium imaging
1229 during the visuo-tactile sparse noise protocol described in the wide-field section was
1230 performed on Ai148-D x Rasgrf2-2A-dCre mice. After cleaning the cranial window with
1231 70% ethanol, a hydrophobic chamber was made between the head plate and the
1232 imaging platform using liquid plastic (Smooth-Cast 325, Smooth-On) and the objective
1233 was immersed in distilled water. We ensured no polluting light could reach the
1234 objective by covering it with a dark protective sleeve and by turning off the light in the
1235 room. At the beginning of each recording, an anatomical picture of the field-of-view
1236 was taken using a CCD camera. When switching the microscope in two-photon mode,
1237 we took an image of the surface blood vessels at magnification x1 and x1.5 for further
1238 realignment. For each location, we typically imaged at three different depths between

1239 100 µm and 300 µm below the surface. Each mouse underwent no more than two
1240 imaging protocols per day.

1241

1242 Histology

1243 Mice were anesthetized with 3% isoflurane and euthanized with i.p. injection of
1244 Pentobarbital (Eskornarkon, 150 mg/kg) and Buprenorphine (0.1 mg/kg). They were
1245 then transcardiacally perfused using a peristaltic pump (ISM829, Cole-Parmer) with
1246 0.01 M PBS, pH 7.4 for 2 min, and then 4% paraformaldehyde (PFA) in phosphate
1247 buffer (PB; pH 7.4) for 3 min. The brains were post-fixed at 4°C in PFA for 48 h and
1248 then transferred into PBS. For anatomical experiments of Fig. 4, the brains were post-
1249 fixed at 4°C in PFA for 2 h and washed 3 times for 15 min in PBS. The left cerebral
1250 hemisphere was separated from the right hemisphere and subcortical parts were
1251 removed with a spatula. The left hemisphere was flattened between glass slides and
1252 kept flattened at 4°C in PFA for 12 h. After PBS washing, flattened hemispheres were
1253 embedded in agar gel 4% before cutting slices of 70µm thickness with a vibratome
1254 (VT 1000 S, Leica).

1255

1256 Immunohistochemistry

1257 Flat brain sections were incubated with slight agitation (40 rotations/min) for 2 h at
1258 room temperature in a saturation/permeabilization solution containing a mix of 5%
1259 BSA and NGS, 0.3% triton X-100 and PBS. Brain sections were then incubated with
1260 slight agitation (40 rotations/min) overnight at 4°C with a rat anti-muscarinic
1261 acetylcholine receptor M2 (M2 AChR) primary antibody (1:500, Sigma-Aldrich,

1262 reference number MAB367) in the same blocking solution. Sections were washed 3
1263 times for 15 min in PBS before a 2 h incubation with either a donkey anti-rat secondary
1264 antibody conjugated with Alexa Fluor 488 (dilution 1:500, Invitrogen, #A21208) or with
1265 a goat anti-rat secondary antibody conjugated with Cy5 (dilution 1:500, Invitrogen,
1266 #A10525) in blocking solution at room temperature without agitation. Hoechst solution
1267 (dilution 1:1000, Invitrogen, # 33342) was used for fluorescent nuclear counterstaining.
1268 Slices were incubated for 10 min in that solution with slight agitation then washed 2
1269 times for 5 min in PBS.

1270

1271 Histological imaging

1272 Slices were mounted on Superfrost microscope slides (Epredia) with mounting
1273 medium (Fluoromount) and covered with 24x50 mm coverslips (Menzel-Gläser). All
1274 photomicrographs were taken using a Zeiss Axio Scan.Z1 or a Leica Stellaris 5
1275 microscope at the bioimaging platform of the University of Geneva.

1276

1277 Wide-field calcium imaging analysis: Retinotopic and whisker mapping protocols

1278 Responses to drifting checkerboard stimuli were averaged across trials for each
1279 condition and converted in df/f using a pre-stimulus time window as baseline. Azimuth
1280 and elevation preference maps were then computed[24].To segment visual areas,
1281 azimuth and elevation maps were combined to generate a visual field sign map. The
1282 sign map was computed as the sine of the difference between the vertical and
1283 horizontal retinotopic gradients for each pixel. Somatotopic maps were obtained by

averaging the response df/f across B2 or C2 stimulation trials over a short time window of 200 ms.

Wide-field calcium imaging analysis: Sparse noise protocol

After an initial down sampling to a resolution of 100 x 100 pixels by bicubic interpolation, 50 Hz framerate videos acquired during the sparse noise protocol underwent pixelwise notch filtering (f_0=12 Hz, f_w=6 Hz) and discrete wavelet transform (DWT) detrending (setting lowest frequency approximation coefficients to zero in a 6-level decomposition) to remove artifacts and low-frequency drifts. After these initial preprocessing steps, videos were z-scored using as reference distribution the ensemble of all pixel values corresponding to blank stimuli (i.e. trials with no visual and no tactile stimulation). Next, trials with a high baseline activity (>=0.5 z-score on average, corresponding to a strong positive fluctuation of spontaneous activity preceding the stimulus) were discarded and z-score and baseline subtraction were computed again including only remaining trials. This was meant to better separate local responses to sensory stimulations from ongoing spontaneous activity. Starting from the z-scored data obtained in this way, response surprises (i.e. $-\log10(p_{t\text{-}test})$) across trials were computed for each time point and each stimulus to define spatial responsivity masks. Average visual or tactile top or bottom response movies were obtained by averaging the median responses across trials to the relevant stimuli. For visual “top” all stimulation conditions (either unimodal or multimodal) in which the visual stimulus was present in grid positions 7 or 8 were used whereas for visual “bottom” all visual conditions including positions 3 or 4 were used. Retinotopic and somatotopic maps of vertical space (Fig. 3b,c and Extended Data Fig. 6g) were obtained by taking the difference between average visual or tactile top and bottom

response maps. Modality preference maps (Fig. 3d and Extended Data Fig. 6g) were obtained by computing pixel-by-pixel the difference between the maximum response for visual and tactile stimuli. Multisensory enhancement maps (Fig. 3f and Extended Data Fig. 6g) were obtained by computing pixel-by-pixel the difference between the maximum unisensory response between visual and tactile stimuli (predicted response) and the multisensory response (measured responses). For all the difference maps mentioned above the input maps were independently normalized to the [0,1] interval before taking the difference (ensuring their range to be bound in the [-1,1] interval). Retinotopy-somatotopy spatial coherence maps (Fig. 3e and Extended Data Fig. 6g) were obtained by convolutionally (stride = 1 patch size = 8 pixels) computing the correlation-based similarity of matching patches of the two different maps. The result was then scaled by the average peak-to-peak range in that patch (to diminish contribution from pixel with very low response magnitude). Comparison of grand average maps at single pixel level (Fig. 3g,h) was performed on responsive pixels only (exceeding a surprise threshold corresponding to $p_{t\text{-}test} <= 0.1$ for either visual or tactile responses). We compared pixels with low and high modality preference (i.e. below or above 85% quantile of the absolute value distribution within the responsive region) or with low and high coherence (i.e. below or above 15% quantile of the absolute value distribution within the responsive region). Grand average maps displayed in Fig. 3b,c,f are obtained by averaging frames of the corresponding grand-average movie (obtained by realigning single mouse movies to the common reference atlas and then averaging) over different time windows: frames 18 to 20 for the somatotopy (i.e. 0.16 s to 0.20 s after stimulus onset); frames 25 to 27 for the retinotopy (i.e. 0.30 s to 0.34 s after stimulus onset); and frames 28 to 30 for multisensory modulation (i.e. 0.36 s to 0.4 s after stimulus onset). These windows were chosen to be roughly centered on the peak of these signals. Grand average modality preference and spatial coherence

maps displayed in Fig. 3d,e were computed on maps obtained above (average z-score maps or position selectivity maps, respectively). Signal time courses displayed in Extended Data Fig. 7 were obtained by integrating grand-average movies across time-varying regions of interest (ROIs). These ROIs were specifically defined to track the activity 'bump' evoked by stimulation in each area. To prevent bias in estimating the response —particularly in areas with higher cortical magnification factors, which could lower the average by including many non-responsive pixels— these masks were created by intersecting a static mask, which selects each area based on the fitted reference atlas, with a dynamic responsivity mask. This dynamic mask selects, for each movie frame, only those pixels that across mice show an average maximum response surprise, exceeding a threshold (corresponding to a p-value ≤ 0.01 across conditions). To measure angular mismatch between retinotopic and somatotopic maps we computed vertical retinotopy gradient vectors from the grand-average version of these maps (using Matlab “gradient” function with a scale of 4 pixels followed by a Gaussian smoothing of gradient components). Then a region of interest overlapping with RL was defined and we computed the average angular difference between the two gradient fields.

<u>Atlas fitting and registration</u>

The reference Allen Mouse Brain atlas[67] was first tilted sideways at 30° and then projected to match the skull tilt in our experiments and therefore the layout of areas in the dorsal cortex. The resulting atlas was manually fitted to the wide-field imaging field-of-view for each mouse by visually aligning the atlas boundary lines to reproducible landmarks from functional maps. Both the maps obtained from the sparse noise protocol (i.e. vertical retinotopy and somatotopy difference maps) and the maps

1360 obtained from the whisker and retinotopic mapping protocols were used to register the
1361 atlas. Landmarks used include the outlines of the sign map regions, the position of C2
1362 and B2 whisker activity bumps in S1 and S2, the reversal of vertical retinotopy at the
1363 boundary of each visual area (see Extended Data Fig. 6 for example). To relate
1364 microscale and macroscale functional properties measured respectively by two-
1365 photon and wide-field imaging experiments, we also manually reconstructed the
1366 position of each two-photon field-of-view (FOV) in the frame of reference with the atlas
1367 fitted to the wide-field maps. To do so, we aligned the blood vessels pattern visible in
1368 each two-photon FOV with the one visible in the wide-field cortical image (as shown
1369 in Extended Data Fig. 9f). To compare data across mice and compute grand averages,
1370 we developed a Matlab pipeline to robustly realign atlases to one another. This
1371 pipeline was based on iterative application of the image registration algorithm
1372 implemented by Matlab function "imregtform" (considering "rigid" transformations in
1373 "monomodal" mode) to stack images depicting atlas boundaries. This pipeline enabled
1374 us to obtain the rotation and shift required to register all maps and neuron positions to
1375 the frame of reference of a common atlas. For the anatomical tracing experiments (Fig.
1376 4b-d), a similar processing was performed with ImageJ through registration of atlases
1377 fitted using the M2 AChR staining. Brain from all mice with similar injections could then
1378 be averaged together. To compare the somatotopy and retinotopy of axonal
1379 projections or projecting neurons with the functional topographic maps obtained in
1380 wide-field we brought them in a common reference frame by registering a crop of the
1381 M2 AChR-fitted atlas to the common wide-field/two-photon atlas (by finding the
1382 registering affine transformation with Matlab functions "cpselect" and "fitgeotrans").

1383

1384 <u>Two-photon calcium imaging analysis: Pre-processing and functional cell-types</u>

To extract time-varying somatic GCaMP6f calcium signals, we used the Suite2p toolbox[68]. Neuropil contamination was corrected by subtracting the fluorescent signal from a surrounding ring $F_{Surround}(t)$ from somatic fluorescence: $F(t) = F_{Soma}(t) - \alpha * F_{Surround}(t)$ with $\alpha=0.7$. Neuropil-corrected fluorescence signals F(t) were then converted in z-score by subtracting from each trace the mean value and dividing by the standard deviation of F(t) over the last 0.2 s of the baseline window preceding the stimulus onset (pooling across all trials). Using these z-scored fluorescence traces we computed response surprises (i.e. $-\log10(p_{z\text{-}test})$) across trials for each stimulus and for each time sample. Similarly, we computed the coefficient of variation (CV) across trials quantifying response variability. A neuron was considered reliably responsive if its response exceeded a stringent surprise threshold $Surprise_{th} = 8$ (i.e. $p_{z\text{-}test} <= 10^{-8}$) while remaining below a coefficient of variation threshold value $CV_{th} = 4$ for at least 4 consecutive time bins in any stimulus condition. This responsivity criterion was requested for each neuron to be included in subsequent analyses. For each neuron included, we used a more inclusive criteria to characterize the extent of their tuning properties. Indeed, neurons exceeding a less stringent threshold $Surprise_{th} = 2$ (i.e. $p_{t\text{-}test} <= 0.01$) while remaining below the same coefficient of variation threshold at any time bin of a visual, tactile or visuo-tactile condition were considered “responsive” to these conditions. The responsivity pattern of each neuron was used to classify them in one of four functional classes: 1) neurons responsive in visual but not tactile conditions were termed “visual neuron”; 2) neurons responsive in tactile but not visual conditions were termed “tactile neuron”; 3) neurons responsive in both tactile and visual conditions were termed “visuo-tactile neuron”; 4) neurons responsive only in visuo-tactile conditions (both visual and tactile stimuli presented together) were termed “gated neuron”. Only visuo-tactile neurons displaying significant responses in both modalities were used for the analyses displayed in Fig. 5g-j. Measured multisensory

1411 responses were compared to a “max model” of multisensory interaction[69] (as in Fig.
1412 5b and Extended Data Fig. 11b). Predicted visuo-tactile z-scored traces for each
1413 multisensory stimulus condition were computed trial-wise by taking the max (for each
1414 time bin) between the response to the same visual and tactile stimulus presented
1415 alone (i.e. the corresponding unimodal conditions) and subsequently averaging across
1416 trials. Average responses (predicted or measured) were computed over a response
1417 window spanning from 0.2 s to ~0.733 s following stimulus onset for each stimulus
1418 and each responsive neuron.

1419

1420 Two-photon calcium imaging analysis: Computation of indices

1421 We computed the “multisensory modulation index” (MI) as the normalized difference
1422 between predicted and measured visuo-tactile responses at every time bin for every
1423 stimulus condition. To summarize the intensity of multisensory modulation of each
1424 neuron across stimulus conditions over time we computed the min-max range of the
1425 integral of MI values over the same time window mentioned above (i.e. from 0.2 s to
1426 0.733 s) across all valid conditions. Valid stimulus conditions comprised significant
1427 responses as well as all multisensory conditions containing at least one unisensory
1428 stimulus to which the neuron is responsive and displaying significant multisensory
1429 modulations (i.e. with $p<0.05$ of a bootstrap-t test for MI value for at least one time bin,
1430 see “quantification and statistical analysis” section below). Preferred vertical position
1431 in the tactile or visual space of each neuron was quantified as the center-of-mass of
1432 these average responses along the corresponding dimension of the stimulus grid on
1433 visuo-tactile (measured or predicted) conditions. This center-of-mass was converted
1434 into a “position preference index” ranging from +1 for neurons tuned to the top
1435 visual/B2 whisker stimulus to -1 for neurons tuned to the bottom visual/C2 whisker

stimulus. This index characterizes the tendency of each neuron to respond more to stimuli located at one particular end (i.e. “top” or “bottom”) of the spectrum of stimulus positions presented in each modality (as in Fig. 5c,d,g and Extended Data Fig. 10a-b). The sharpness of positional tuning of neurons was computed as the inverse of the best sigma parameter of a Gaussian fit of the average response to each visual position or as the absolute value of the tactile position selectivity index described above. This selectivity index was computed on the visuo-tactile condition of max response (both in the measured or predicted case). These indices ranged from 0 for neurons responding equally to all positions (i.e. completely positionally untuned) to 1 for neurons responding to only one position (i.e. maximally positionally tuned). The values of positional preference and selectivity indices shown in Fig. 5g,h,i,j are averaged over both delay conditions (i.e. with or without delay between tactile and visual stimuli, see Extended Data Fig. 7). Neurons were labeled as ventral or dorsal by running a k-means clustering algorithm (with $n_{centroids}$=2) on the spatial distribution of visuo-tactile neurons over the surface of the dorsal cortex (Fig. 5e).

<u>Two-photon calcium imaging analysis: Correspondence with wide-field</u>

To quantify the correspondence between single-neuron properties distributed across the cortex and the wide-field maps, we created smoothed spatial maps from 2D histograms that depict the dominant response properties at each cortical location. We generated retinotopic and somatotopic maps from two-photon data (Fig. 5c,d and Extended Data Fig. 10a,b) by smoothing a 2D normalized histogram of neurons with positional preferences (top-preference index≥0.05, bottom-preference index≤0.05) using a Gaussian kernel (σ~3% of total wide-field FOV) and then calculated the difference between these maps. For modality preference maps reconstructed using

1461 two-photon data (Extended Data Fig. 10c), we applied a Gaussian smoothing (σ~3%
1462 of FOV) to 2D normalized histograms that describe the distribution of unimodal visual
1463 and tactile neurons, calculating the normalized difference between them. To map
1464 multisensory modulation (Extended Data Fig. 10d), we applied Gaussian smoothing
1465 (σ~3% of FOV) to a MI-range-weighted histogram showing the spatial distribution of
1466 multisensory modulations, then normalized this against the unweighted distribution
1467 that includes unresponsive neurons. We included unresponsive neurons to properly
1468 capture the relative density of multisensory modulation in the local population. To
1469 quantitatively assess the match between two-photon reconstructed maps and the
1470 wide-field maps, we computed a Pearson correlation coefficient restricted to the pixels
1471 with good two-photon coverage (thresholding the map shown in Extended Data Fig.
1472 9g at a threshold of 2,000 neurons/mm2).

1473

1474 Two-photon calcium imaging analysis: Decoding analysis

1475 To test whether the neuronal representation observed across the dorsal cortex of
1476 naïve mice could support cross-modal generalization observed in our behavioral
1477 experiments, we adopted a decoding approach. We trained a Bayesian classifier to
1478 infer stimulus category (top or bottom) from single-neuron responses in the tactile
1479 modality and then tested the accuracy on the visual modality. This decoder was
1480 inspired by original works introducing neuronal population probabilistic codes[70,71] and
1481 is similar to the approach used in previous work[20]. We built feature vectors
1482 representing the response of each neuron to each stimulus category (i.e. “top” and
1483 “bottom”) in each modality. The feature vectors were defined, for each neuron, as the
1484 z-score response integrated over a 0.2 s - 0.733 s time window in every trial of the
1485 most responsive stimulus position pertaining to each category (visual top = positions

5 to 8, visual bottom = positions 1 to 4, tactile top = B2, tactile bottom = C2). The response feature vectors were used in a trial-wise fashion as predictors to infer the "top" or "bottom" labels corresponding to the location of the stimulus delivered to the animal. We incorporated 4-fold cross-validation to mitigate overfitting and assess the classifier's accuracy outside the training dataset. Trials were partitioned into four batches, three of them for training and one for testing. The decoding was assessed both at the single neuron level (n_{pool} = 1 and averaged over all neurons of a given class to get the values displayed in Extended Data Fig. 11d,e) as well as on pools of neurons of increasing size (n_{pool} = [1,50] to get the curves displayed in Extended Data Fig. 11c). During population decoding, we repeated the procedure 40 times, each time randomly resampling the neurons in the decoding pool without replacement to ensure that the results were not dependent on a specific selection and partitioning of neurons. Decoding accuracy (defined as the fraction of trials with correct predictions) was averaged across resampled data and cross-validation splits. Prior to classification, each neuron's response features within the population vector were individually normalized to a 0-1 range across trials. Additionally, trials were randomly reordered, maintaining their corresponding correct labels, to eliminate noise-related correlations. In this probabilistic framework the ''training" consists simply in computing the average tuning curves (i.e. stimulus-triggered average) using all trials included in the training set and taking the logarithm of this vector. The subsequent ''testing'' of the decoder requires to generate a prediction. Predictions were made by calculating each test trial's feature vector log-likelihood for the 'top' or 'bottom' stimulus, then assigning the label with the highest log-likelihood as the predicted outcome. The log-likelihood can be obtained by taking a matrix product between the matrix storing the log of tuning curves computed at the ''training'' stage and the current population feature vector (after subtracting a corrective term proportional to the sum of all tuning curves to account for

any representational bias in the decoded population). Tactile decoding performances represented in Extended Data Fig. 11c,d,e corresponded to the average cross-validated test accuracies on the same modality on which the Bayesian classifier was trained (i.e. tactile).

Behavioral analysis

To quantify mouse behavior over time within single sessions we isolated different stimulation conditions (i.e. trials with top stimuli, trials with bottom stimuli and Catch trials) to compute a smoothed conditional lick probability over a sliding window of 60 trials. We calculated the conditional probabilities of licking by dividing the number of trials with a mouse lick response to a specific stimulus by the total presentations of that stimulus within the moving time window. These curves are the ones displayed throughout the paper (Fig. 1,2,6,7 and Extended Data Fig. 1,3,4,12,13) and labelled "Top", "Bottom" and "Spont". From Go and No go lick probabilities (defined by the task rule to coincide with top or bottom), we also computed a "Discrimination performance" metric as the percentage of correct trials for discrimination. Specifically, we defined behavioral performance as the average between the rate of correct choices upon delivery of the Go stimulus (i.e. Hit rate = conditional lick probability for Go trials) and the rate of correct rejects upon delivery of the No go stimulus (i.e. Correct Reject rate = 1 — False Alarm rate where False Alarm rate = conditional lick probability for No go trials). This way of computing the performance makes it insensitive to the proportion of Go and No go trials. Following a similar logic, we defined a "Detection performance" as the maximum between the Go detection rate (i.e. average Hit rate and Catch Correct Reject rate) and the No go detection rate (i.e. average False Alarm rate and Catch Correct Reject rate). Behavioral states were classified as previously

1537 described[20].The end of each session was determined as the trial following peak
1538 performance where the conditional lick probability for Go trials dropped below 66% of
1539 its maximum value. Conditional lick probabilities and performance per session were
1540 computed only during engaged trials of each session (i.e. discarding the part of the
1541 session during which conditional lick probabilities dropped due to task disengagement).
1542 Switch-aligned performance trajectories shown throughout the paper (Fig. 1,2,6,7 and
1543 Extended Data Fig. 1,2,4,13) were obtained realigning the curve of average session
1544 performance and conditional lick probabilities around the session of task switch.
1545 Accompanying bar plots display the difference of discrimination and detection
1546 performance between the last session before the switch and the first session after the
1547 switch. In Extended Data Fig. 3, we plotted the average conditional lick probabilities
1548 and the performance time course across mice that underwent whisker removal control
1549 sessions. These average curves were obtained by dividing each session in three
1550 chunks: “before”, “during” and “after” whisker removal and averaging them separately
1551 after a stretching interpolation to match their duration. Accompanying bar plots display
1552 the average discrimination and detection performance in these three chunks
1553 (excluding boundary timepoints to avoid contamination due to the temporal smoothing
1554 induced by the sliding window we used to compute the traces). Learning rates
1555 following the switch (Fig. 2c and Fig. 6l) were obtained measuring the slope of the best
1556 fitted line for 3 consecutive sessions after switch for all mice in each group. We
1557 excluded mice that did not show a drop of performance to chance level after the switch
1558 as they successfully generalized from one modality to the other. The relationship
1559 between the TeNT-P2A-GFP expression overlap with each cortical area and the
1560 cross-modal generalization performance impairment in rule-preserving conditions was
1561 assessed using Pearson coefficient of correlation. Specifically, for each mouse we
1562 calculated the Pearson coefficient of correlation between two vectors: 1) the vector

representing the fractional overlap of TeNT expression binary masks (displayed in Extended Data Fig. 12) and each atlas-defined cortical area, and 2) the vector representing the change in performance following modality switch (performance averaged over 3 consecutive sessions after switch). This analysis was performed for each cortical area (examples for areas RL and AL are shown in Extended Data Fig. 12f) and displayed as a correlation map in Fig. 6e. For the reverse correlation approach, we computed the difference between the average of all TeNT-injected mice GFP fluorescence binary masks and the one of mice displaying impairment of cross-modal generalization ability (defined as mice performing below 57.5% of correct trials on average in the 3 sessions following a rule-preserving modality switch). This difference took null or negative values in areas where TeNT expression did not affect the behavior and positive values in regions producing behavioral impairment (i.e. regions where TeNT expression is enriched in the impairment-triggered ensemble compared to the ensemble including all TeNT-expressing mice).

Quantification of TeNT expression and ventral/dorsal grouping

Wide-field fluorescence images of dorsal cortex displaying the pattern of expression of TeNT-P2A-GFP in each injected mouse were first pre-processed to remove the blood vessels from the surface. This was necessary to obtain a smooth, non-occluded estimate of the spatial profile of GFP expression across the surface of the cortex. To do so we first segmented the blood vessels with adaptive thresholding (using Matlab function “adaptthresh”) and then inpaint them by local interpolation (using Matlab function “regionfill”) (Fig. 6g,i and Extended Data Fig. 12a-d and 13b). Next, we computed a median-subtracted map of df/f calculated with respect to a manually annotated region of interest on the border of each window (selected to correspond to

1588 a fluorescence profile stable around baseline level, usually at the farthest end of the
1589 window with respect to the injection site). To compare images across different mice
1590 and account for variations in imaging conditions, we normalized saturation by clipping
1591 the values in each map to the minimum peak value observed across all mice. After
1592 normalizing these resaturated df/f maps to 1 we computed their 0.90 contour (i.e. the
1593 expression "patch") to define the binary TeNT-P2A-GFP expression mask to be used
1594 in subsequent analyses to evaluate the spatial extent of toxin expression. The overlay
1595 of these masks for all mice is displayed in Extended Data Fig. 12e. Next, TeNT-
1596 expressing mice undergoing rule-preserving modality switch were subdivided in
1597 "dorsal" and "ventral" subgroups by computing a d-prime measure (distance
1598 normalized by patch size) with respect to the two multimodal visuo-tactile neuron
1599 clusters found by k-means in the two-photon analysis of Fig. 5e. Neurons outside the
1600 region of low d-prime with patch centroid falling respectively within AL/LI or A/RL
1601 region were categorized as ventral and dorsal, respectively (Fig. 6g,i showed the
1602 overlay of the binary masks together with expression centers as dots over the common
1603 atlas). The same procedure was followed to validate the targeting of TeNT injections
1604 to the dorsal region in mice undergoing rule-reversing modality switch (Extended Data
1605 Fig. 13b). To quantify potential differences in the size of TeNT-expressing cortical
1606 patches between the "ventral" and "dorsal" subgroups of animals, while accounting for
1607 the surface obstructed by dental cement at the edge of the cranial window, we
1608 performed a Gaussian fit on the normalized df/f images mentioned above. A 2D
1609 anisotropic Gaussian function was fitted to the fluorescence distribution by non-linear
1610 least squares optimization (using Matlab function "fmincon"). The full-width-at-half-
1611 maximum (FWHM) of the fitted Gaussian was used to define the contour of the
1612 corrected expression area. This approach provided the occlusion-corrected estimation
1613 of the TeNT-P2A-GFP expression surface, reported in Extended Data Fig. 12f.

1614

1615 Anatomical tracing analysis

1616 For each brain, M2 AChR immunostaining and tracer fluorescence images of each
1617 slice were realigned by matching the radial blood vessel pattern. To do so, we applied
1618 the “Normalize local contrast” function in ImageJ and then inverted the image to crop
1619 low intensity pixels and isolate blood vessel holes. We then iteratively registered these
1620 images across the stack in ImageJ using the “MultiStackReg” function with affine
1621 transformation. The transformation could then be applied to the original stack. Slices
1622 with good fluorescence signals were then averaged together. For anterograde tracing
1623 data, we first applied an “Unsharp mask” function (radius: 20, mask weight: 0.8) and
1624 pixel values were log-transformed to enhance axonal projections with respect to the
1625 strong signal at the injection site where cell bodies are labelled. For retrograde tracing
1626 data, a top hat filter (radius: 12) was applied to highlight the signal carried by CTB-
1627 positive cells followed by the “Enhance contrast” function (Saturated pixels: 0.55%).
1628 Realigned average slices for each mouse were then manually fitted to a projection of
1629 the Allen mouse brain atlas using M2 AChR landmarks[67]. Individual mouse atlases
1630 were then registered to common reference atlas. Centroid positions for injection
1631 locations were determined by calculating the center of mass of the fluorescence
1632 signals within manually outlined regions surrounding the injection sites. For
1633 anterograde tracing data, fluorescence images corresponding to different injections
1634 were normalized to the unit range per channel across brains and median-equalized
1635 across channels within brains. For retrograde tracing data, fluorescence images
1636 corresponding to different injections were rescaled to have the same peak value
1637 across channels and brains. Center-of-mass coordinates for each injection in each
1638 brain were projected on a line corresponding to the vertical meridian in the somatotopic

1639 or retinotopic map at the targeted site. This yielded, for each injection, a vertical
1640 coordinate as the center location. Lastly, we obtained an average projection map by
1641 weighting the coordinate of each injection center with its normalized pixel intensity at
1642 every pixel across the stack of fluorescence images (Fig. 4b,c,d and Extended Data
1643 Fig. 8g). The maps obtained in this way represent for every pixel the preferred
1644 projection origin (anterograde) or projection target (retrograde) location along the
1645 vertical line, allowing for an understanding of the topographic mapping of inputs and
1646 outputs associated with various regions. We also established a statistical metric to
1647 assess the significance of projections at each location. This was accomplished by
1648 comparing the median difference between two distributions: the local distribution of
1649 normalized pixel intensities at each location and the distribution of normalized pixel
1650 intensities from a specific frontal-lateral region of the slice. The latter region was
1651 selected based on its lack of fluorescence signal, as determined by an initial visual
1652 examination of the raw images. The center of the color scale used to plot the projection
1653 maps corresponds to the median projection coordinate of the injection ensemble.
1654 Average projection maps were compared to wide-field retinotopic and somatotopic
1655 maps. This was achieved by aligning a selected portion (matching the cranial window
1656 field-of-view) of the projection maps with the shared wide-field/two-photon atlas.
1657 Subsequently, we calculated the Pearson coefficient of correlation between the two
1658 images as a measure of similarity. Pixels exhibiting non-significant projection signal
1659 were discarded for this analysis.

1660

1661 <u>Optogenetic substitution experiments</u>

1662 To test if the dorsal cortical area RL or AL is sufficient for cross-modal generalization,
1663 we used area-specific optogenetic activation as a substitute for visually evoked

1664 responses. We expressed Channelrhodopsin-2 in the cortex by injecting
1665 AAV1.CamKII0.4.Cre.SV40 into the whole RL or AL area of Ai32 mice. This approach
1666 induced a widespread expression of Channelrhodopsin-2 (ChR2) fused with
1667 Enhanced Yellow Fluorescent Protein (eYFP). ChR2, a light-gated cation-selective
1668 channel, generates depolarizing photocurrents in response to blue illumination,
1669 thereby allowing for the excitation of cortical neurons[72]. To illuminate the cortical
1670 surface of head-fixed mice during behavioral tasks, we built a behavioral rig equipped
1671 with a Digital Light Processing (DLP) module (STAR 3.0 EVM Monochrome LED
1672 Projection Modules, DLP6500, ViALUX GmbH). This module features a 1024 × 768
1673 Texas Instruments micro-mirror chip and a 460 nm blue LED, integrated with an
1674 inverted tandem-lens configuration macroscope. The optical tower assembly
1675 comprised two lenses configured in an L-shaped pathway, separated by a dichroic
1676 mirror. Light from the macroscope enters through the projection lens (L1; 150 mm smc
1677 Pentax-A 645 lens) at the rear, reaching a dichroic mirror (640 nm cutoff wavelength;
1678 60 × 60 mm; Semrock) positioned at a 45° angle. This mirror reflects the light towards
1679 the front end of the objective lens (L2; 50 mm Nikon NIKKOR lens), which projects the
1680 image onto the mouse's cortex. Stimulation intensity was adjusted, for each mouse,
1681 to ensure detection while minimizing heat dissipation in the cortex: this was achieved
1682 by operating the stimulation LED within a power range that produced an irradiance
1683 between 3.5mW/mm^2 and 11.5mW/mm^2. The refresh rate was set at 100Hz with a
1684 projected pixel size measuring approximately 6.5 μm. To prevent mice from directly
1685 perceiving the blue light used for optogenetic stimulations, we enclosed the optical
1686 column and the mouse skull with an opaque sleeve. To optogenetically stimulate the
1687 cortex with task relevant information concerning the vertical position of the stimulus,
1688 we shaped the blue light projection in every trial to match the top or bottom encoding
1689 subregions of the RL or AL map. Light patterns were obtained by thresholding the

average retinotopy movies within each area boundaries as defined by the fitted atlas. To effectively drive neuronal activity with blue light, we pulsed illumination at 30 Hz[72]. We used a pulsing pattern over the top or bottom encoding part lasting one second within the response window. Real-time projection control was achieved integrating ALP Vialux API with the custom-made Matlab graphical user interface (GUI) used to run the behavioral tasks and monitor mouse performance. Analysis of task performance during optogenetic substitution sessions was carried out exactly as described in the "behavioral analysis" section above.

Network model

We constructed four recurrent excitatory (E) / inhibitory (I) rate networks representative of the areas V1, S1, AL, and RL (Fig. 8a). We abstracted the decision process to a pair of readout units which in turn drove an integrator through a drift-diffusion process. Recurrent rates of the units in each region evolved according to

$$\tau_i \dot{r}_i = -r_i + \mathrm{f}\left(W_{ij} r_j + I(t) + \sigma_r \mathrm{x}_i(t)\right)$$

where W_{ij} are the connection weights from unit j to unit i, $I(t)$ is a source of external input to V1 and S1 cells only, and x_i is noise independent to each unit, evolving according to $\mathrm{dx_i} = -\mathrm{x_i dt} + \sigma_x \mathrm{dW}$ where dW is a Wiener process with scaling factor σ_x. For I cells $\sigma_r = 0$. We used a saturating transfer function, given by:

$$\mathrm{f(x)} = \beta \left\lfloor \frac{1}{1 + \exp(-(\mathrm{x} - \mathrm{x_0})/\rho)} - \frac{1}{1 + \exp(\mathrm{x_0}/\rho)} \right\rfloor_+ .$$

where $\lfloor \cdot \rfloor_+$ denotes a threshold at zero. Each region was divided into two subnetworks (corresponding to top- and bottom-preferring cells) of N_E excitatory neurons and $N_I =$

N_E inhibitory neurons each. These subnetworks were anatomically segregated such that weights were partitioned into top- and bottom-preferring units which did not interact (i.e. $W_{ij} = 0$ for *i* top and *j* bottom, or *i* bottom and *j* top; see Fig. 8). Within a subnetwork, neurons were all-to-all connected. Projections between regions respected subnetwork boundaries and were limited to E neurons; feedforward projections contacted both E and I neurons; feedback projections only contacted E neurons. Weights of feedforward projection connections (i.e. V1 or S1 to RL or AL) were scaled up relative to the within-region weights ($3.2W_{EE}$), and feedback projections (i.e. AL or RL to V1 or S1) were scaled down relative to within-region weights (RL: $0.4W_{EE}$; AL: $0.04W_{EE}$). In order to model AL/RL silencing we removed all incoming and outgoing connections to the AL/RL units. AL did not project to the decision units. Simulations were subdivided into multiple trials of length 400 ms, defined as a period of no external stimulation t_{isi} = 200 ms, i.e. $I(t)$ = 0, together with presentation of a stimulus $I(t)$ > 0 to the V1 or S1 network (mimicking the visual or tactile stimuli, respectively) for time t_{stim}= 200 ms which was exclusive to either top- or bottom-preferring units in one of the two sensory regions (V1 or S1). The stimulus was modeled as a step function, i.e. $I(t) = c_s$, where c_s is a constant. The stimulus was randomized for each trial. In order to model rewards in our framework we considered two abstract readout units, z_1 and z_2, corresponding to 'go' and 'no-go' responses, respectively. The activity of these units was a weighted linear sum of activity from E neurons within the recurrent network $\mathrm{z_i(t)} = \alpha W_{ij} r_j$ where α is a scaling constant. The network's decision was determined by producing a decision variable δ_i for each z_i by integrating z_i from stimulus onset in the presence of independent noise,

$$\mathrm{d}\delta_i = z_i \mathrm{dt} + \sigma \mathrm{dW}$$

where dW is a Wiener process with scaling factor σ. Decisions were instantiated once a fixed threshold θ_0 was reached by either z_1 or z_2 resulting in the specific decision encoded by that readout unit; if neither z_1 nor z_2 crossed the threshold before the end of the stimulus period, the action was considered 'no-go'. Once a decision was reached the response z_i was modified according to $\widetilde{z_i}(t) = z_i(t) + c_r$, until the end of the stimulus interval. If the decision was correct relative to the presented stimulus then $c_r > 0$, otherwise $c_r < 0$. $|c_r|$ was defined as the difference between the current z_i and the last value of z_i before the stimulus period. Only projection weights from regions V1, S1, and RL to the output variables z_i were plastic. Weights evolved according to a Hebbian rule:

$$\dot{W_{ij}} = \gamma z_i r_j$$

where $i \in \{1, 2\}$, $j \in \{1, \dots, N_E\}$, and γ is the learning rate. Weights were bounded between 0 and $W_{max} = 1$ and normalized after each update to the initialized mean $\overline{W_z}$ within a region. Weights were initialized as a gaussian centered at mean $\overline{W_z}$ = 0.5 with standard deviation $\sigma_z = 0.1$. All model simulations were run for 100 trials before and after a switch. In order to compare model performance with the animal behavior we recorded the trial outcome for each stimulus presentation. We then computed a performance metric and 'go' probabilities conditioned on the stimulus in a sliding window of width 15 trials. In particular, if we define s_1 as input to the bottom-preferring units and s_2 as input to the top-preferring units, within each window we calculated $P(z_1|s_1)$ and $P(z_1|s_2)$ as the 'go' probabilities. The performance accuracy was computed as P(correct) with correct defined as $z_1 > z_2 \mid s_1$ and $z_2 > z_1 \mid s_2$ in the rule-preserving context and $z_1 > z_2 \mid s_2$ and $z_2 > z_1 \mid s_1$ in the rule-reversing context. We quantified the number of trials to reach criterion across four different trial conditions: rule-preserving and rule-reversing switches in the full model; rule-preserving and rule-

reversing switches with RL silenced. We set a criterion value of 0.75 performance accuracy for each trial condition to quantify the number of trials until the model relearned after a switch. Because the mean performance accuracy increased approximately monotonically while response conditions were held constant, we computed the first time at which a given model run reached the criterion value as the time to (re)learn. If a model run did not reach the criterion within a specified number of trials, we omitted it from this analysis. The parameters used in the model are the following:

Variable	Value
W_{EE}	0.05
W_{EI}	0.065
W_{IE}	0.055
W_{II}	0.045
c_s	20
ρ	15
x_0	20
β	30
α	$1/(6N_E)$
α (lesion)	$1/(2N_E)$
γ	4e-7
σ	0.08
σ_x	$\sqrt{2}$
σ_r	0.75

τ_E	20
τ_I	10
θ_0	80

The code is available at: https://github.com/comp-neural-circuits/Guyoton-Matteucci-etal-2025.

Quantification and statistical analysis

Statistical details of experiments and analysis are described in figure legends and in the main text. Details include statistical tests used, sample type and size as well as definition of bar plots and error bars. In figure legends, standard error of the mean (S.E.M.) is specified when plotted as error bars. Paired or unpaired t-tests were used to assess significance of mean comparisons (implemented by Matlab functions “ttest” and “ttest2”, respectively). Normality tests were not performed systematically but individual data points were plotted to visualize distributions. Wilcoxon signed rank test were used to assess significance in paired median comparisons (implemented by Matlab function “signrank”). Wilcoxon rank sum test was used for unpaired median comparisons (implemented by Matlab function “ranksum”). Pearson coefficient of correlation was used to compute correlations between two conditions (implemented by Matlab function “corr”). Across all fits reported uncertainties (i.e. confidence intervals) for best-fit parameter values were extracted from fit covariance matrices (fitting was performed using Matlab function “nlinfit”). In order to assess the statistical significance of multisensory modulation at each time bin, for each visuo-tactile stimulus condition, and for each responsive neuron, we performed a bootstrap-t

procedure[73] with 2000 outer resamplings and 25 inner resamplings (over trials) in order to obtain p values for the difference from zero of MI values.

Data and Code Availability

The dataset and Matlab code for this study are freely accessible on Zenodo at https://doi.org/10.5281/zenodo.14712479. The Python code for the simulations is freely available on GitHub at https://github.com/comp-neural-circuits/Guyoton-Matteucci-etal-2025.git.

Acknowledgements

We thank Denis Jabaudon, Christian Lüscher, Alan Carleton, Daniel Huber and members of the El-Boustani laboratory for discussions. This work was supported by the Swiss National Science Foundation: PCEFP3_181070 (S.E.-B.).

Author Information

M.G., G.M. and S.E.-B. conceived experiments. M.G. performed surgeries, viral infections, wide-field and two-photon imaging, behavioral experiments, and post-mortem analysis. M.G., G.M. and C.G.F. performed behavioral experiments with optogenetics. G.M. coded acquisition software and performed data analysis. M.P.G. and J.G. conceived the network model and performed simulations. M.G., G.M. and S.E.-B. wrote the manuscript.

Ethics Declarations

Authors declare no competing interests.

Corresponding author

Correspondence and requests for materials should be addressed to Sami El-Boustani (sami.el-boustani@unige.ch).

Supplementary Information

Extended Data Fig. 1-15

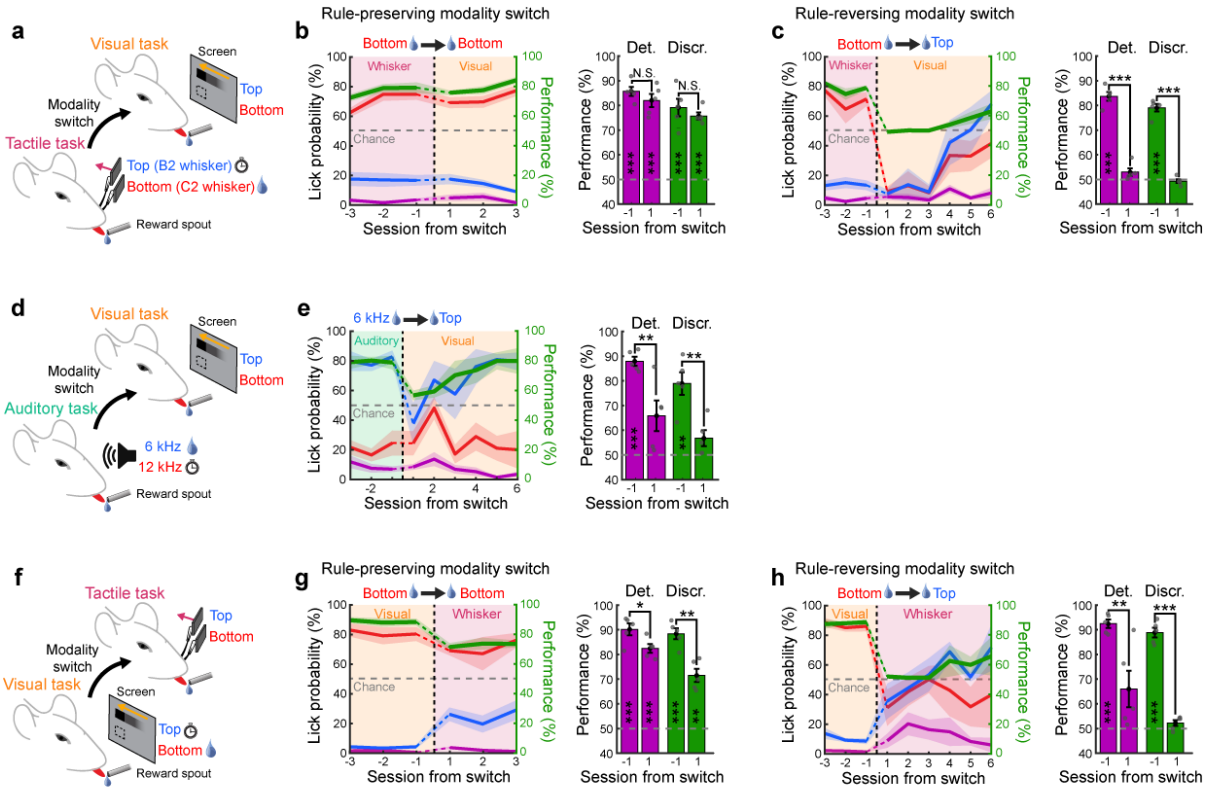

Extended Data Figure 1

Extended Data Fig. 1. Cross-modal generalization in mice across different conditions.

a, Schematic of behavioral paradigm where switches occur between a tactile task and a visual task. Bottom tactile stimuli were rewarded upon licking in the first task. **b,** Left: Average task performance and conditional lick probabilities across sessions for mice (N=5 mice) undergoing a rule-preserving modality switch (dashed vertical line). Shaded areas and color code as in Fig. 1e. Right: detection (purple) and discrimination (green) performance distribution the session before and after the switch (two-sided paired t-test comparing days, *p<0.05, **p<0.01, ***p<0.001, N.S. Not significant). Performances are also tested against chance level (two-sided t-test, *p<0.05, **p<0.01, ***p<0.001, Blank: Not significant). **c,** Same as panel b but for a rule-reversing modality switch. **d,** Schematic of behavioral paradigm where switches occur between an auditory discrimination task with two pure tones (6 kHz and 12 kHz) and a visual task. The 6 kHz tone is always associated with a water reward. **e,** Same as panel b for an auditory to visual modality switch, where the top visual stimulus is associated to a reward. **f,** Schematic of behavioral paradigm where switches occur between a visual task and a tactile task with the bottom visual stimulus being the rewarded one. **g,** Same as panel b for mice undergoing a rule-preserving switch (N=5 mice). **h,** Same as panel g but for rule-reversing modality switches. For cases with spatial rule-reversing modality switch or in absence of spatial prior (i.e. panels c,e,h), behavioral curves are shown for 6 consecutive sessions following the switch.

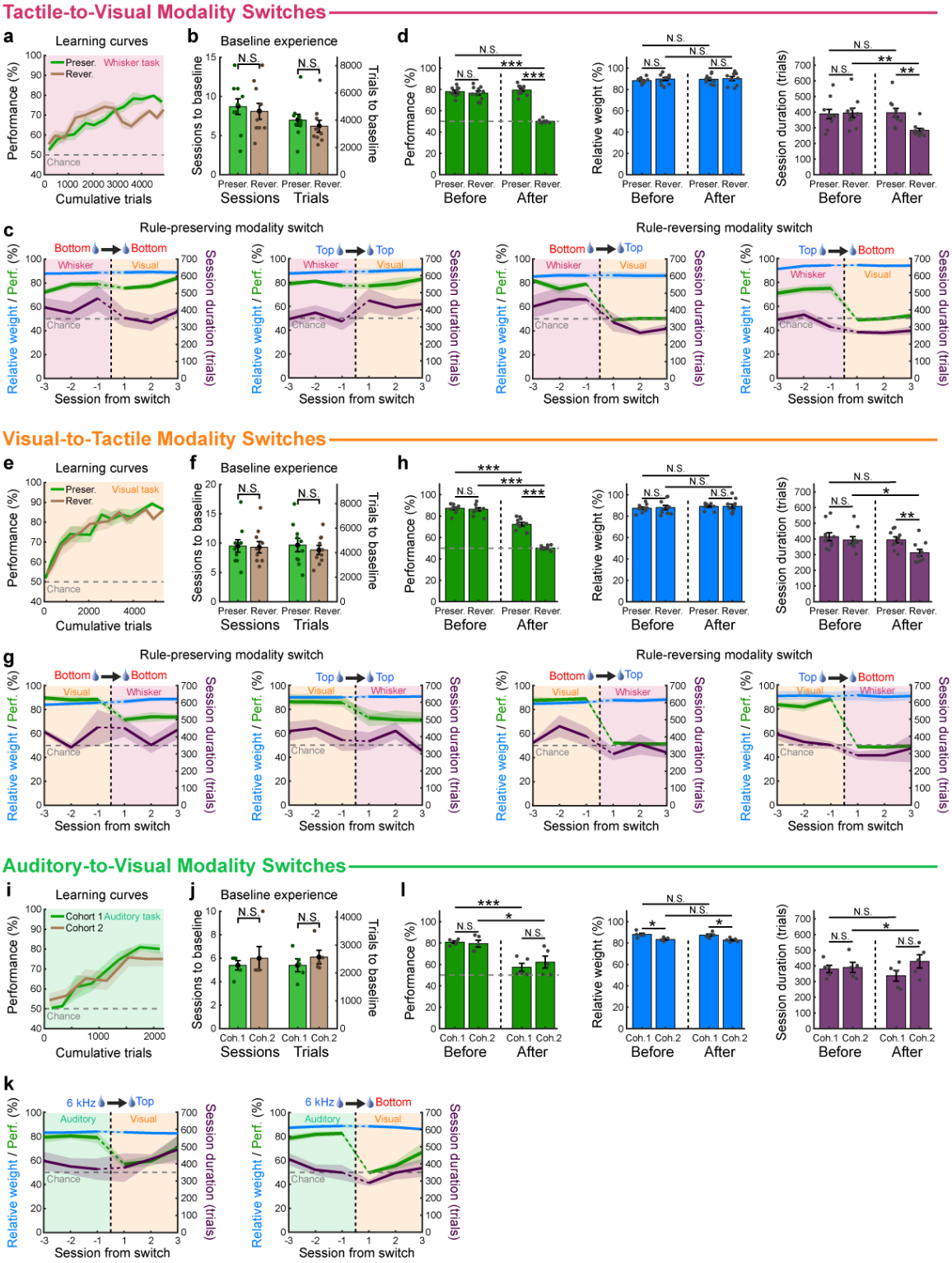

Extended Data Figure 2

Extended Data Fig. 2. Learning trajectory, task experience, task performance and motivational state in the different cohorts of mice and different tasks.

a, Discrimination learning curves for the cohorts of mice performing the whisker task before rule-preserving (green, N=10 mice) or rule-reversing (brown, N=10 mice) modality switch to a visual task. Shaded areas: s.e.m. **b,** Comparison of number of sessions and trials experienced by mice in the rule-preserving and rule-reversing cohorts before the switch (unpaired two-sided t-test, *p<0.05, **p<0.01, ***p<0.001, Blank: Not significant). **c,** Switch-aligned task performance (green), relative weight (blue) and session duration (purple) averaged across mice for all tactile-to-visual conditions. Shaded areas: s.e.m. **d,** Comparison of performance (green), relative weight (blue) and session duration (purple) averaged over the 3 days preceding (before) or following (after) modality switch (unpaired two-sided t-test, *p<0.05, **p<0.01, ***p<0.001, Blank: Not significant). In all plots, horizontal gray dashed line indicates performance chance level and vertical black dashed line indicates the switch. **e-h,** same as panels a-d but for cohorts of mice performing the visual task before rule-preserving (green, N=10 mice) or rule-reversing (brown, N=10 mice) modality switch to the whisker task. **i-l,** Same as panels a-d but for two cohorts of mice (N=5 mice each) performing the auditory task before modality switch to the visual task. All bar plots indicate the average value and s.e.m.

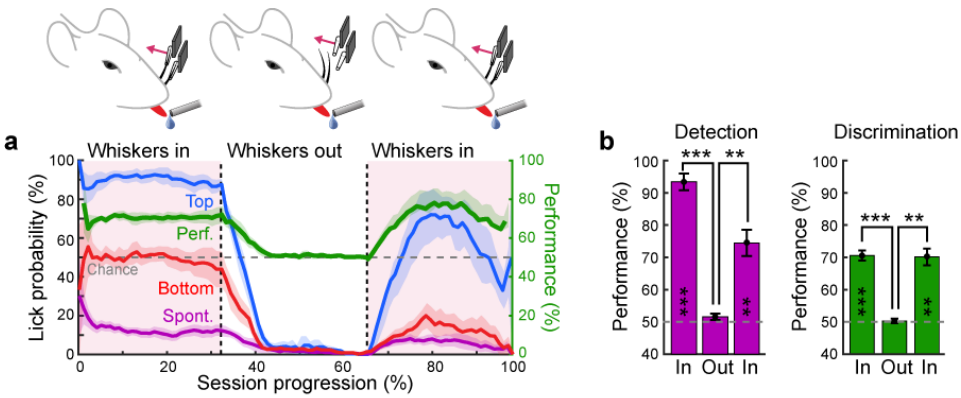

Extended Data Figure 3

Extended Data Fig. 3. Performance of mice at the whisker discrimination task with and without whiskers in the piezo stimulators.

a, Conditional lick probabilities and performance during the whisker discrimination task averaged across expert mice (N=5 mice). Sessions were normalized between beginning (0%) and end (100%) before the average was performed. Color code is the same as in Fig. 1. During these sessions, mice performed the task for approximately one-third of the trials with whiskers present in the capillary tubes used to deliver tactile stimulations. Subsequently, the whiskers were removed while maintaining the tube positions, and the task continued for an equivalent duration. Finally, the whiskers were reinserted to confirm that mice were still motivated to perform the task. **b,** Comparison of detection (purple) and discrimination (green) performance during the 3 different phases of the sessions described in panel a. Comparisons are performed between consecutive phases (paired two-sided t-test, ***p<0.001, **p<0.01, *p<0.05) and with chance level (two-sided t-test with p=0.188 for detection and p=0.710 for discrimination during the Out phase). Mice were not able to perform the task in absence of direct whisker stimulations.

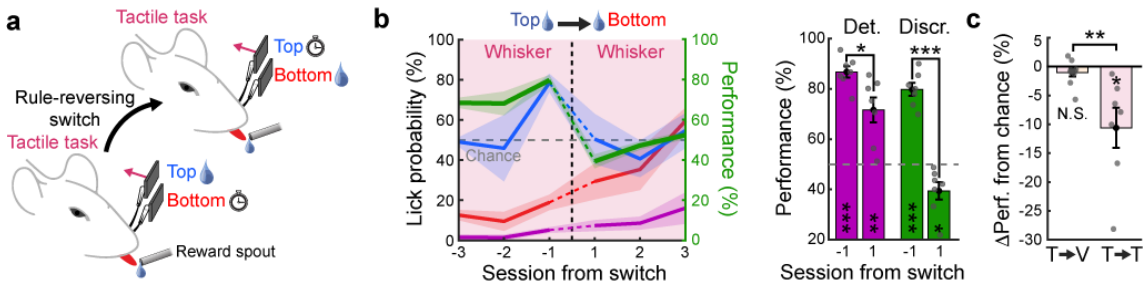

Extended Data Figure 4

Extended Data Fig. 4. Relearning the whisker discrimination task following a reversal of the spatial rule within the same modality.

a, Schematic of the behavioral paradigm for rule-reversing switch within the tactile modality. Once mice became experts in the whisker discrimination task, the spatial rule of the task was reversed. **b,** Left: Average task performance across sessions for mice exposed to the reversed reward association (N=7 mice). Shaded area: S.E.M. Vertical dashed line indicates the transition from one rule to the other. Right: detection (purple) and discrimination (green) performance distribution the session before and after the switch (paired two-sided t-test comparing days, *p<0.05, **p<0.01, ***p<0.001, N.S. Not significant). Performances are also tested against chance level (two-sided t-test, *p<0.05, **p<0.01, ***p<0.001, Blank: Not significant). **c,** Comparison of performance change relative to chance level after rule switch across sensory modalities (i.e. tactile to visual) or within the whisker task (N=10 mice for visuo-tactile and N=7 mice for tactile only, unpaired two-sided t-test, **p=0.0056). Mice maintained their responses to whisker stimulations significantly above chance level, yet their performance on the discrimination task fell significantly below chance (*p=0.0221). This suggests a reduced adaptability to a reversal of the spatial rule within the same modality, potentially due to a stronger habitual response linked to the previously rewarded whisker or an entrenched bias regarding the saliency of whisker stimulations.

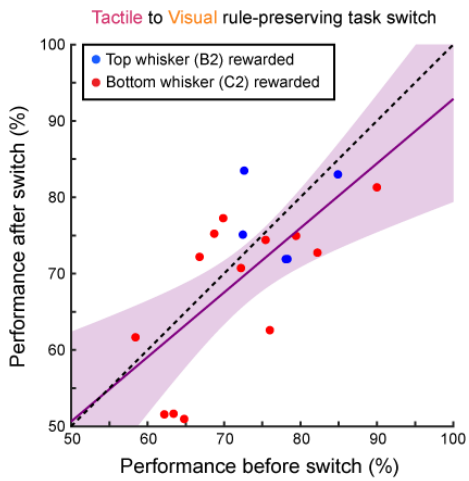

Extended Data Figure 5

Extended Data Fig. 5. Performance level is maintained after switches from the whisker discrimination task to the visual task.

Comparison between performance in the whisker task the session before the switch and the performance in the visual task the session following the switch. This includes mice that experienced the switch, showcasing varying performance levels and rewarding either the top whisker (blue) or the bottom whisker (red). Performances before and after the switch were correlated (N=18 mice, Pearson coefficient: 0.68, p=0.0018) and close to the unity dashed line. Shaded area: 95% confidence interval. Mice exhibit consistent discrimination performance following modality switch, suggesting that cross-modal generalization may correspond to the initial sensorimotor learning level, or that shared influences, such as thirst-related motivation, impact both tasks equally.

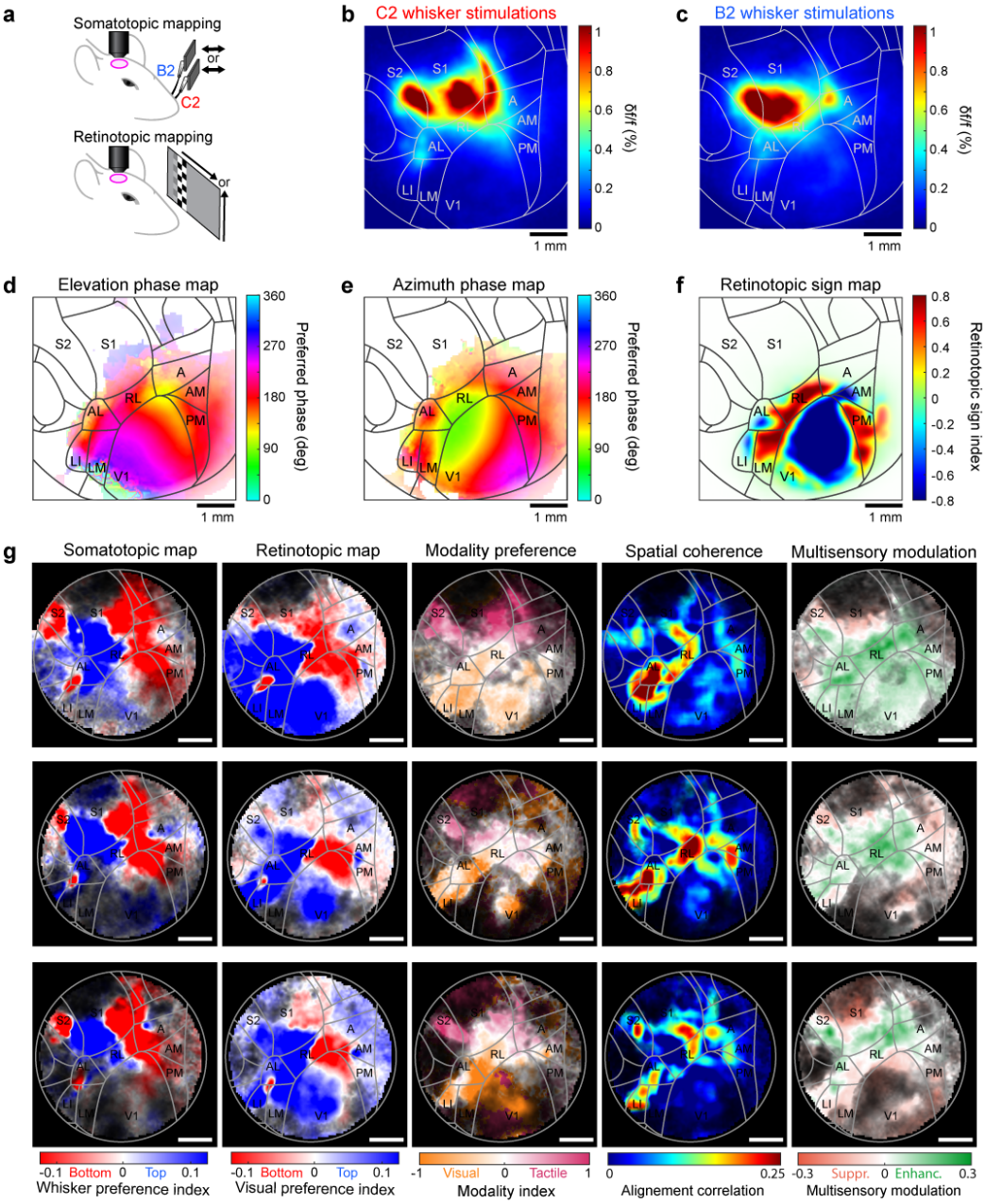

Extended Data Figure 6

Extended Data Fig. 6. Average whisker and retinotopic maps with examples of single mouse visuo-tactile functional maps obtained in wide-field imaging.

a, Schematic of the protocols used to measure single whisker response maps (top) and retinotopic maps (bottom) in transgenic mice expressing GCaMP6f in layer 2/3 during wide-field imaging through a cranial window. **b,** Response map averaged across mice (N=41 mice) for C2 whisker stimulations. Projection of the Allen Mouse Brain Atlas is overlaid on top with areas names for reference. **c,** Same as in panel b for B2 whisker stimulations. **d,** Elevation phase map averaged over mice (N=50 mice). Pixels with low response amplitude are displayed in white. **e,** Azimuth phase map average over the same mice as in panel d. **f,** Retinotopic sign map computed based on the elevation and azimuth phase maps of panels d and e. **g,** Representative examples of visuo-tactile functional maps obtained from sparse noise protocol responses from 3 different mice (rows). From left to right: 1. Whisker preference map used to describe somatotopy in the vertical space with red colors indicating preference for the bottom whisker and blue colors indicating preference for the top whisker. 2. Visual position preference map used to describe retinotopy in vertical space. 3. Modality preference map describing the dominant modality for each pixel. 4. Spatial coherence map between retinotopic and somatotopic maps. 5. Multisensory modulation map indicating areas with responses enhancement or suppression for visuo-tactile stimuli.

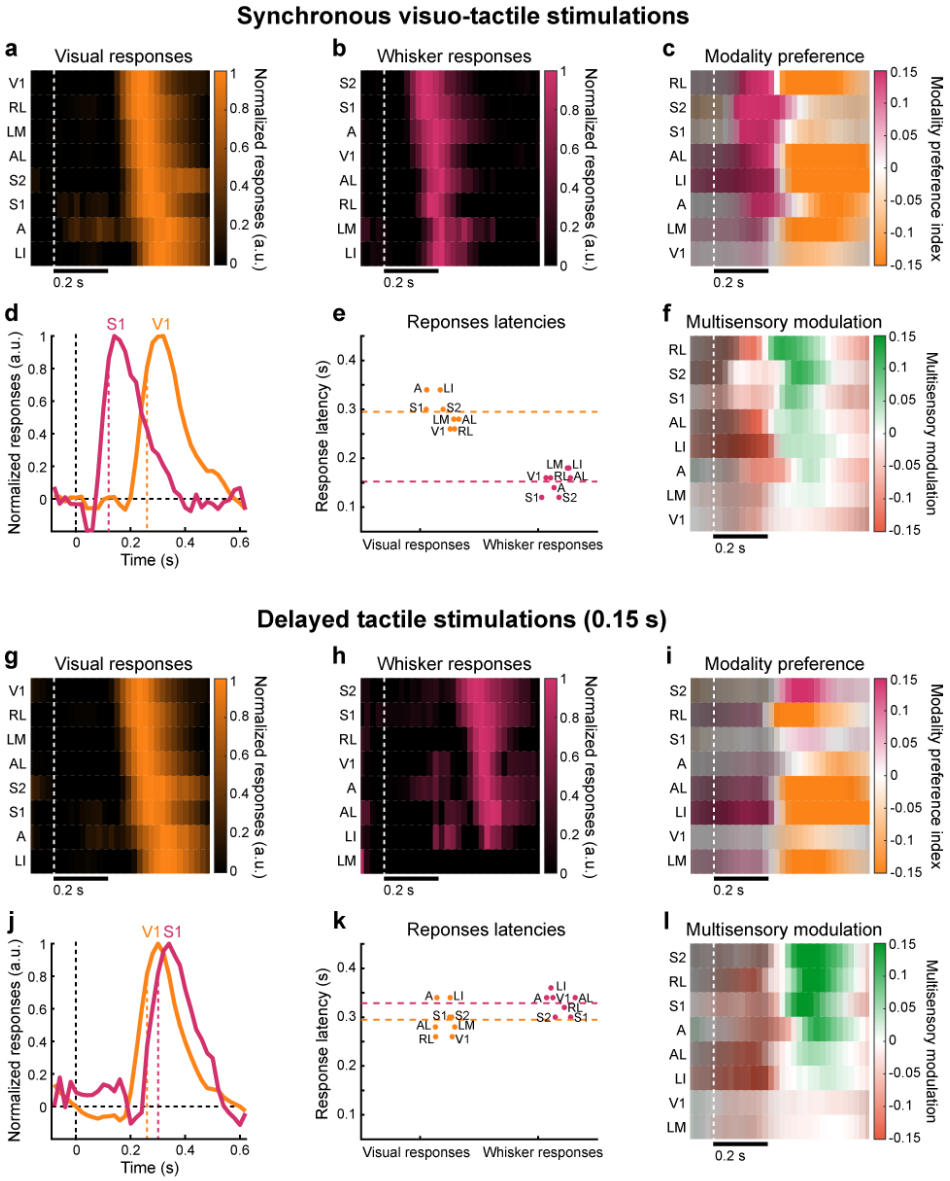

Extended Data Figure 7

1932

Extended Data Fig. 7. Comparison of cortical response dynamics for synchronous or delayed visuo-tactile stimulations.

a, Average activation time course for each visually responsive area following stimulus onset (N=29 mice). Areas are ordered based on response onsets. White dashed line indicates stimulus onset. **b,** Same as panel a for responses in cortical areas evoked by whisker stimuli. **c,** Time course of the modality preference index across cortical areas with visuo-tactile responses. **d,** Average response time course in the primary visual cortex (V1) and the whisker primary somatosensory cortex (S1) highlighting an offset of about 0.15 s between cortical responses evoked by the two modalities. Colored dashed lines indicate response latency computed as the time point where the response curve reaches 80% of its peak amplitude. **e,** Distribution of response latencies for cortical areas with evoked visual (orange) or whisker tactile (magenta) responses. Colored dashed lines indicate the average latencies across areas. **f,** Time course of the multisensory modulation index across cortical areas with visuo-tactile responses. **g-l** Same as panels a-f for tactile stimuli presented with a delay of 0.15 s with respect to the visual stimuli to match response latencies in the cortical areas. Multisensory enhancement was observed when stimuli were synchronized or delayed though they were stronger when cortical responses had comparable latencies.

1951

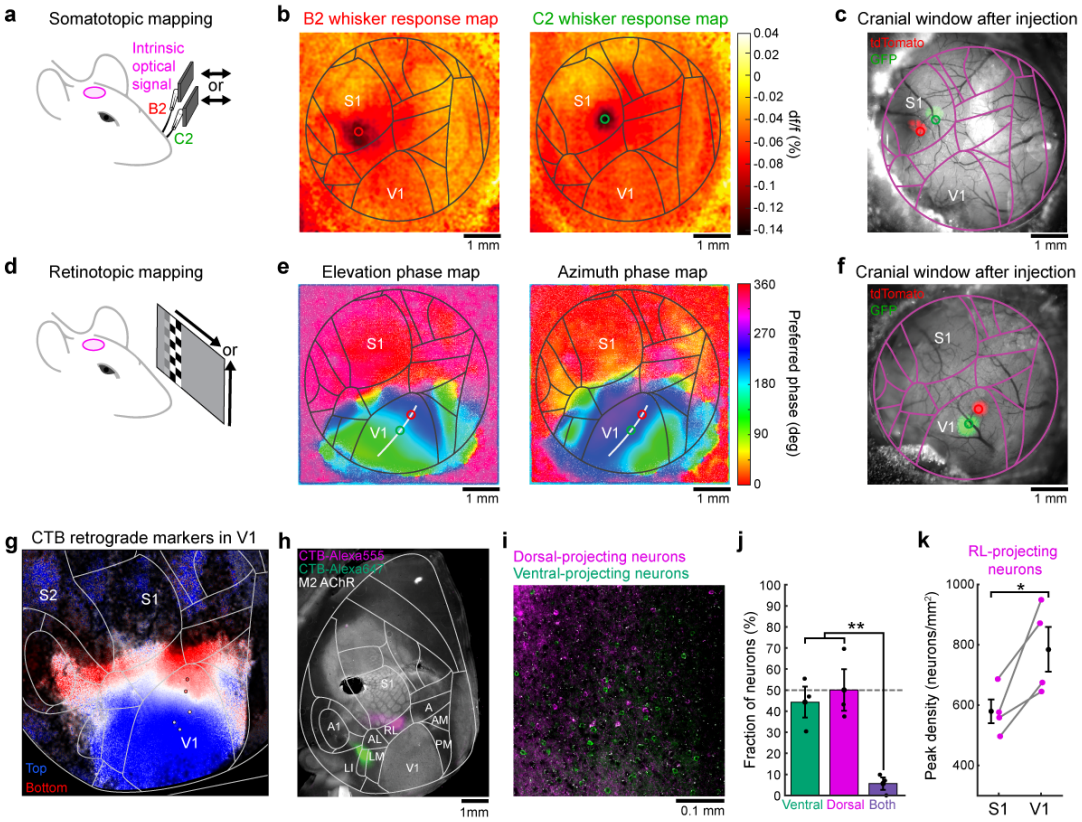

Extended Data Figure 8

Extended Data Fig. 8. Functional mapping of vertical positions in the visual or whisker somatosensory cortex for anatomical tracing.

a, Schematic of the protocol for mapping whisker-responding areas in the dorsal cortex. Single whiskers are stimulated repeatedly during intrinsic optical signal imaging. **b,** Change in red light reflectance on the surface of the cortex measured after averaging several trials of whisker stimulations relative to baseline. The left image reveals the barrel location corresponding to B2 whisker stimulations and the right plot for C2 whisker stimulations. **c,** Image of the cranial window several weeks after injection of viral vectors to express GFP and tdTomato in two distinct parts of the whisker somatotopic map. Locations of B2 and C2 barrels in S1 defined in panel b are indicated with circles overlaid on top of the fluorescent signal where injections were performed. **d,** Schematic of the protocol for retinotopic mapping in areas of the dorsal cortex. Horizontal or vertical bars drift across the screen and they are textured with a flickering checkerboard pattern to elicit strong cortical responses at different phases corresponding to the retinotopic preference. **e,** Retinotopic phase maps for elevation and azimuth on the dorsal cortex. These maps are then used to identify a gradient across vertical dimension in an iso-profile along the azimuth dimension. Two retinotopically distinct locations along the vertical axis are identified and labeled for viral injection. **f,** Image of the cranial window four weeks after injection of viral vectors to express GFP and tdTomato in two distinct parts of the primary visual cortex retinotopic map. Locations where stereotaxic injections were performed corresponding to panel e are indicated with circles overlaid on top of the fluorescent signals. **g,** Cholera Toxin B subunit (CTB) conjugated to different Alexa dyes was injected in different locations of the retinotopic map in V1 (circles). After perfusing the brain and flattening the cortex, a map was reconstructed over the dorsal cortex combining all injection sites to reconstruct areas where neurons project to the region of V1 encoding stimuli on the top (blue) or bottom (red) part of the visual field. All cortices with CTB labels were registered to a common atlas before performing the analysis (5 injection sites from N=3 mice). A similar analysis was performed previously with coronal slices[29]. **h,** Flattened cortex with injections of CTB conjugated with two different dyes (Alexa555 and Alexa647) in the dorsal and ventral visuo-tactile area, respectively. Immunohistochemical localization of M2 AChR is used to identify V1 and the barrels in S1 for atlas registration. **i,** Example image obtained with confocal microscopy where dorsal-projecting neurons (magenta) and ventral-projecting neurons (green) are intermingled in V1. **j,** Fraction of neurons that projected to the ventral area exclusively (green), to the dorsal area exclusively (magenta) or to both (purple) (N=3 mice, unpaired two-sided t-test, **$p=1.8x10^{-3}$, n=230 neurons for ventral, n=277 neurons for dorsal and n=26 neurons for both out of 26 fields-of-view). Neurons that project to the dorsal and ventral visuo-tactile areas display minimal overlap, suggesting they may process distinct types

of visual information. **k,** Comparison of peak density of RL-projecting neurons in V1 and S1 as measured with confocal imaging (N=4 mice, paired two-sided Wilcoxon test, *p=0.042)

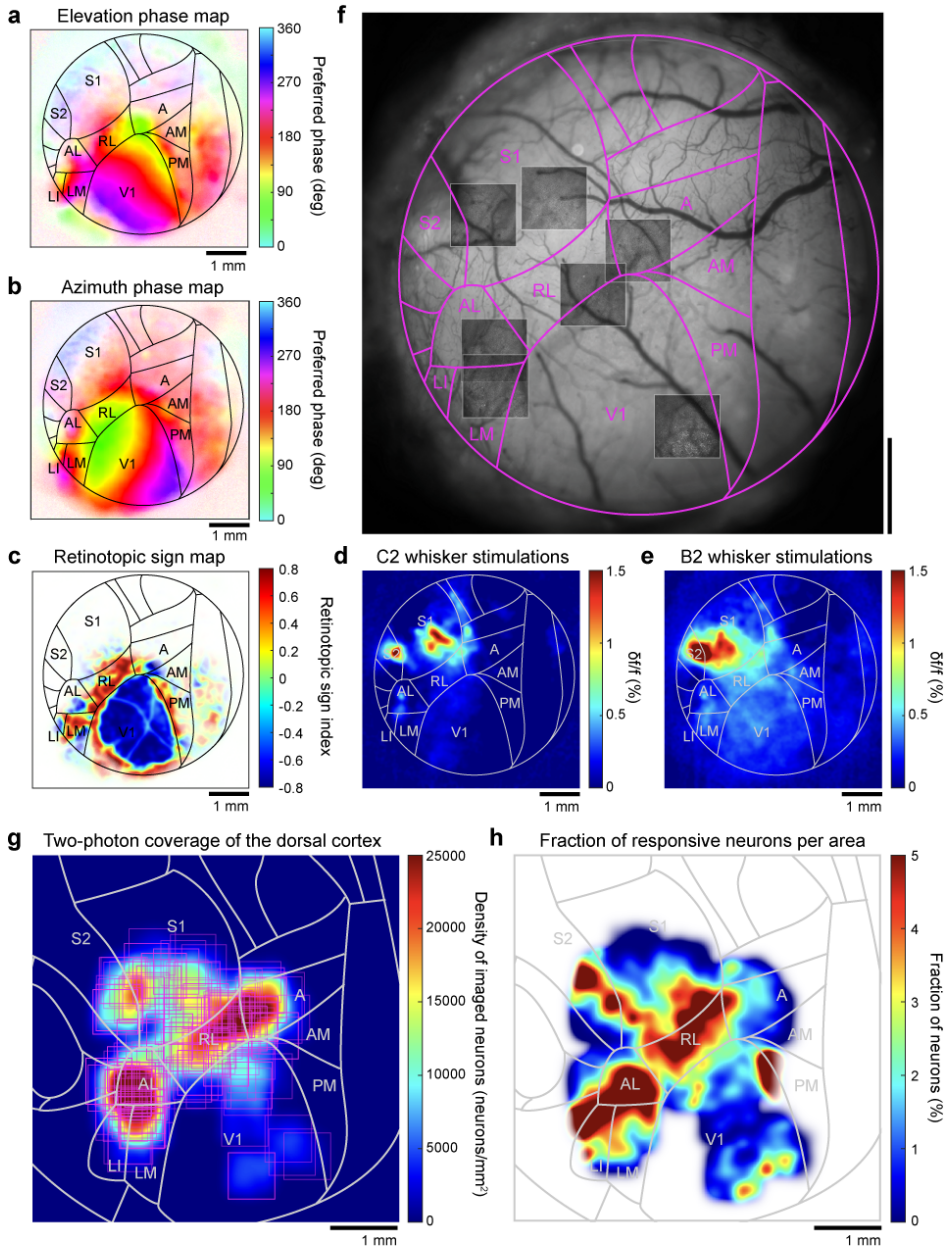

Extended Data Figure 9

1990

Extended Data Fig. 9. Coverage of large portions of the cranial window for characterizing visuo-tactile responses at single-cell level using two-photon microscopy.

a-e, Functional maps are obtained and aligned with the Allen Mouse Brain Atlas for each individual mouse, ensuring precise localization of neurons within their respective areas. Subsequently, all maps are realigned to a common reference atlas to reconstruct wide-field maps. Visual stimulation protocols are used to obtain phase maps for elevation (panel a) and azimuth (panel b) to compute the retinotopic sign map (panel c). Additionally, whisker stimulations provide response maps for C2 (panel d) and B2 (pandel e) whisker stimulations. **f,** Image obtained with wide-field imaging where blood vessels are well distinguished on the surface of the cortex. The atlas fitted with functional maps is overlaid on top in purple. For this mouse, seven fields-of-view were imaged using two-photon microscopy and positioned on the cortical surface by matching blood vessel patterns. **g,** Coverage of visual and tactile areas of the dorsal cortex with two-photon imaging across mice. Using the common atlas and information about all neuron's location, we can recreate a large-scale population using single-cell information. We could collect N=272 fields-of-view across N=25 mice. **h,** Fraction of neurons imaged with two-photon microscopy that were responsive to at least one stimulus condition. The areas of high responsivity are in accordance with wide-field imaging. White color indicates regions where no imaging was performed.

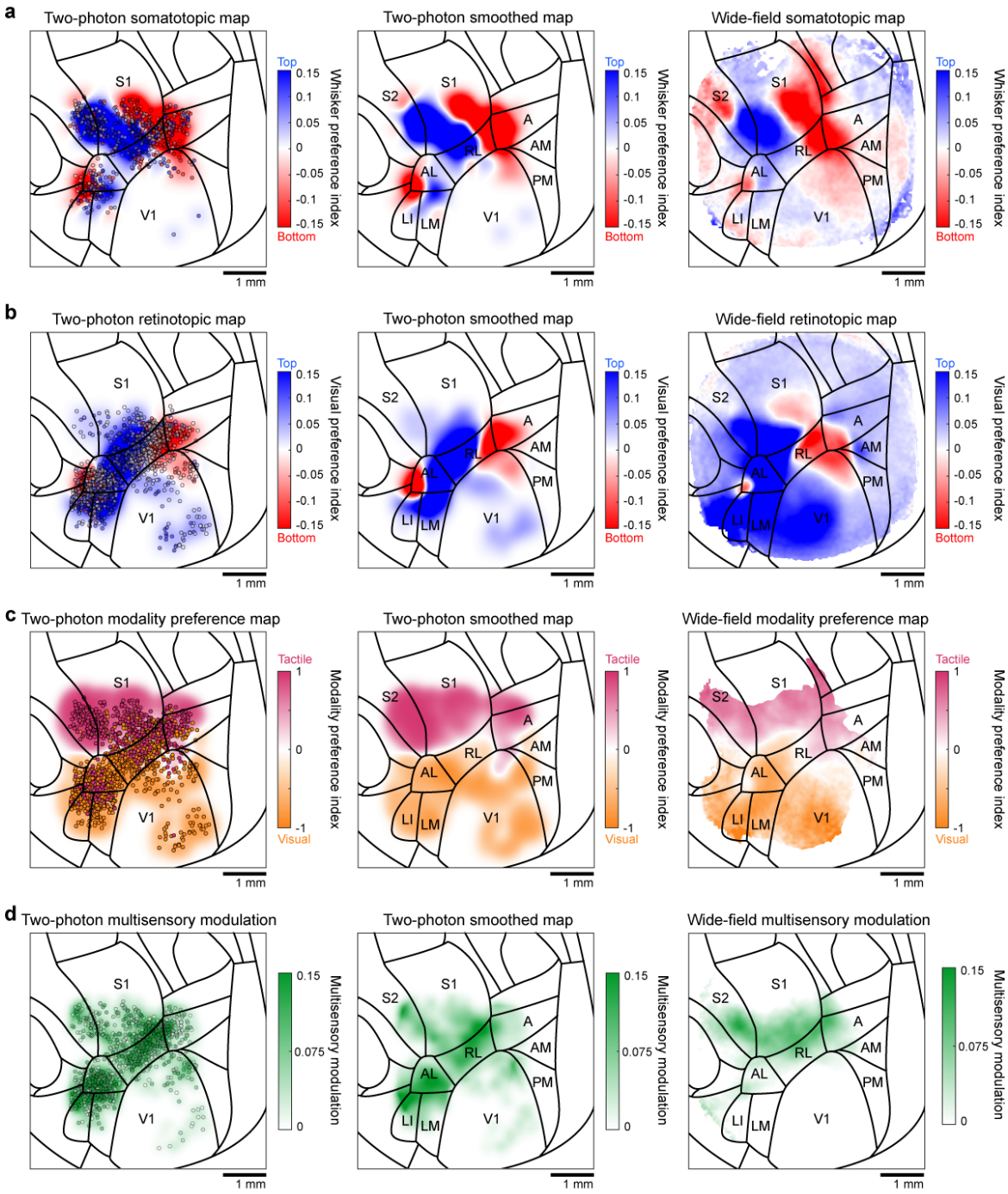

Extended Data Figure 10

2010

Extended Data Fig. 10. Functional maps correspondence between wide-field and two-photon calcium imaging.

a, Left: Distribution of neurons imaged with two-photon microscopy with significant whisker tactile responses. Neurons are displayed on the common atlas and are color-coded based on their whisker preference (n=790 neurons). Middle: Large-scale functional map reconstructed from single neuron whisker preferences. Right: Somatotopic map for the whisker preference obtained with wide-field imaging. Pearson coefficient of correlation between the wide-field map and the two-photon reconstructed map: 0.847. **b,** Same as in panel a for neurons with significant visual responses (n=1,816 neurons, Pearson coefficient of correlation: 0.651). **c,** Same as in panel a displaying modality preference for all neurons with significant whisker tactile or visual responses (n=2,160 neurons, Pearson coefficient of correlation: 0.795). **d,** Same as in panel a displaying multisensory enhancement for all neurons with significant multisensory modulation. For this analysis, the multisensory modulation is computed as the variation between the most suppressed and most enhanced response across conditions for all neurons (n=2,497 neurons, Pearson coefficient of correlation: 0.4458). These neurons were from the same dataset used for Figure 5 (N=25 mice).

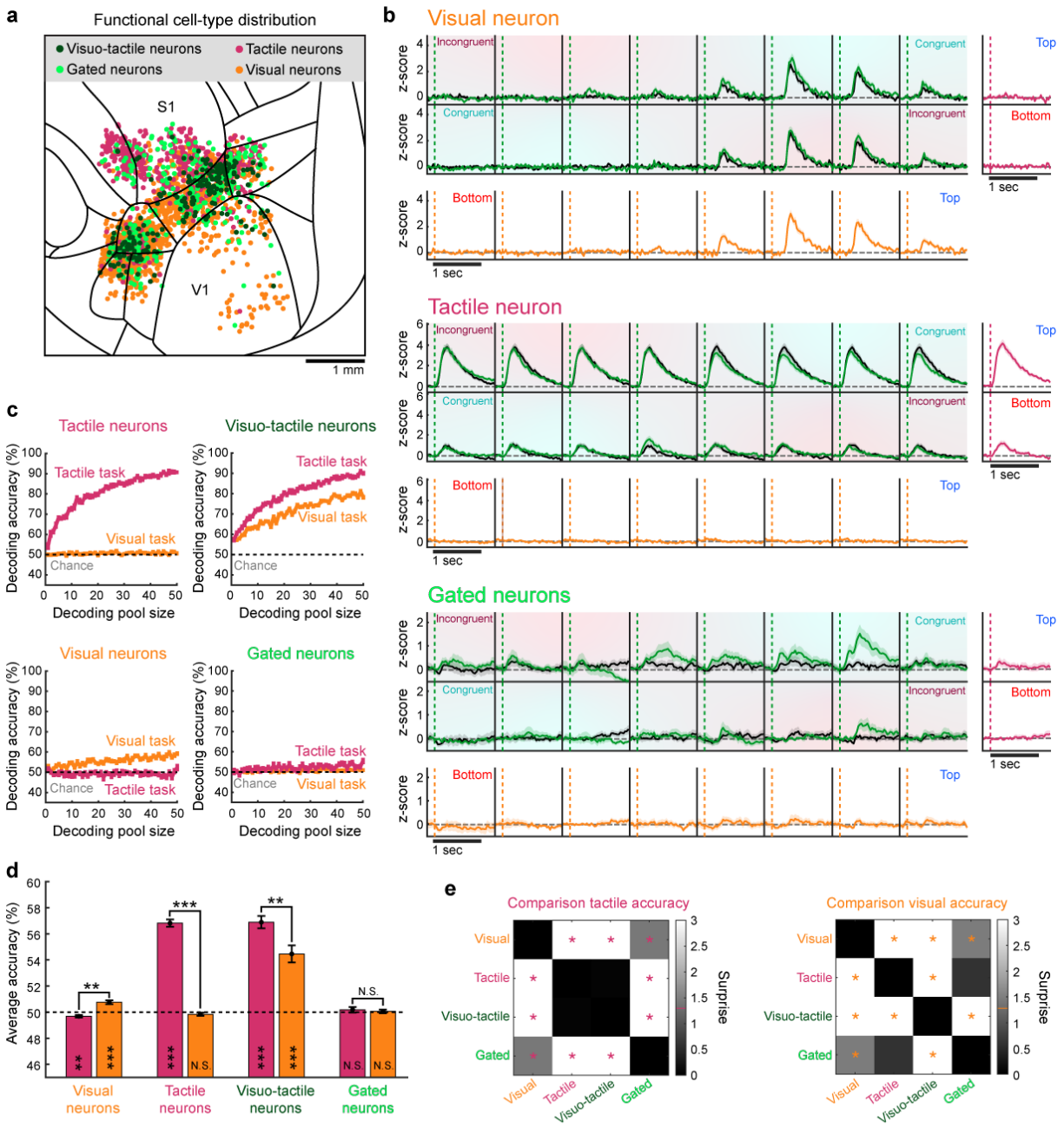

Extended Data Figure 11

2028

Extended Data Fig. 11. Distribution of functional cell-types across the dorsal cortex and their impact on cross-modal generalization.

a, Distribution of significantly responsive neurons across the dorsal surface of the cortex (from the same N=25 mice presented in Figure 5). Common atlas overlaid for reference. Color code indicates functional cell-type of each neuron (n=2,703 neurons). Neurons were classified in four categories: tactile neurons (magenta) responded only to whisker stimulations (n=567); visual neurons (orange) responded only to visual stimulations (n=1,593); visuo-tactile neurons (dark green) responded to both visual and whisker stimulations (n=213); gated neurons (light green) responded only to concomitant visuo-tactile stimulations (n=319). **b,** Example visuo-tactile receptive field for a visual neuron (top), a tactile neuron (middle) and a gated neuron (bottom). Color code is identical to Fig. 5b. Note that the gated neuron responds only when visual and whisker stimulations are presented together in the top location (spatially congruent condition). **c,** Decoding accuracy for the tactile task and the visual task as a function of the pool size. A Bayesian decoder was trained to discriminate the location of whisker stimulation (magenta) based on the neuronal responses of a pool of neurons. The same decoder was then used to decode the location of visual stimuli (orange), mimicking the modality switch experienced by mice in the behavioral experiment. Error bars: S.E.M. Only visuo-tactile neurons were able to achieve good generalization performance across modalities because of their functional properties. Tactile neurons could only afford good decoding performance in the whisker-based task but could not maintain it when switching to the visual task. Performance chance level is indicated with a gray dashed line at 50%. **d,** Comparison of single-neuron decoding accuracy distributions on tactile responses (magenta) and generalization to the visual ones (orange) for each functional cell-type class (paired two-sided t-test comparing tactile and visual task, *$p<0.05$, **$p<0.01$, ***$p<0.001$, N.S. Not significant). Decoding accuracies are also tested against chance level (two-sided t-test, *$p<0.05$, **$p<0.01$, ***$p<0.001$, N.S.: Not significant). Error bars: S.E.M. **e,** Surprise matrix corresponding to all two-sided t-tests performed across tactile (left) or visual (right) conditions for data in panel d. Asterisks indicates surprise values larger than 1.301 corresponding to $p<0.05$.

2060

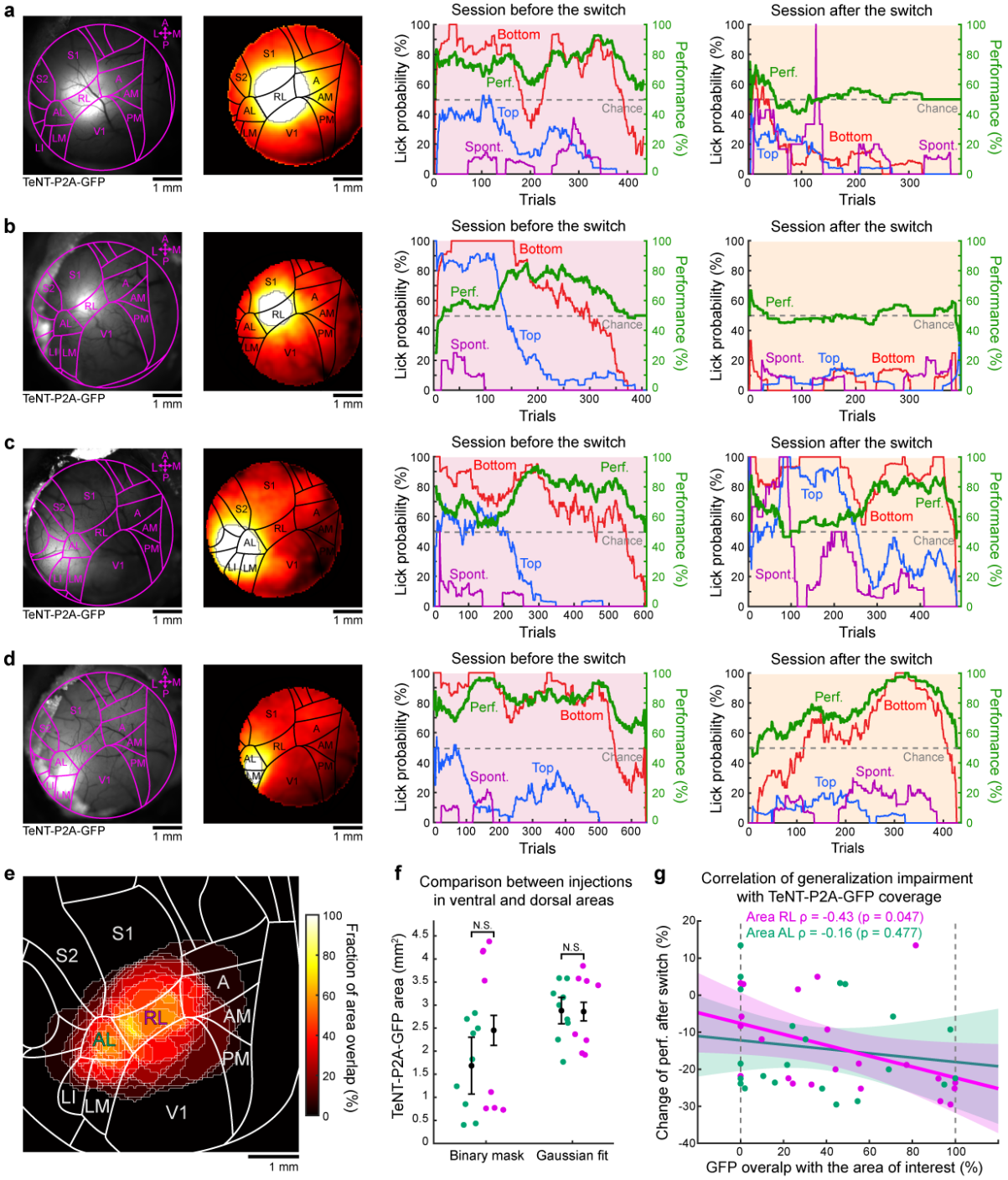

Extended Data Figure 12

Extended Data Fig. 12. Cross-modal generalization impairment following rule-preserving switches in relation to TeNT expression in different associative areas of the dorsal cortex.

a, Left: Example of TeNT-P2A-GFP expression pattern over the cranial window and corresponding estimate of expression coverage after blood vessels subtraction. Right: Effect of cortical silencing on cross-modal generalization from the tactile task to the visual task while preserving the spatial rule of the task. The discrimination performance dropped at chance level after the switch. **b-d,** Same as in panel a but for other example mice with cortical injections at various locations and the resulting impact on cross-modal generalization performance. Note that equal volumes of viral vectors were injected in each mouse; however, some expression patterns appear truncated at the edge of the window. **e,** Overall coverage across all experiments performed with this protocol. **f,** Comparison of estimated surface expressing TeNT-P2A-GFP between injections performed in ventral (green, N=9 mice) or dorsal (magenta, N=8 mice) areas. On the left, the surface was estimated using a binary mask obtained with the normalized fluorescent signal (unpaired two-sided t-test, p=0.15). On the right, the surface of expression was estimated using a Gaussian fit to include regions obstructed by the dental cement at the edge of the cranial window (see Methods, unpaired two-sided t-test, p=0.66).**g,** Example of correlation between the level of TeNT-P2A-GFP overlaps with a specific area (here RL or AL) and the corresponding drop of discrimination performance after switch. To obtain a more robust effect for the correlation, we computed the performance changes over 3 consecutive sessions after switch (N=22 mice, Pearson coefficient: -0.43, p=0.047 for RL; Pearson coefficient: -0.16, p=0.48 for AL).

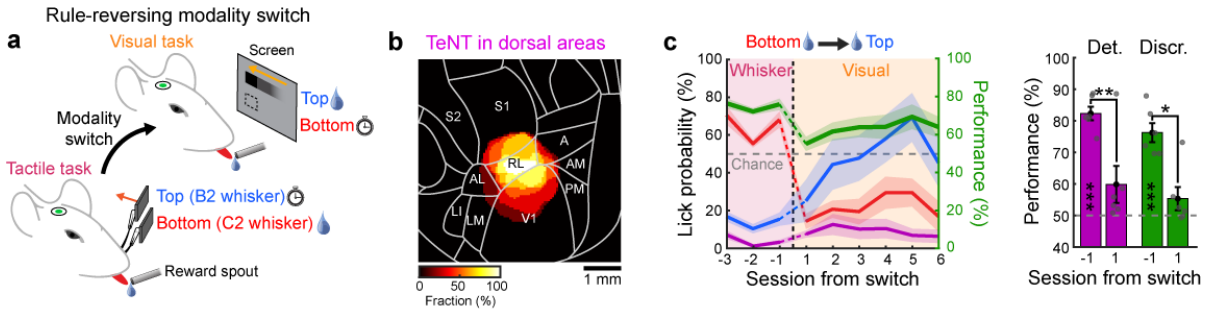

Extended Data Figure 13

Extended Data Fig. 13. Relearning after rule-reversing modality switch in mice expressing TeNT-P2A-GFP in the dorsal area RL.

a, Schematic of behavioral paradigm where the modality switches occur between a tactile task and a visual task in mice expressing TeNT-P2A-GFP in RL. The bottom whisker stimulus is associated with the reward initially while the top visual stimulus becomes associated to rewards after the modality switch. **b,** Average TeNT-P2A-GFP coverage in all mice where dorsal neurons were silenced (N=6 mice). **c,** Left: Average task performance and conditional lick probabilities across sessions for mice population in panel b (N=6 mice) switching from the tactile task to the visual task with a spatial rule reversal. Shaded area: S.E.M. Black dashed line indicates the switch between modalities. Right: detection (purple) and discrimination (green) performance distribution the session before and after the switch (paired two-sided t-test comparing days, *p<0.05, **p<0.01, ***p<0.001, N.S. Not significant). Performances are also tested against chance level (two-sided t-test, *p<0.05, **p<0.01, ***p<0.001, Blank: Not significant). Contrary to mice with intact cortical activity, mice with silenced RL area relearned the visual task faster after the rule-reversing modality switch, indicating a lack of prior on the spatial rule in these mice despite their previous experience with the tactile task.

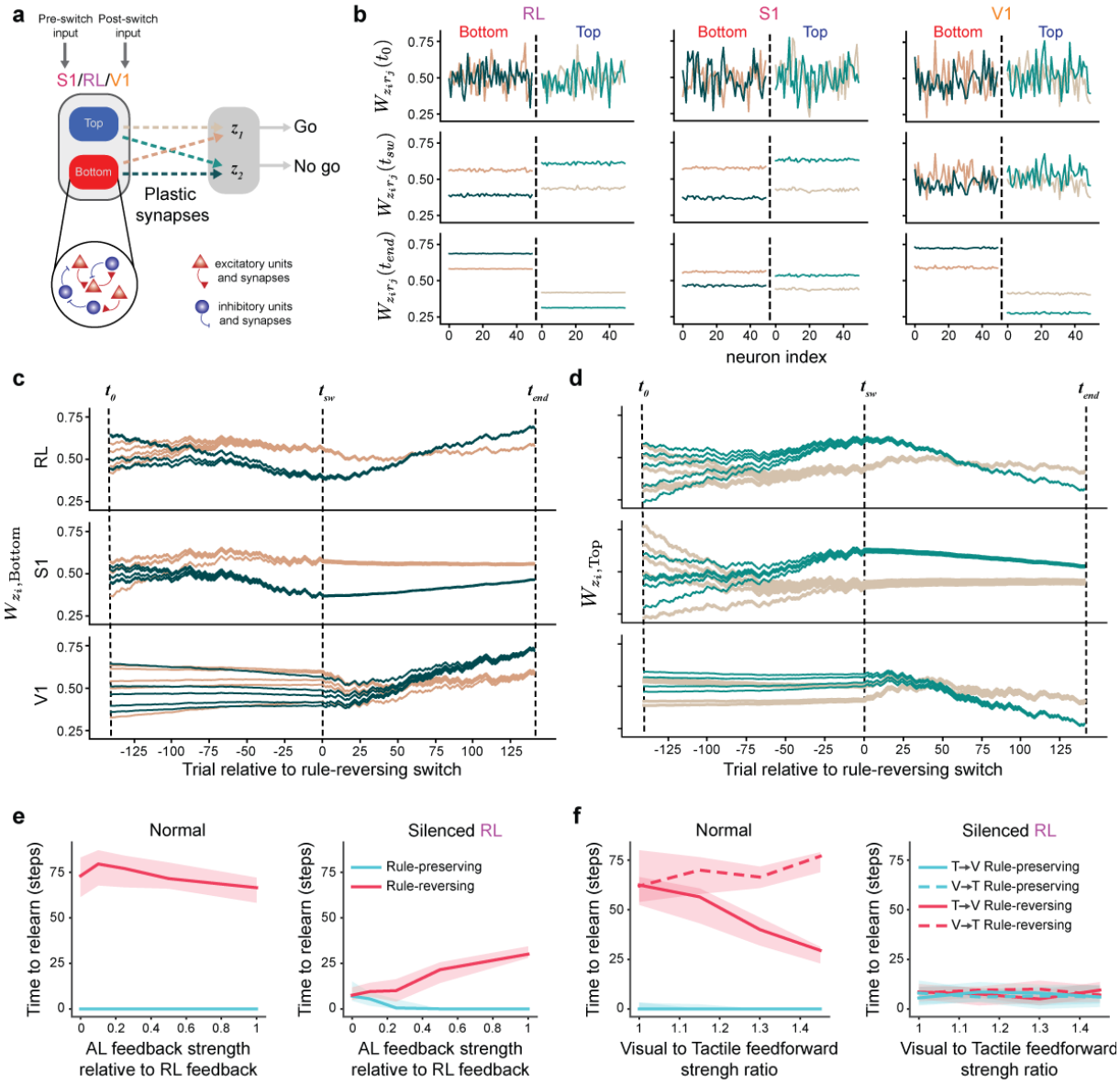

Extended Data Figure 14

Extended Data Fig. 14. Model performance on a rule-reversing modality switch.

a, Model schematic. The model consists of three networks for areas S1, V1, and RL (here only one network is shown for simplicity) that comprised excitatory and inhibitory units tuned to either bottom or top stimuli. Dashed lines denote plastic synapses, and their colors are consistent throughout the figure. The excitatory units in all networks project to the two decision variables z_1 and z_2. Area AL is included in the model but lacks direct projections to the decision area. S1 was initially stimulated, and Bottom stimuli mapped to "Go" action. After the switch, V1 was stimulated, and Top stimuli were mapped to "Go" action. **b,** Weights shown for different time points (corresponding to the dashed lines in panels c and d as a function of the neuronal index. $W_{z_i,r_j}(t)$ denotes the weights from sensory neuron j to decision variable i at time t. t_0: initial timepoint; t_{sw}: time of the switch; t_{end}: final timepoint after a rule-reversing switch. At the time of the switch (t_{sw}), all regions have the same organization of weights such that the correct output is produced (including in V1, due to the reverberation of network dynamics). After the switch, areas RL and V1 have reorganized to drive the correct output. **c,** Subsample of weights from the Bottom-preferring units to z_1 (brown) and z_2 (teal) as a function of time in a simulation. **d,** Same as in panel c for Top-preferring units. **e,** Steps required to relearn the task following a rule-preserving (blue) or rule-reversing (red) modality switch, shown as a function of AL feedback strength in the normal network (left) and in the model with RL silenced (right). **f,** Same as panel e, shown as a function of the visual-to-tactile feedforward connection strength ratio. The comparison includes modality switches from the tactile task to the visual task (solid lines) and from the visual task to the tactile task (dashed lines). Notably, the ratio reported in Extended Data Fig. 8k was estimated to be approximately 1.3. For simplicity, these simulations were conducted without including area AL.

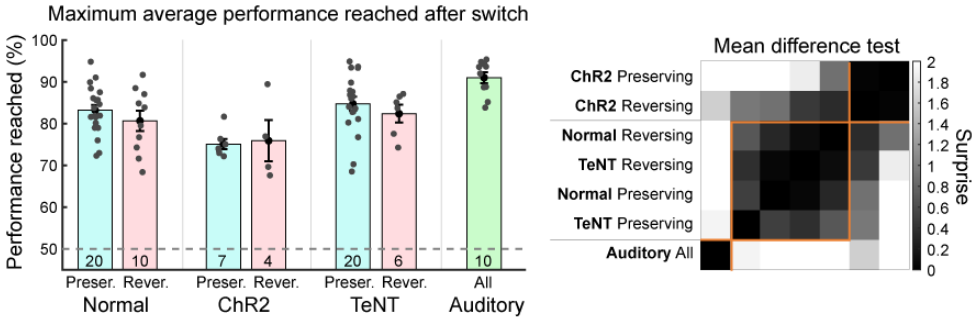

Extended Data Figure 15

Extended Data Fig. 15. Maximum average performance reached following modality switch across different conditions.

Left: Maximum average performance reached in the discrimination task following the modality switch. Mice numbers are indicated for each group at the bottom of the bar. Mice that did not reach the expert criteria in Figure 7F are discarded from this plot. Error bars: S.E.M. Right: Surprise matrix computed from pairwise unpaired two-sided t-test between conditions. A hierarchical clustering based on cosine similarity was used to group conditions based on surprise values. Mice were clustered with respect to the maximum performance reached based on the nature of sensory stimulation used after switch (visual, auditory or optogenetic).